Structure of endogenous Pfs230:Pfs48/45 in complex with potent malaria transmission-blocking antibodies

Ezra T. Bekkering[1,9], Randy Yoo[2,3,9], Sophia Hailemariam[2,3,10], Fabian Heide[2], Danton Ivanochko[2], Matthew Jackman[2], Nicholas I. Proellochs[1], Rianne Stoter[1], Geert-Jan van Gemert[1], Ayana Maeda[4], Takaaki Yuguchi[4], Oscar T. Wanders[1], Renate C. van Daalen[1], Maartje R. Inklaar[1], Carolina M. Andrade[1], Pascal W.T.C. Jansen[5], Michiel Vermeulen[5,6], Teun Bousema[1], Eizo Takashima[4], John L. Rubinstein[2,3,7], Taco W.A. Kooij[1], Matthijs M. Jore[1,10]*, Jean-Philippe Julien[2,3,8,10]**

[1]Department of Medical Microbiology, Radboud University Medical Center, The Netherlands.
[2]Program in Molecular Medicine, The Hospital for Sick Children Research Institute, Toronto, ON, Canada.
[3]Department of Biochemistry, University of Toronto, Toronto, ON, Canada.
[4]Division of Malaria Research, Proteo-Science Center, Ehime University, Matsuyama, Japan
[5]Department of Molecular Biology, Faculty of Science, Oncode Institute, Radboud University Nijmegen, Nijmegen, The Netherlands.
[6]Division of Molecular Genetics, The Netherlands Cancer Institute, Amsterdam, The Netherlands.
[7]Department of Medical Biophysics, University of Toronto, Toronto, Ontario, Canada.
[8]Department of Immunology, University of Toronto, Toronto, Ontario, Canada.
[9]These authors contributed equally.
[10]Senior authors.
*Correspondence: matthijs.jore@radboudumc.nl
**Correspondence; jean-philippe.julien@sickkids.ca

SUMMARY

The Pfs230:Pfs48/45 complex forms the basis for leading malaria transmission-blocking vaccine candidates, yet little is known about its molecular assembly. Here, we used cryogenic electron microscopy to elucidate the structure of the endogenous Pfs230:Pfs48/45 complex bound to six potent transmission-blocking antibodies. Pfs230 consists of multiple domain clusters rigidified by interactions mediated through insertion domains. Membrane-anchored Pfs48/45 forms a disc-like structure and interacts with a short C-terminal peptide on Pfs230 that is critical for Pfs230 membrane-retention *in vivo*. Interestingly, membrane retention through this interaction is not essential for transmission to mosquitoes, suggesting that complex disruption is not a mode of action for transmission-blocking antibodies. Analyses of Pfs48/45- and Pfs230-targeted antibodies identify conserved epitopes on the Pfs230:Pfs48/45 complex and provides a structural paradigm for complement-dependent activity of Pfs230-targeting antibodies. Altogether, the antibody-bound Pfs230:Pfs48/45 structure presented improves our molecular understanding of this biological complex, informing the development of next-generation *Plasmodium falciparum* transmission-blocking interventions.

KEYWORDS

Malaria, *Plasmodium falciparum*, Pfs230, Pfs48/45, cryo-electron microscopy, monoclonal antibodies, transmission-reducing activity, transmission-blocking vaccines

INTRODUCTION

Nearly half of the human population is at risk for malaria infection, making malaria one of the largest public health concerns (1). The parasite that is responsible for the majority of fatal human cases, *Plasmodium falciparum*, is efficiently transmitted by *Anopheles* mosquitoes throughout the population (2). Human-to-mosquito transmission is mediated by mature male and female gametocytes that are taken up by an *Anopheles* mosquito during a bloodmeal (3). Inside the mosquito midgut, male and female gametocytes rapidly activate and egress from their red blood cells (RBCs) as micro- and macrogametes, respectively. Microgametes fuse with macrogametes creating a zygote that forms the basis for further parasite development in the mosquito, eventually resulting in an infectious mosquito that can further spread the parasite and its related disease (4).

Two sexual-stage surface proteins essential for *Plasmodium* transmission, Pfs230 (5) and Pfs48/45 (6), are expressed in both gametocytes and gametes. Pfs48/45 and Pfs230 knockout (KO) parasites showed markedly lower oocyst formation rates, demonstrating that these proteins play a critical role in establishing mosquito infection (7, 8). Pfs48/45 is predicted to have a GPI-anchor and localizes together with Pfs230 to the parasite plasma membrane (PPM) (9). Pfs230, without a recognizable GPI anchor or transmembrane motif, is thought to associate with the PPM by forming a stable heterodimeric complex with Pfs48/45, as shown in co-immunoprecipitation studies (10, 11). This is further supported by the observation that Pfs48/45 KO parasites lose Pfs230 surface retention (7). Both proteins are part of the 6-Cysteine (6-Cys) protein family, characterized by the presence of 6-Cys domains: Immunoglobulin-like folds that contain up to six cysteines that can form disulfide bonds (12, 13). Pfs230 contains fourteen 6-Cys domains, whereas Pfs48/45 contains three (**Figure 1A**). Structural information on the full Pfs230:Pfs48/45 structure has been limited; two full-length structures of recombinant Pfs48/45 have been reported, adopting two distinct conformations – a disc-like (14) and an extended (15) conformation – whereas the structural characterization of Pfs230 has been limited to just the first two domains of the protein (16-20). Additionally, there is a lack of structural understanding of what domains are involved in the Pfs230:Pfs48/45 interaction itself.

The human-to-mosquito transmission stages form a developmental bottleneck for the malaria parasite and are therefore an attractive target for interventions seeking malaria elimination (21), such as transmission-blocking vaccines (TBVs). Indeed, modeling studies have suggested that TBVs could synergistically increase the effectiveness of vaccines targeting other parasite stages (22-24). Importantly, both Pfs230 and Pfs48/45 were recognized in the early 1980s as the targets for antibodies that had potent human-to-mosquito transmission-reducing activity (TRA) (9, 11, 25). Since then, multiple studies have shown that naturally infected individuals can acquire Pfs230 and Pfs48/45-targeted antibodies that are associated with high-level TRA in serum (*e.g.* (26-31)) and these antibodies can block transmission when purified (26). The structure, epitopes, and TRA of these naturally acquired antibodies have been partially characterized at the monoclonal antibody level (15, 17, 20, 32). Domain 1 of Pfs230 (Pfs230D1) and domain 3 of Pfs48/45 (Pfs48/45D3) are the targets of the most potent transmission-blocking monoclonal antibodies (mAbs) (*e.g.* (15, 17, 19, 20, 32-35)). Initial reports suggested that other domains of Pfs230 and Pfs48/45 were not able to elicit comparably potent transmission-blocking antibodies (35). Recently at least three other Pfs230 domains, and Pfs48/45D1, have been identified as targets for potent transmission-blocking antibodies, but structural insight into these epitopes is lacking in comparison to Pfs230D1 and Pfs48/45D3 (32, 36-39).

Regardless of the domain they target, the vast majority of the potent α-Pfs230 antibodies is complement-dependent (17, 20, 36, 40), although some antibodies retain TRA at very high concentrations in the absence of complement (16, 34). In contrast, α-Pfs48/45 antibodies can block transmission at low concentrations in a complement-independent manner (15, 18, 32, 33, 38, 41). The rationale behind what drives antibody potency for both α-Pfs230 and α-Pfs48/45 antibodies remains unclear. As both proteins are capable of eliciting highly potent antibodies, they have been targeted as lead antigens and are currently the most advanced and promising TBVs in development (42, 43). Indeed, immunogens based off these two proteins have been extensively evaluated in preclinical and phase I/II clinical trials (44-47). Although these clinical trials show promising results, induced TRA was incomplete and more efficacious vaccines may thus be needed. Structure-function relationships of how potent antibodies target the Pfs230:Pfs48/45 complex would not only enhance our understanding of *P. falciparum* transmission biology and antibody mechanism of actions, but also aid in the design and development of next-generation malaria vaccines that can induce more potent TRA to reach elimination goals.

Here, we report the molecular structure of the endogenous Pfs230:Pfs48/45 heterodimer in complex with six antibodies with potent TRA as determined by cryogenic electron microscopy (cryo-EM). Cumulatively, our data provide critical molecular insights into the Pfs230:Pfs48/45 heterodimer complex, moving towards deepening our understanding of *P. falciparum* transmission biology and opportunities to block this process through next-generation biomedical interventions.

RESULTS

Structure of the Pfs230:Pfs48/45 complex

We set out to determine the cryo-EM structure of the Pfs230:Pfs48/45 complex by purifying it from mature *P. falciparum* gametocytes. Using the inducible gametocyte producing parasite line NF54/iGP2 (48), we fused *pfs230* (Pf3D7_0209000) C-terminally with a 3xFLAG-C-tag coding sequence, yielding parasite line iGP2$^{230\text{-tag}}$ (**Figure S1A-D**). iGP2$^{230\text{-tag}}$ gametocytes showed normal Pfs230 and Pfs48/45 localization and retained normal *in vitro* exflagellation and mosquito infectivity in standard membrane feeding assays (SMFA; **Figure S1E-F**). The Pfs230:Pfs48/45 complex was purified using anti-FLAG resin. Pfs230 and Pfs48/45 were the highest enriched proteins from this purification as detected by LC-MS/MS (**Figure 1B-D**). Two high-molecular weight bands were observed in Blue-Native Polyacrylamide Gel Electrophoresis (BN-PAGE) **(Figure 1E)**. Both bands were stained by α-Pfs230 antibodies in immunoblotting assays, but only one band was stained by α-Pfs48/45 antibodies, attributing these two bands to the Pfs230:Pfs48/45 complex and Pfs230 alone, respectively (**Figure 1F**). BN-PAGE analysis of eluted protein incubated with a molar excess of different fragment of antigen-binding (Fab) fragments of transmission-blocking antibodies, targeting a range of conformational epitopes on Pfs48/45 and Pfs230, confirmed the native structure of the eluted proteins (**Figure S1G**). While α-Pfs230 Fabs shifted both protein species upwards, α-Pfs48/45 Fabs only affected the upper band, further ascertaining the top band as the Pfs230:Pfs48/45 complex.

Since we were interested in how potent transmission-blocking antibodies are targeting the native Pfs230:Pfs48/45 complex, we generated a size exclusion chromatography (SEC)-purified Pfs230:Pfs48/45 heterodimer in complex with six Fab fragments, using the structurally delineated RUPA-97 (20), LMIV230-01 (19), and RUPA-44 (32), and the yet-to-be-structurally delineated 2A2 (38, 40, 49), 18F25 (36, 49), and RUPA-71 (32) inhibitory antibodies (**Figure 1G, Figure S1H**). Cryo-EM data of this Pfs230:Pfs48/45:6Fab complex was collected at 0°, 35°, and 40° tilt. 2D class averages from this dataset clearly revealed the

presence of all components of the complex: Pfs230 bound to four Fabs (LMIV230-01, RUPA-97, 2A2, 18F25) in complex with Pfs48/45 bound to two Fabs (RUPA-44 and RUPA-71) (**Figure 1H**).

The highest resolution structural information was derived by generating four locally refined maps corresponding to more rigid components of the complex: Pfs230D1-6 bound to RUPA-97, LMIV230-01, and 2A2 at a global resolution of 3.6 Å; Pfs230D7-8 bound to 18F25 at a global resolution of 3.8 Å; Pfs230D9-14 bound to Pfs48/45 at a global resolution of 4.7 Å; and Pfs230D13-14 bound to Pfs48/45, RUPA-44, and RUPA-71 at a global resolution of 3.4 Å (**Figure 1I-J, Figure S2-3, Table 1**).

Insertion domains organize Pfs230 domains

Molecular models were built into each of the locally refined maps to elucidate structural features of the interdomain topologies and dispositions of potent mAbs. The models derived from the maps of Pfs230D1-6:RUPA-97:LMIV230-01:2A2 and Pfs230D7-8:18F25 (**Figure 1I-J, Table 1**) were initialized from experimentally determined crystal structures and predicted AlphaFold (AF) models, which were refined into maps with sufficiently high resolution to model sidechain positions (**Table 1, Table S3**). For the 4.7 Å resolution map of Pfs230D9-14:Pfs48/45, we report the backbone positions of a compositely refined Pfs230D9-12 structure in the presence of the Pfs230D13-14:Pfs48/45 structure discerned from the 3.4 Å resolution map (**Figure 1I-J, Table 1**). AF models of Pfs230D9-D12 were docked and manually rearranged into the Pfs230D9-14:Pfs48/45 map. A template-guided inference strategy in AF2 followed by refinement using map-constrained energy minimizations resulted in the final model. We attribute the lower local resolution of Pfs230D9-12 in our Pfs48/45:Pfs230D9-14 map to intrinsic flexibility between the D12 and D13 domains and to bound antibodies on Pfs48/45 that may create steric hindrance in this region (**Figure S3**).

Each tandem structural unit of Pfs230 consists of A- and B-type 6-Cys domains (**Figure S4**). Most A-type domains feature a 5-on-5 β-sandwich whereas B-type domains feature a 4-on-5 β-sandwich fold **(Figure S4A, inset**). A key differentiating feature of these folds is the way in which the first two β-strands are arranged (**Figure 2A, Figure S4A, inset**). In the A-type folds (i.e. Pfs230 D1, D3, D5, D7, D9, D11, and D13), the first canonical β1 strand is split between the two β-sheets (β1 and β1') of the 6-Cys β-sandwich fold before transitioning into the β2 strand. In contrast, in the B-type folds (i.e. Pfs230 D2, D4, D6, D8, D10, D12 and D14), the first two β-strands (β1 and β2) are part of the same β-sheet.

While small deviations from the canonical 6-Cys domains exist, primarily near the perpendicular β-hairpin (**Figure S4B-C**), most of the structural diversity that distinguishes the different Pfs230 6-Cys domains lie in long sequence insertions in loop regions between the β-strands **(Figure 2A)**. These regions were previously coined as insertion domains (IDs) for another 6-Cys domain-containing protein (50, 51) and are present in Pfs230D3, D6, D7, D10 and D11 (**Figure S4D-I**). Many of these IDs (i.e. Pfs230D3, D6, D10, and D11-ID2) contribute to interdomain contacts (**Figure 2B-C**), while others (i.e. Pfs230D11-ID1 and D7) were not observed to interact with other domains (**Figure 2D**). The presence of these IDs mediates the formation of domain clusters in Pfs230.

The Pfs230 C-terminus interacts with Pfs48/45

The interaction site between Pfs48/45 and Pfs230 was delineated at 3.4 Å resolution (**Figure 3A, Figure S3C, Table 1**). Our structure indicates that Pfs230 engages with all three domains of Pfs48/45 through its terminal 6-Cys domains, Pfs230D13 (296 $Å^2$) and Pfs230D14 (1376 $Å^2$) (**Figure 3B**). Pfs48/45 adopts a disc-like conformation in our structure with Pfs230, with Pfs48/45D1 (1057 $Å^2$) and Pfs48/45D3 (478 $Å^2$)

accounting for the majority of contacts with Pfs230, while Pfs48/45D2 (112 Å^2) contributes more modestly (**Figure 3B, Figure S5A, Table S2**). Pfs230 binds to Pfs48/45 on the opposite face of the disc conformation compared to the C-terminus of Pfs48/45, where the GPI linker is located for attachment to the PPM (**Figure 3B**). Previously, two different conformations of Pfs48/45 have been observed in the absence of Pfs230 binding, a compact, disc-like structure solved using X-ray crystallography (14) and an elongated Pfs48/45 structure determined by cryo-EM as bound to a different set of antibodies (15). A comparison of these models with our Pfs230-bound Pfs48/45 structure indicates very similar arrangements of Pfs48/45D1-2 (backbone RMSD = 1.4-1.7 Å for res. 45-288) (**Figure S5B**). However, the position of Pfs48/45D3 relative to Pfs48/45D1-2 varies considerably more. When aligned to Pfs48/45D1-2, there is almost no overlap between Pfs48/45D3 from Pfs230-bound Pfs48/45 and the elongated Pfs48/45 structure while modest positional differences are observed between Pfs48/45D3 of the two disc-like Pfs48/45 structures (backbone RMSD = 3.9 Å for res. 293-428; **Figure S5B**).

The C-terminus of Pfs230 (Pfs230Cterm; res. 3108-3118) – a sequence extending out of the canonical 6-Cys domain – is integral for mediating the Pfs230:Pfs48/45 interaction (**Figure 3C, Figure S6A**). These residues occupy a groove of the Pfs48/45 disc and form extensive interactions with loop 45-49 and strand 65-76 of Pfs48/45D1, loop 246-250 of Pfs48/45D2, and loop 377-380 of Pfs48/45D3 (**Figure 3B**). While accounting for fewer interactions than Pfs230D14, Pfs230D13 residues 2866-2871 and the intervening loop between Pfs230D13 and Pfs230D14 (res. 2977-2984) support complexation by engaging with a portion of a Pfs48/45D3 extended loop (res. 348-371) (**Figure 3D**). Additionally, the Pfs48/45 N-terminus wraps around Pfs48/45D1-2 and, through residues 41-50, forms interactions with loops 2993-2998 and 3108-3114 and strand 3007-3014 of Pfs230D14 (**Figure 3B**). While the N-terminal region of Pfs48/45 remained largely unresolved in previous structural studies of Pfs48/45 without Pfs230 implying flexibility (14, 15), this region is well-resolved in the Pfs230-bound structure and reveals that unlike other A-type domains, Pfs48/45D1 features a different β1 orientation and connectivity (**Figure S5C**), localizing to the interface. An analysis of single nucleotide polymorphisms (SNP) across *P. falciparum* revealed that the interface between Pfs48/45 and Pfs230 is highly conserved (**Figure S5A, S5D**).

Corroborating these structural findings, a recombinantly produced protein construct spanning Pfs230D13-14-Cterm bound to female gametes on which Pfs48/45 is anchored, while similarly produced constructs spanning either Pfs230D1 (previously established to be correctly folded and capable of inducing transmission-blocking immunity (36)) or Pfs230D10 could not (**Figure S7A**). To further confirm the interaction between Pfs230D13-14-Cterm and Pfs48/45, two transgenic parasite lines carrying a truncated *pfs230* gene were created (**Figure S7B-E**). Pfs230$^{\Delta D13/14}$ parasites express Pfs230 up until Pfs230D12, while Pfs230 expressed in Pfs230$^{\Delta Cterm}$ gametocytes only lacks the last 29 C-terminal residues (res. 3107 – 3135), seen as central to the Pfs230:Pfs48/45 interface in our cryo-EM structure. Wildtype Pfs230 is expected to localize on the outside of the PPM, facing into the parasitophorous vacuole, and is expected to co-localize with PPM-bound Pfs48/45. Western blot analysis shows that late-stage Pfs230$^{\Delta D13/14}$ and Pfs230$^{\Delta Cterm}$ gametocytes still contain (truncated) Pfs230. However, saponin-treated parasites with a disrupted parasitophorous vacuole membrane (PVM) lose all Pfs230, demonstrating that Pfs230 is no longer retained on the PPM (**Figure S7F-G**). In fixed immunofluorescence microscopy, full-length and truncated Pfs230 proteins localized in close proximity to Pfs48/45, suggesting that Pfs230 protein trafficking is unaffected in both mutant parasite lines (**Figure S7H**). When the PVM was naturally disrupted upon activation of macrogametes or chemically disrupted in saponin-treated gametocytes, Pfs230 remained bound on the PPM surface in wildtype parasites. In contrast, both Pfs230$^{\Delta D13/14}$ and Pfs230$^{\Delta Cterm}$ gametocytes and gametes lacked surface-bound Pfs230 in these experiments (**Figure 3E-F**). Furthermore, we could not find evidence of a Pfs230-positive population in Pfs230$^{\Delta Cterm}$ gametes in a flow cytometry-based binding assay using over 2,000 macrogametes (**Figure S7I-J**). Together, our structural and *in vivo*

experiments demonstrate that the C-terminal region of Pfs230 is essential for the formation of the Pfs230:Pfs48/45 complex.

Structural characterization of the Pfs48/45D1-ii epitope

The X-ray crystal structure of unliganded RUPA-71 was solved at 2.3 Å resolution (**Table S3**) to use as a high-resolution model to fit and refine into the 3.4 Å resolution Pfs230D13-14:Pfs48/45:RUPA-44:RUPA-71 cryo-EM map (**Figure 4A-B, Table 1**). RUPA-71 predominantly interacts with strand 126-135 of Pfs48/45D1, with additional contacts on Pfs48/45D1 loop 88-90 (**Figure 4A-B, Figure S6B, Table S4**). This is consistent with the previous epitope mapping derived from HDX-MS (15). Heavy chain Complementarity-Determining Region 1 (HCDR1; 108 $Å^2$), HCDR2 (66 $Å^2$), HCDR3 (472 $Å^2$), and Kappa chain CDR1 (KCDR1; 52 $Å^2$) of RUPA-71 all contact Pfs48/45D1, with the extended HCDR3 (20 aa) contributing most key contacts (**Figure 4A, Table S4)**. The epitope of RUPA-71 is highly charged with several negative and positive patches. RUPA-71 binds to these regions through salt bridges formed between RUPA-71 KCDR1 residue K^{32} and HCDR1-3 residues D^{31} and R^{98} and E_{129}, K_{89}, K_{101}, E_{130}, and D_{132} of Pfs48/45D1 (**Figure 4A, Table S4)**. Noticeably, the HCDR3 of RUPA-71 adopts a β-hairpin that forms a β-sheet-like structure with two β-strands of Pfs48/45D1 (res. 126-143) (**Figure 4B**). In addition to intra-chain hydrogen bonds, this β-sheet is held together by five backbone hydrogen bonds between RUPA-71 G^{96}, R^{98}, and Y^{100} and D_{132}, E_{130}, and I_{128} of Pfs48/45D1 (**Figure 4B, Table S4**). Sequence analysis across parasite field isolates revealed only five rare SNPs within the RUPA-71 epitope: K33T (0.015%), K33N (0.007%), S90R (0.007%), K101T (0.029%), and S119T (0.007%), making this epitope highly conserved (**Figure S8A**) (*38*). When compared to RUPA-58, which is the only other D1 antibody that has been structurally characterized to date, RUPA-71 binds to a largely separate epitope, although with some overlap in residue contacts (K_{88}, K_{89}, S_{90}, K_{101}, $D_{132,}$ and R_{140}) that would result in steric clashes (**Figure S8B**)**.** RUPA-58 and RUPA-71, as well as other antibodies that compete with them, require low concentrations to inhibit in the SMFA (IC_{80} < 10 µg/ml), indicating that mAbs that bind to this region of Pfs48/45D1 (res. 86-101 and 126-139) are potently inhibitory (15, 32).

Pfs48/45 epitope accessibility in the Pfs230:Pfs48/45 complex

Next, we investigated how the Pfs230 interaction with Pfs48/45 might affect the accessibility of Pfs48/45-targeting antibodies. An overlay of structures of previously characterized antibodies with the Pfs230-bound structure revealed that Pfs48/45D1, Pfs48/45D2 and Pfs48/45D3-1b epitope antibodies approach from the side of the Pfs48/45 disc and are accessible when Pfs230 is bound **(Figure S8C-E)**. In contrast, many antibodies that target the Pfs48/45D3-1a epitope, including highly potent antibodies TB31F and RUPA-29, would have considerable clashes with both Pfs230D13 and Pfs230D14 in this conformation **(Figure 4C)**.

To determine whether these antibodies can bind to Pfs48/45 in the context of the Pfs230:Pfs48/45 complex, we used the BN-PAGE-based mobility shift assay to study the changes in migratory pattern of Fab-bound endogenous Pfs230:Pfs48/45 complex. To this end, the purified complex was incubated with a tenfold molar excess Fab derived from a range of both potent and non-potent TRA antibodies, spanning almost all currently known epitopes on the complex. As expected, α-Pfs230 Fabs shifted both bands upwards, with the exception of 15C5, which targets epitope III on Pfs230D1 that is shielded by Pfs230D2 and thus incompatible with binding full-length Pfs230 (**Figure 4E**) (17, 20). None of the other tested α-Pfs230 Fabs, targeting epitopes on Pfs230D1, Pfs230D4 and Pfs230D7, disrupted the Pfs230:Pfs48/45 complex, in agreement with the relative orientation of Pfs230 on Pfs48/45 in our structure. The α-Pfs48/45 Fabs did not shift the lower free Pfs230 band, but did affect migration of the upper band. While

some Fabs i) bound to the intact complex (*e.g.* RUPA-44, RUPA-117), others ii) disrupted the Pfs230:Pfs48/45 complex (*e.g.* RUPA-58 and RUPA-50), or iii) showed a heterogeneous effect resulting in Fab-bound and unliganded Pfs230:Pfs48/45 (*e.g.* TB31F, RUPA-47) (**Figure 4E**). The non-potent 10D8, targeting Pfs48/45-D2, could not bind to the Pfs230:Pfs48/45 complex. To confirm the observation that some but not all Pfs48/45-targeted antibodies could disrupt the Pfs230:Pfs48/45 complex, we tested whether a subset of these Fabs could displace Pfs230 on the female gamete surface in a competition assay. In agreement with the BN-PAGE results, RUPA-50, RUPA-57, and RUPA-58 significantly decreased Pfs230 on the gamete surface in a dose-dependent manner, while *e.g.* TB31F, RUPA-46, and RUPA-89 Fabs showed no displacement of Pfs230 (**Figure S8F**).

Intriguingly, TB31F could still partially bind to the Pfs230:Pfs48/45 complex in BN-PAGE (**Figure 4E**) and did not displace Pfs230 on the gamete surface (**Figure S8F**), despite modeling based on our Pfs230-bound Pfs48/45 structure suggesting that significant steric clashes would occur. In this context, it is interesting to note again that it has previously been described how Pfs48/45 can adopt a disc-like conformation (similar to the structure reported here in complex with Pfs230), but also more extended conformations where Pfs48/45D3 can reorient from the rest of the protein. Given that Pfs48/45D1-2 contributes 1169 $Å^2$ of a total 1647 $Å^2$ buried surface area within the Pfs48/45-Pfs230 interface, it is conceivable that Pfs48/45D1-2 is sufficient for Pfs230 binding, allowing for Pfs48/45D3 to retain a range of motion in the complex. Modeling Pfs48/45D3 antibodies onto the previously determined extended conformation of Pfs48/45 with Pfs230D13-14 aligned to its Pfs48/45D1-2 binding site demonstrates that Pfs48/45D3-1a epitope would be accessible in this arrangement (**Figure 4D**). This elongated conformation can also accommodate binding for most anti-Pfs48/45 antibodies that target epitope 1b or Pfs48/45D1-2, with the exception of 10D8 (**Figure 4D, Figure S8I**) (14, 15). Together, this could indicate that Pfs230-bound Pfs48/45 retains flexibility, and that this mobility may allow for the binding of antibodies that would otherwise be blocked in the Pfs230-bound disc-like conformation of Pfs48/45.

Pfs230 membrane retention is non-essential for transmission

Interestingly, the ability of Fab fragments to induce (partial) disruption of the Pfs230:Pfs48/45 complex does not seem to be associated with TRA of the corresponding antibody in SMFAs (**Figure 4E, Figure S8F, Table S1**). For example, when looking at Pfs48/45D3-1a targeting antibodies, the extremely potent antibody TB31F (IC_{80} < 2 µg/ml) shows only partial binding *in vitro* and no displacement of Pfs230 *in vivo*. More importantly, the non-potent RUPA-57 (IC_{80} > 100 µg/ml) is able to fully dissociate the complex *in vitro* and partially on the gamete surface, mimicking the phenotype of *e.g.* the potent RUPA-50 (IC_{80} < 2 µg/ml). The binding characteristics for RUPA-57 suggest that the capability for a mAb to induce Pfs230:Pfs48/45 complex dissociation does correlate with potent transmission-reducing activity.

To investigate whether Pfs230:Pfs48/45 complex disruption could still be a mode of action for some of the transmission-blocking antibodies, we further characterized Pfs230 truncation parasite lines. These parasite lines mimic the most severe outcome of antibody-induced complex dissociation, where all Pfs230 is dissociated from the parasite plasma membrane. Surprisingly, both $Pfs230^{\Delta D13/14}$ and $Pfs230^{\Delta Cterm}$ gametocytes showed high oocyst intensities in multiple independent membrane feeding experiments using *Anopheles stephensi* mosquitoes (**Figure 4F**), in contrast to almost complete lack of oocysts reported for $Pfs230^{KO}$ parasite lines (7). Although our truncation lines showed lower oocyst intensity than wildtype parasites in some experiments, other experiments showed no difference. We confirmed by midgut oocyst genomic DNA extraction and PCR that the oocysts formed by the truncation lines only contained mutant parasite DNA, ruling out accidental wildtype contaminations (**Figure S8G**). To further confirm that Pfs230 remains dissociated from the parasite surface within the mosquito midgut, we added the Pfs230D4-

329 targeting antibody 2A2 into the bloodmeal with either wildtype NF54 and Pfs230$^{\Delta Cterm}$ gametocytes. While
330 2A2 almost completely blocks transmission for wildtype parasites at 10 µg/ml (TR 99.1% (95% CI: 98.5 to
331 99.4)), we observed no significant TRA for 10 µg/ml 2A2 with the Pfs230$^{\Delta Cterm}$ truncation gametocytes (TRA
332 13.0% (95% CI: -5.7 to 28.4)) (**Figure 4G, Figure S8H**). Together, these data indicate that Pfs230:Pfs48/45
333 complex disruption is not the mode of action for functional transmission-blocking α-Pfs48/45 (or α-
334 Pfs230) antibodies.
335
336
337 ***Delineation of Pfs230D4 and D7 epitopes***
338
339 Our cryo-EM studies reveal potent epitopes outside of Pfs230D1 that had not been previously structurally
340 delineated. Fab 2A2 could be resolved in the Pfs230D1-6 map, while Fab 18F25 could be resolved in the
341 Pfs230D7-8 map (**Figure 1I, Table 1**). X-ray crystal structures of unliganded 2A2 and 18F25 Fabs were
342 solved to 1.2 Å and 1.6 Å resolution (**Table S3**), respectively, and docked and refined into the maps. Our
343 cryo-EM structure reveals that 2A2 targets Pfs230D4 (**Figure 5A**), confirming the epitope location
344 previously proposed based on the differential binding and TRA of mAb 2A2 against *P. falciparum* strains
345 that contain SNPs in Pfs230D4 (38). 2A2 buries 824 Å^2 on Pfs230D4, primarily making contacts through
346 the KCDR3 and all HCDR loops (**Figure 5A**, **Table S4**). Most residues contacted by the antibody lie in the
347 canonical perpendicular β-hairpin of Pfs230D4 (β5-β6) and surrounding regions (β2-β4 regions) (**Table S4**).
348 A moderate number of additional contacts are facilitated by the KCDR1/3 within the loop region between
349 the β10 and β11 strands (**Table S4**)**.** Analysis of the MalariaGEN Pf7 database reveals that many SNPs
350 differing from the NF54 strain are found in the 2A2 epitope in various parasite strains (**Figure 5B**). Some
351 of the SNPs are quite rare with frequencies less than 1% (Q1196E, E1198V, E1198D, L1208F, N1209K and
352 N1209Y, Q1250P, Q1250L, Q1255E, K1259I, and K1261N), while others are seemingly more common
353 (H1159D – 53.3%, Y1194S – 59.3%, N1209H – 19.2%, Q1250K – 86.3%, and Q1250E – 12.6%).
354
355 A subset (H1159D, Y1194S, Q1196E, N1209Y, Q1250K) of these SNPs are found in strains of *P. falciparum*
356 in which 2A2 had diminished TRA and perturbed binding to live female gametes in surface
357 immunofluorescence assays (SIFA) (**Figure 5B**) (38). Two mutations (Y1194S and Q1250K) are both present
358 in the NF135 and NF183 strains but are not sufficient to perturb binding of 2A2 **(Figure 5B)**. In contrast,
359 the NF149, NF175, and NF176 strains also encode these mutations, and they also carry 1-3 additional
360 SNPs (H1159D, Q1196E, and N1209Y) found in the 2A2 epitope **(Figure 5B)**. Live gametes obtained from
361 these parasite lines are unable to bind mAb 2A2 in SIFAs (38).
362
363 The epitope of mAb 18F25 localizes to Pfs230D7 (**Figure 5C**) (37). Integrative modeling in the global 3.8 Å
364 global resolution map suggests that 18F25 buries 515 Å^2 on Pfs230D7 through all CDRs of the antibody
365 (**Table S4**). 18F25 primarily engages with the Pfs230D7-ID found in between β4 and β5, with a small
366 amount of interactions localized to the β8-β9 loop (**Figure 5C, Table S4**). Unlike the 2A2 epitope and
367 Pfs230D4 overall, both the 18F25 epitope and Pfs230D7 are more conserved (**Figure 5D**). Only two SNPs
368 in Pfs230D7 identified from the MalariaGEN Pf7 database have frequencies higher than 10% (Y1829N –
369 69.4% and I1870V – 13.5%) and these are not contained within the 18F25 epitope (53). Only three residues
370 within the epitope are reported with mutations in the database. V1801I, V1801L, and V1801A are
371 conservative mutations that have a combined frequency of 5.8% (5.7%, 0.01%, and 0.09%, respectively).
372 Two other SNPs of D1803N and N1804D are also conservative mutations that occur relatively infrequently
373 (D1803N – 0.01% and N1804D – 0.2%).
374

375 To better understand how the SNPs found in the 18F25 epitope affect the affinity of the mAb to Pfs230D7,
376 we performed surface plasmon resonance (SPR) experiments (**Figure 5D**) using Pfs230D7 constructs
377 expressed using a wheat germ cell-free protein expression system (54). SPR experiments utilizing the
378 18F25 Fab and WT Pfs230D7 revealed that the antibody binds to its native epitope with single digit
379 nanomolar affinity (K_D = 1.8 nM). Mutation of the most polymorphic residue, V1801, to the three different
380 SNPs identified in the MalariaGEN Pf7 database revealed a negligible effect on binding affinity, with Fab
381 18F25 maintaining wild-type level nanomolar binding affinity (V1801A: K_D = 3.6 nM, V1801L: K_D = 2.6 nM
382 and V1801I: 0.9 nM, respectively). While the rarer SNPs D1803N and N1804D have a more moderate effect
383 (K_D = 181 nM and K_D = 92 nM, respectively), nanomolar-level binding affinity is still maintained in these
384 cases. Together, our data elucidate the 2A2 and 18F25 epitopes on Pfs230D4 and D7, respectively,
385 providing structural insights into Pfs230-directed antibody responses outside of Pfs230D1. In contrast to
386 2A2, mAb 18F25 targets a conserved epitope with rare naturally occurring non-synonymous SNPs that
387 have small impact on 18F25 binding affinity.
388
389 ***Potent Pfs230 antibodies target membrane distal epitopes***
390
391 mAb 2A2, while showing strain-dependent TRA, was highly potent in SMFAs utilizing the NF54 strain (IC_{80}
392 = 1.9 µg/ml (38)). The potency was on par with the highly potent RUPA-97 that targets Pfs230D1 (IC_{80} =
393 0.7 µg/mL (20)), suggesting that a common feature of these mAbs might be responsible for the high
394 potency. These two mAbs, despite binding different domains, bind to the same side of Pfs230 with a
395 similar angle of approach (**Figure 6A**). mAb 18F25 (IC_{80} < 30 µg/ml (37)) also binds to the same face of
396 Pfs230, while differing slightly in its angle of approach (**Figure 6A**). Interestingly, Pfs230D1-directed mAbs
397 of lower potency, such as RUPA-38 (IC_{80} > 100 µg/mL) (20), bind to the opposite face of where RUPA-97,
398 2A2, and 18F25 bind to Pfs230 (**Figure 6A**). This trend is generally applicable to α-Pfs230D1 mAbs
399 published to date (**Figure S9**) (17).
400
401 These Pfs230-targeting mAbs have been demonstrated to be complement-dependent for their TRA (20,
402 36-38, 40). Previously, it has been shown that for efficient C1q deposition on an antigenic surface, the first
403 step in the classical complement activation pathway, IgGs need to form into ordered hexameric antibody
404 structures (55, 56). Intriguingly, the epitopes of potent mAbs RUPA-97, 2A2, and 18F25 are localized to
405 the opposite face of where Pfs48/45 and presumably the PPM would be (**Figure 6A**). In contrast, the
406 epitope of non-potent RUPA-38 is localized near the presumed location of the PPM (**Figure 3A**). These
407 observations led us to hypothesize that the angle of approach of the antibody is a determinant of Pfs230-
408 directed antibody potency, as antibodies that are near the PPM might be prevented from efficient
409 recruitment of complement components and thus complement activation. To test this hypothesis, we
410 selected five different mAbs targeting Pfs230D1 with different potencies (RUPA-97 (IC_{80} = 0.7 µg/mL),
411 rh4F12 (IC_{80} = 55 µg/mL), LMIV230-01 (IC_{80} = 48 µg/mL), RUPA-38 (IC_{80} > 100 µg/mL)), and LMIV230-02
412 (IC_{80} > 1000 µg/mL) (19, 20), expressed these as IgGs of the same complement-fixing subclass, and tested
413 antibody binding, C1q recruitment and C3 deposition on live female NF54 gametes. All antibodies except
414 LMIV230-02 bound gametes with similar intensity (**Figure 6B**), which is in agreement with previously
415 determined *in vitro* affinities (20). In contrast, the highly potent antibody RUPA-97 and moderately potent
416 antibodies rh4F12 and LMIV230-01 were able to recruit C1q and deposit C3 on the surface, while the non-
417 potent RUPA-38 was not able to do so efficiently (**Figure 6C-D**). These findings, as implied by the
418 Pfs230:Pfs48/45 complex structure, suggest that the angle of approach relative to the PPM might be a
419 critical determinant for potency in complement-dependent Pfs230-directed antibodies.
420
421

422 # DISCUSSION

423

424 Targeting human-to-mosquito transmission, a developmental bottleneck in the *Plasmodium* life cycle, is
425 a promising intervention strategy for malaria control and elimination. Here, we reveal the structural
426 disposition of the heterodimer complex Pfs230:Pfs48/45, which is essential for *P. falciparum* transmission
427 and a major target for malaria transmission-blocking vaccine development. Using advances in molecular
428 parasitology and cryo-EM, we were able to circumvent recombinant expression by purifying the
429 approximately 410 kDa large, membrane-bound Pfs230:Pfs48/45 complex from its native source, late-
430 stage *P. falciparum* gametocytes. Previously, similar methods have been used to elucidate the structure
431 of the *Plasmodium* Translocon of Exported Proteins (PTEX) complex (57) and the soluble RhopH complex
432 (58, 59), both crucial protein complexes within the *Plasmodium* life cycle non-amenable to standard
433 recombinant protein production. Using genome engineering to enable the purification of endogenous
434 proteins for cryo-EM studies has also found traction in research on other organisms, including human cells
435 (60), and bacterial pathogens like *Pseudomonas spp.* (61) and *Mycobacteria spp.* (62). This highlights the
436 opportunities that this approach, combined with recent advances in the field of structural biology
437 including bottom-up structural proteomic platforms such as cryoID (63) and protein folding prediction
438 software such as AlphaFold 3 (64), may offer to the many other *Plasmodium* proteins refractory to
439 recombinant expression.

440

441 Our structure reveals how insertion domains present within Pfs230 6-Cys domains mediate inter-domain
442 interactions **(Figure 2)** as seen before with the Pf12:Pf41 heterodimer complex, which are two other
443 malarial proteins that are composed of 6-Cys domains (50, 51). Additionally, inter-protein contacts
444 between Pfs230 and Pfs48/45 appear to be mediated by regions outside of the canonical 6-Cys fold; we
445 have shown how the C-terminal extension of Pfs230 is critical for binding, and observed that the N-
446 terminal extension of Pfs48/45 also localized to this interface **(Figure 4B-C, Figure S6A)**. This suggests that
447 regions outside of the canonical 6-Cys fold may have been introduced to provide functional roles by
448 mediating interactions, which could be a generalizable property of 6-Cys domain family of proteins.

449

450 Although it is currently unknown what exact cellular process the Pfs230:Pfs48/45 complex is involved in,
451 knockout studies in *P. falciparum* and the rodent malaria parasite *Plasmodium berghei* suggest the
452 Pfs230:Pfs48/45 complex is involved in microgamete-to-macrogamete adhesion and microgamete-to-RBC
453 adhesion resulting in exflagellation centers (7, 8, 65). The presented structure will enable the design of
454 domain clusters with more precision than previously possible for the generation of genetically modified
455 parasite lines that can interrogate Pfs230 function. Our structure also shows that the N-terminal domains
456 are membrane-distal, potentially allowing interactions with other elements. This is in line with previous
457 descriptions of some functional complement-independent α-Pfs230D1 antibodies, suggesting that
458 Pfs230D1 might be involved in some protein interactions that are disrupted upon binding of these
459 antibodies (16, 34). Furthermore, competition assays with recombinant Pfs230Pro-D1-2 was previously
460 shown to inhibit the formation of exflagellation centers (16), further suggesting that the N-terminus of
461 Pfs230 might be involved in cell-to-cell adhesion. The C-terminal Pfs230 domains are involved in the
462 Pfs48/45-based membrane anchoring onto the PPM. We showed that functional activity of complement-
463 independent Pfs48/45 antibodies does not correlate with their ability to disrupt the Pfs230:Pfs48/45
464 complex. The transgenic parasite lines expressing truncated Pfs230, which lose Pfs230 membrane-
465 retention but are able to efficiently infect *Anopheles* mosquitoes, fully support the notion that complex-
466 dissociation is not a mode of action for transmission-blocking antibodies. These observations imply that
467 Pfs48/45 does not merely serve as an anchor for Pfs230 membrane retention, but carries out an additional
468 critical function during parasite transmission that anti-Pfs48/45 antibodies can potently inhibit.

Surprisingly, there is a stark difference between the truncation parasite lines Pfs230$^{\Delta D13/14}$ and Pfs230$^{\Delta Cterm}$ on one hand that do infect mosquitoes, and the previously reported Pfs230^{KO} parasite lines on the other hand that almost completely lost capability for parasite transmission (7). Future studies should focus on uncovering the roles of individual domains of Pfs230 and Pfs48/45 during parasite transmission.

Next to characterizing the full-length structure of the Pfs230:Pfs48/45 heterodimer, we also molecularly characterized the epitope of multiple transmission-blocking antibodies. The potent Pfs48/45D1 antibody, RUPA-71, binds an adjacent epitope to the previously characterized mAb, RUPA-58 (*15*). All highly potent Pfs48/45D1 antibodies compete with either RUPA-58 or RUPA-71, indicating that binding to this conserved portion of Pfs48/45D1 is associated with transmission-reducing activity (*15*). Additionally, we structurally characterized potent epitopes outside of Pfs230D1 found on Pfs230D4 and Pfs230D7 targeted by murine mAbs, 2A2 and 18F25, respectively. While mAb 2A2 is notably potent when used against the NF54 strain, the epitope is highly polymorphic with many Pfs230D4 SNPs observed in field isolates (38) and described in the MalariaGEN Pf7 database (53). In contrast, both Pfs230D7 and the 18F25 epitope are highly conserved and may represent a yet unexplored opportunity for subunit vaccine development. Excitingly, the few naturally occurring SNPs found in the 18F25 epitope were non-detrimental for antibody binding *in vitro* **(Figure 5D)**. However, in comparison to 2A2 and highly potent Pfs230D1-bin I binders, 18F25 exhibits approximately 10-fold lower potency. The ability to design Pfs230 probes based on the full-length structure will now enable discovery efforts seeking more potent antibodies. In addition, the structure of the full Pfs230:Pfs48/45 heterodimer complex reported here with structure-function relationships of antibody inhibition, now enables a more fulsome opportunity for structure-guided immunogen design, which has been transformative in vaccinology during the development of *e.g.* SARS-CoV-2, and respiratory syncytial virus vaccines (66, 67).

Immunogens based on Pfs230 and Pfs48/45 have already shown promising results in clinical trials (44-47), though the induced inhibitory activity was incomplete and the durability of the response remains uncertain. Our findings suggest that current TBV candidates can be further optimized, for example by including Pfs230 domains that were previously thought to be unable to induce functional transmission-blocking antibodies (36-38), or by rational structure-based immunogen design (68, 69). To date, most Pfs48/45-based interventions focus on Pfs48/45D3, but Pfs48/45D1 epitopes may be beneficial inclusions into future Pfs48/45-based immunogens. Currently, in the case of Pfs230 domains, Pfs230D1, D4, D7, and D12 have been demonstrated to elicit potent antibodies (20, 36-38). Interestingly, these Pfs230 domains share a common feature in that they are membrane distal, suggesting that domains present on this side should be prioritized for subunit vaccine development. By this logic, Pfs230D8 and D9 may also be relevant targets (**Figure 6**). Future immunogen design efforts should integrate inter-domain structural elements to present well-folded epitopes. Approaching immunogen design through stabilizing structural clusters, guided by the structure reported here, instead of individual domains will help eliminate the presentation of non-neutralizing epitopes that are absent endogenously, as previously evidenced by the elicitation of Pfs230D1-binIII mAbs (15C5, LMIV230-02, and 230AS-26) and 230AL-20 by a Pfs230D1-only antigen (**Figure S9**). The presented Pfs230:Pfs48/45 structure might also allow for future protein engineering campaigns that graft multiple potent epitopes onto a single chimeric immunogen (70), or use stabilizing mutations in conjunction with display on nanocages (71). Additionally, advances in mRNA vaccination approaches combined with precise immunogen design might allow for the *in situ* expression of stable, native Pfs230:Pfs48/45 co-assemblies. Ultimately, the aim will be to create the most potent next-generation TBVs possible to aid in meeting the ambitious goals of malaria elimination and eradication.

517 ***Limitations of the study***

518 A limitation of our structure is the low resolution obtained for the Pfs230D9-12 domains (global resolution
519 of 4.7 Å). This prevented building an atomic model for these domains, limiting the information that could
520 be confidently extracted from this part of the map. Instead, we combined this low-resolution map with
521 an AF-based modeling approach to obtain a backbone model with reasonable confidence regarding the
522 domain orientations in this region of Pfs230. Additionally, while the presence of 2A2 does not seem to
523 affect the overall structure of Pfs230:Pfs48/45 significantly **(Figure S3A-B)**, other antibodies in our
524 structure could have potentially altered the structure of Pfs230:Pfs48/45 compared to its unliganded
525 state. An unliganded Pfs230:Pfs48/45 heterodimer structure reported by others in parallel to our study
526 described a similar overall structure for the heterodimer complex, indicating that antibody binding in our
527 structure did not have a dramatic effect (72). One notable difference in the 6Fab-bound Pfs230:Pfs48/45
528 structure compared to the unliganded structure is the increased flexibility within the Pfs230D9-14 region,
529 specifically between Pfs230D12 and D13. In 2D classes of the full complex, the constant region of anti-
530 Pfs48/45 Fab, RUPA-71, appears to be in proximity to the Pfs230D1-6 and Pfs230D7-8 clusters of the
531 molecule, potentially causing steric hinderance. Additionally, loops at the periphery of Pfs48/45D1 which
532 come into close proximity of Pfs230D13-14 is not localized to the same region in the antibody-bound
533 structure, pushing Pfs48/45 away from Pfs230. We propose that this steric hindrance induced by RUPA-
534 71 binding decompresses the Pfs230D9-12 cluster, resulting in a more dynamic disposition, and
535 consequently, poorer resolution of this portion of the map. Finally, we purified the Pfs230:Pfs48/45 from
536 late-stage gametocytes instead of gametes, for practical reasons. However, during gamete formation the
537 Pro-domain of Pfs230 is proteolytically cleaved (73), and therefore our structure does not fully
538 recapitulate the mature protein species on gamete surfaces. How these additional Pro-domain residues
539 add onto the structure and if these influence the overall Pfs230:Pfs48/45 conformation, remains currently
540 unknown.

541
542

RESOURCE AVAILABILITY

Lead contact

Further information and requests for resources and reagents should be directed to and will be fulfilled by the lead contact, Jean-Philippe Julien (jean-philippe.julien@sickkids.ca) upon reasonable request.

Materials availability

All unique reagents generated in this study are available from the lead contact with a completed Materials Transfer Agreement.

Data and code availability

- Previously unpublished antibody sequences are available in Table S6. Crystal and cryo-EM structures have been deposited in the Protein Data Bank and are publicly available as the date of publication. EMDB and PDB IDs are listed in Table 1 and Table S3. The proteomics dataset has been deposited in the ProteomeXchange Consortium via the PRIDE partner repository (74) with the dataset identifier PXD060716.
- This paper does not report original code.
- Any additional information required to reanalyze the data reported in this paper is available from the lead contact upon reasonable request.

ACKNOWLEDGEMENTS

We thank Roos de Jong and Sanne Grievink for assistance with protein purification; Laura Pelser, Astrid Pouwelsen, Jacqueline Kuhnen, Jolanda Klaassen, and Wouter Graumans for mosquito rearing and dissections; April Yu for assisting in 18F25 Fab structural determination; Hikaru Nagaoka and Takafumi Tsuboi for their assistance and guidance in Pfs230D7-18F25 binding characterization; Dick Zijlmans for assistance with Mass spectrometry data analysis; Aran Labrijn (Genmab) for antibody sequencing; the Raboudumc Technology Centers for Microscopy and Flow Cytometry for access to their instruments; Samir Benlekbir and Zhijie Li from the SickKids Nanoscale Biomedical Imaging Facility for assistance and insights during cryo-EM data collection; Greg Wasney and James Magnus Jorgensen at the Structural & Biophysical Core (SBC) Facility; past and present members of the Molecular and Cellular Parasitology (Radboudumc) and the Malaria Transmission (Radboudumc) teams for insightful discussions. This work was supported by a Radboudumc Master-PhD grant awarded to E.T.B. and a VIDI grant from the Netherlands Organisation for Scientific Research to M.M.J. (fellowship number 192.061). This work was also undertaken, in part, thanks to funding from a Canadian Institutes for Health Research grant (428410) and was supported by the Canada Research Chair program awarded to J.L.R. and J-P.J. E.T.B. was further supported by a FEMS Research and Training Grant. The Pfs230D7 production and SPR analysis were performed with support from AMED (JP24wm0225045). R.Y. was supported by a Canada Graduate Scholarship - Master's (CGS-M). S.H. was supported by a Canada Graduate Scholarship - Doctoral. C.M.A. is supported by a VENI grant from the Netherlands Organisation for Scientific Research (VI.Veni.222.381). The Vermeulen lab is part of the Oncode Institute, which is partly funded by the Dutch Cancer Society (KWF). X-ray diffraction experiments for the 2A2 and 18F25 Fab datasets were performed at the AMX-17-ID-1 at the National Synchrotron Light Source II, a U.S. Department of Energy (DOE) Office of Science User Facility operated for the DOE Office of Science by Brookhaven National Laboratory under Contract No. DE-SC0012704. X-ray diffraction experiments for RUPA-71 Fab was performed using beamline CMCF-ID at the Canadian Light Source, a national research facility of the University of Saskatchewan, which is supported by the Canada Foundation for Innovation (CFI), the Natural Sciences and Engineering Research Council (NSERC), the National Research Council (NRC), the Canadian Institutes of Health Research (CIHR), the

Government of Saskatchewan, and the University of Saskatchewan. Molecular graphics were generated using UCSF ChimeraX, developed by the Resource for Biocomputing, Visualization, and Informatics (University of California, San Francisco) with support from the National Institutes of Health (R01-GM129325) and the Office of Cyber Infrastructure and Computational Biology, National Institute of Allergy and Infectious Diseases. The size exclusion chromatography instrument was accessed at the Structural and Biophysical Core Facility, The Hospital for Sick Children, and EM data was collected at the Nanoscale Biomedical Imaging Facility, The Hospital for Sick Children, supported by the Canada Foundation for Innovation and Ontario Research Fund.

AUTHORS CONTRIBUTION

Conceptualization: E.T.B., R.Y., S.H., M.M.J., J-P.J.; **Investigation**: E.T.B., R.Y., S.H., N.I.P., R.S., G-J.v.G., A.M., T.Y., O.T.W., R.C.v.D., M.R.I., C.M.A., P.W.T.C.; **Formal Analysis**: E.T.B., R.Y., S.H., F.H, D.I., M.J.; **Resources**: M.V., T.B., J.L.R.; **Writing – Original Draft**: E.T.B., R.Y., S.H., M.M.J., J-P.J.; **Writing – Review & Editing**: E.T.B., R.Y., S.H., F.H., D.I., M.J., N.I.P., C.M.A., T.B., J.L.R., T.W.A.K., M.M.J., J-P.J.; **Supervision**: M.V., T.B., E.T., J.L.R., T.W.A.K., M.M.J., J-P.J.; **Funding acquisition:** E.T.B., M.M.J., J-P.J.

DECLARATION OF INTERESTS

The authors declare no competing interests.

608 # MAIN FIGURES

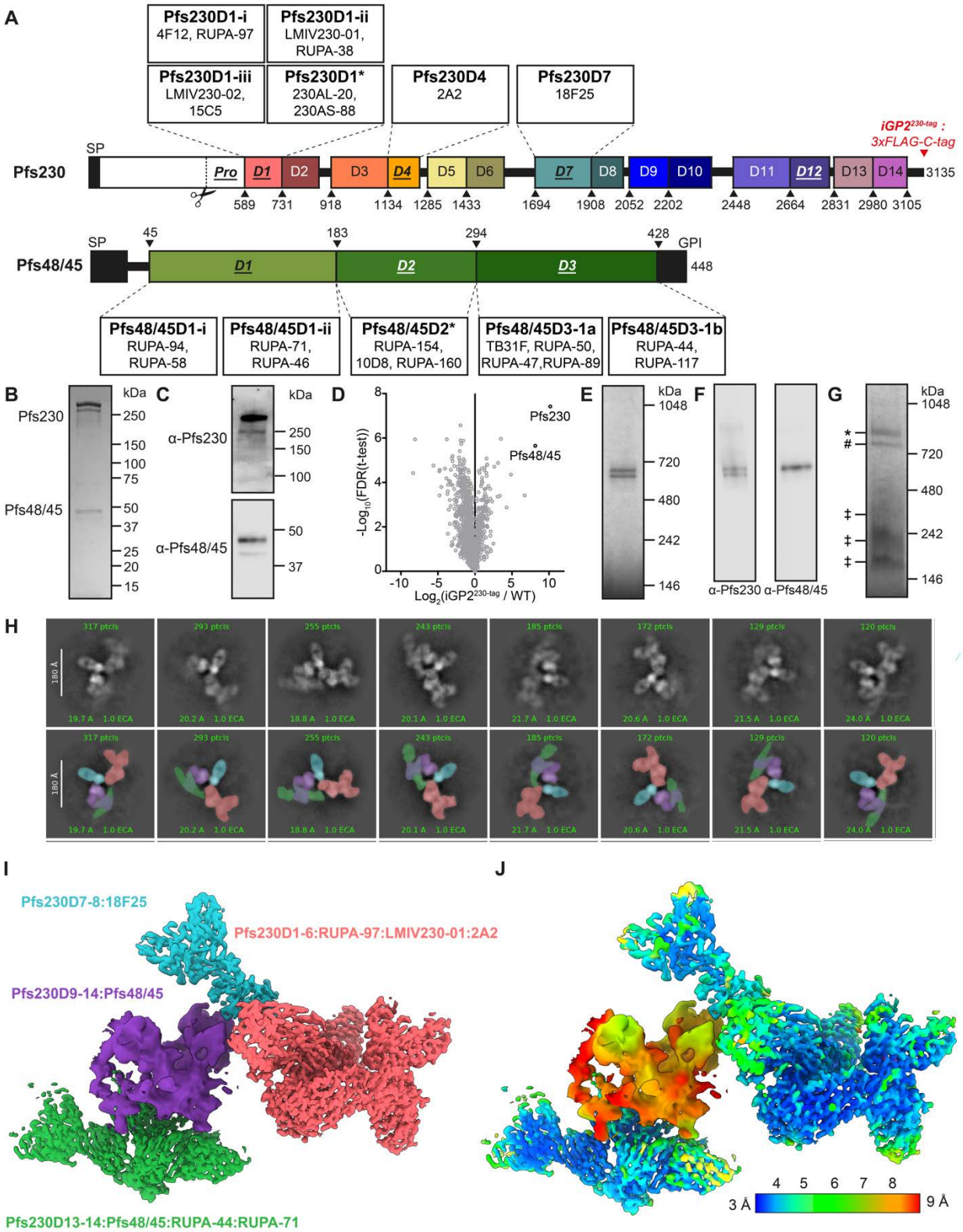

609
610 **Figure 1: Purification of Pfs230:Pfs48/45:6Fab complex from *P. falciparum* gametocytes. (A)** Schematic illustration
611 of Pfs230 and Pfs48/45 domains (not to scale), epitopes found within these domains, and examples of mAbs

612 targeting these epitopes (see also **Table S1**). Asterisks indicate multiple additional distinct epitopes at the indicated
613 domain. Domains that contain known transmission-blocking epitopes are indicated by underlined italic. Arrows
614 indicate amino acid number of the approximate start of the domain as determined by (*13*). SP = Signal peptide, GPI
615 = Glycosylphosphatidylinositol anchor site. **(B-C)** Coomassie Blue (B) and immunoblot (C) staining of a denaturing
616 SDS-PAGE gel of FLAG-tag purified Pfs230:Pfs48/45 complex. **(D)** Mass spectrometry analysis of FLAG-tag purified
617 Pfs230:Pfs48/45 complex. The volcano plot shows the $\log_2$ fold change plotted against the $\log_{10}$ fold false discovery
618 rate, comparing FLAG-tag co-immunoprecipitation of iGP2$^{230\text{-tag}}$ versus NF54/WT parasites. **(E-G)** Blue-Native PAGE
619 analysis, showing (E) Coomassie blue and (F) α-Pfs230 and α-Pfs48/45 immunoblot staining of neat purified
620 Pfs230:Pfs48/45 complex, or (G) Coomassie blue staining of eluted complex incubated with molar excess of six Fabs
621 (RUPA-97, LMIV230-01, 2A2, 18F25, RUPA-44, and RUPA-71). Symbols: * = Pfs230:Pfs48/45:6Fab ; # = Pfs230:4Fab ;
622 ‡ = excess Fab fragment. **(H)** Eight representative 2D class averages generated from cryo-EM of HPLC-SEC purified
623 Pfs230:Pfs48/45:6Fab complex. Structures are annotated in the lower row, with orange highlighting Pfs230D1-
624 6:RUPA-97:LMIV230-01:2A2, blue Pfs230D7-8:18F25, purple Pfs230D-13-14:Pfs48/45, and green Pfs230D13-
625 14:Pfs48/45:RUPA-44:RUPA-71. **(I)** Composite CryoEM map of the Pfs230:Pfs48/45 complex coloured according to
626 the same colouring scheme. **(J)** Local resolution of each map coloured according to scale. Maps are contoured to 5
627 Å around built models. *See also Figure S1-3 and Table S1*.
628

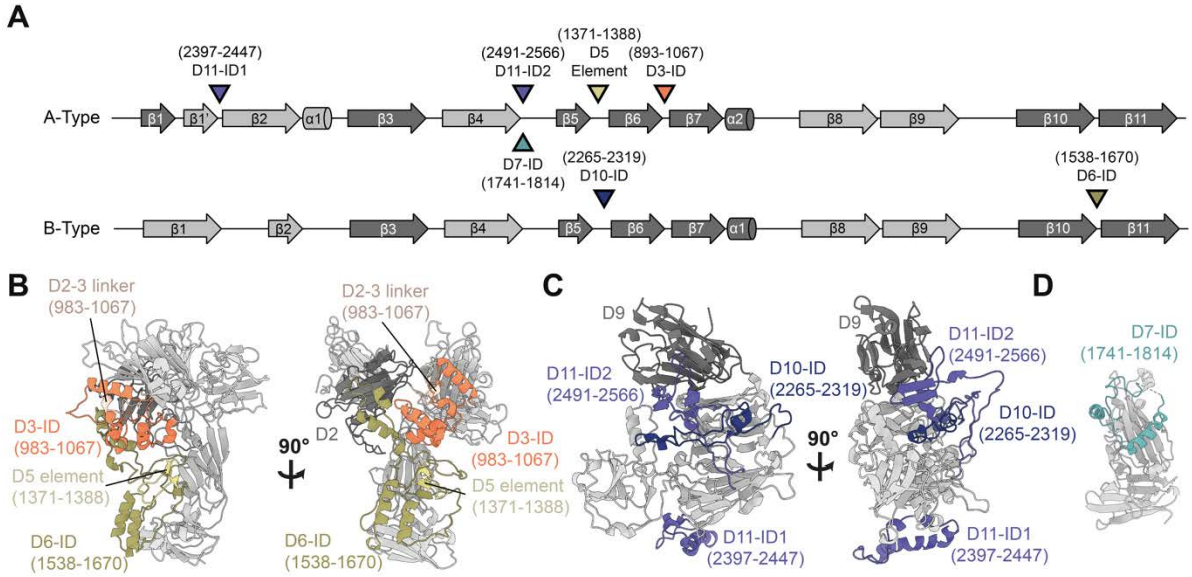

Figure 2. **Insertion domains (IDs) facilitate Pfs230 domain clustering (A)** Secondary structural elements of A- and B-type domains, with insertion domains (IDs) or non-canonical structural element (D5 element) found in respective domains indicated by coloured arrows and with residue range in brackets. **(B)** The D2-D3 linker (light orange), D3-ID (orange), D5 structural element (yellow), and D6-ID (dark yellow) interact with one another, forming a structural fold that packs against the base of D2 (dark grey). **(C)** The D10-ID (blue) and Pfs230D11-ID2 (purple) interact with one another, positioning the D11-ID2 (purple) to form an extended β-sheet with D9 (dark grey). **(D)** D7-8 (silver) and D7-ID (cyan) lack interdomain contact. *See also Figure S4.*

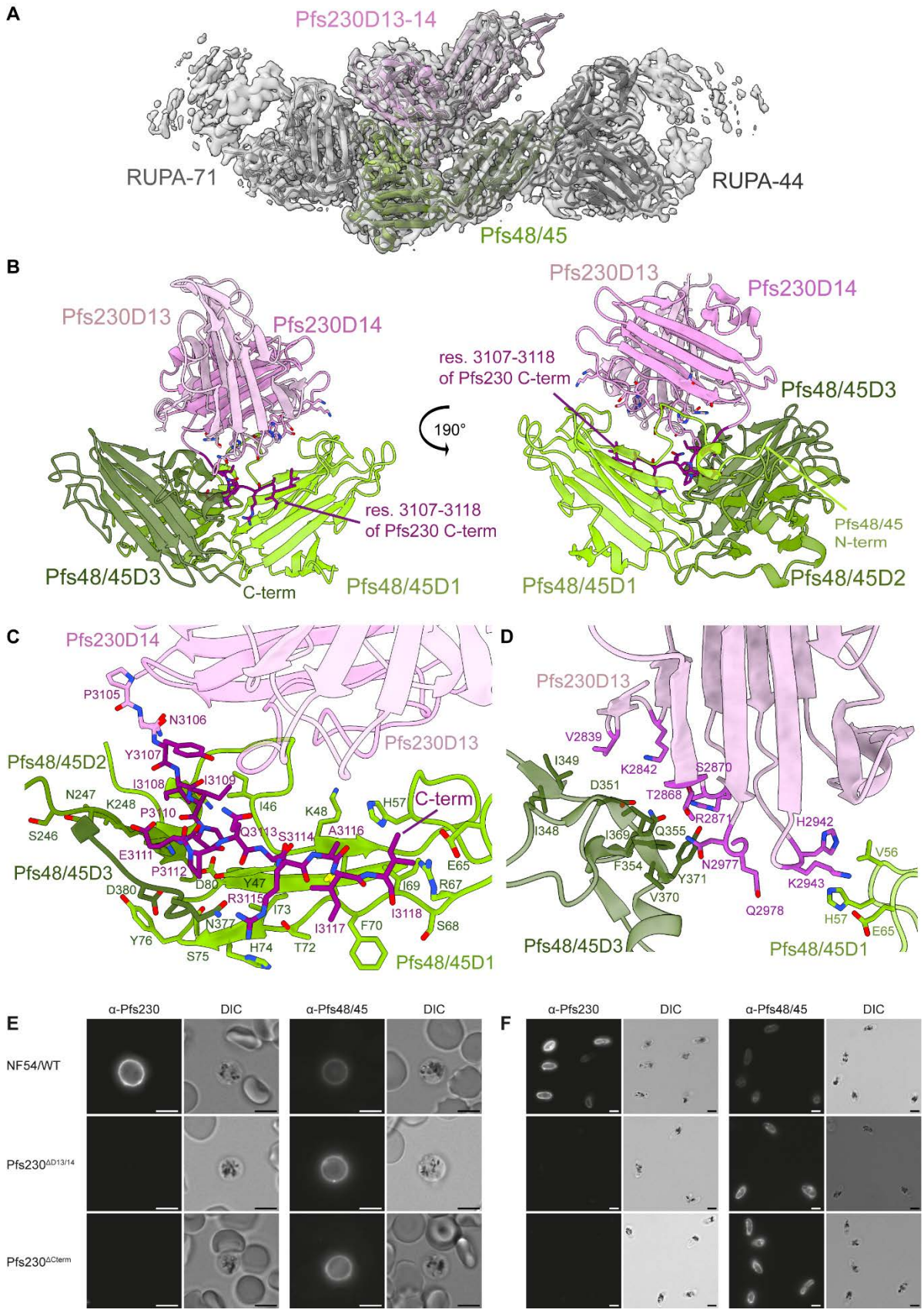
A
Pfs230D13-14
RUPA-71
RUPA-44
Pfs48/45
B
Pfs230D13
Pfs230D14
res. 3107-3118
of Pfs230 C-term
190°
Pfs48/45D3
C-term
Pfs48/45D1
Pfs48/45
N-term
Pfs48/45D2
C
Pfs230D14
Pfs230D13
Pfs48/45D2
Pfs48/45D3
C-term
Pfs48/45D1
D
Pfs230D13
Pfs48/45D3
Pfs48/45D1
E
α-Pfs230
DIC
α-Pfs48/45
DIC
NF54/WT
Pfs230ΔD13/14
Pfs230ΔCterm
F
α-Pfs230
DIC
α-Pfs48/45
DIC

639

640 **Figure 3: Molecular description of the Pfs230 and Pfs48/45 interaction**. **(A)** Overview of the structure of Pfs48/45
641 (yellow green, olive drab, and dark olive drab for domains 1-3, respectively) bound to Pfs230D13-14 (plum), RUPA-
642 71 Fab (dark grey), and RUPA-44 Fab (light grey) with the cryo-EM map shown in grey. **(B)** Pfs48/45 bound to
643 Pfs230D13-14 with key Pfs230 contact residues shown as sticks and the C-terminal region of Pfs230 highlighted in
644 dark magenta. **(C-D)** binding interactions between Pfs48/45 and Pfs230D14-Cterm (C) and Pfs230D13 (D) with key
645 residue contacts shown as sticks. **(E-F)** Representative suspension immunofluorescence microscopy images of
646 NF54/WT, $230^{\Delta D13/14}$, and $230^{\Delta Cterm}$ female macrogametes (E) and saponin-treated stage V gametocytes (F). Parasites
647 were incubated with 15 µg/ml 18F25-DyLight488 (α-Pfs230) or 45.1-DyLight488 (α-Pfs48/45). All images per
648 experiment were taken and analyzed with the same settings. Scale bar represents 5 µm. *See also Figure S5-7 and*
649 *Table S2.*
650

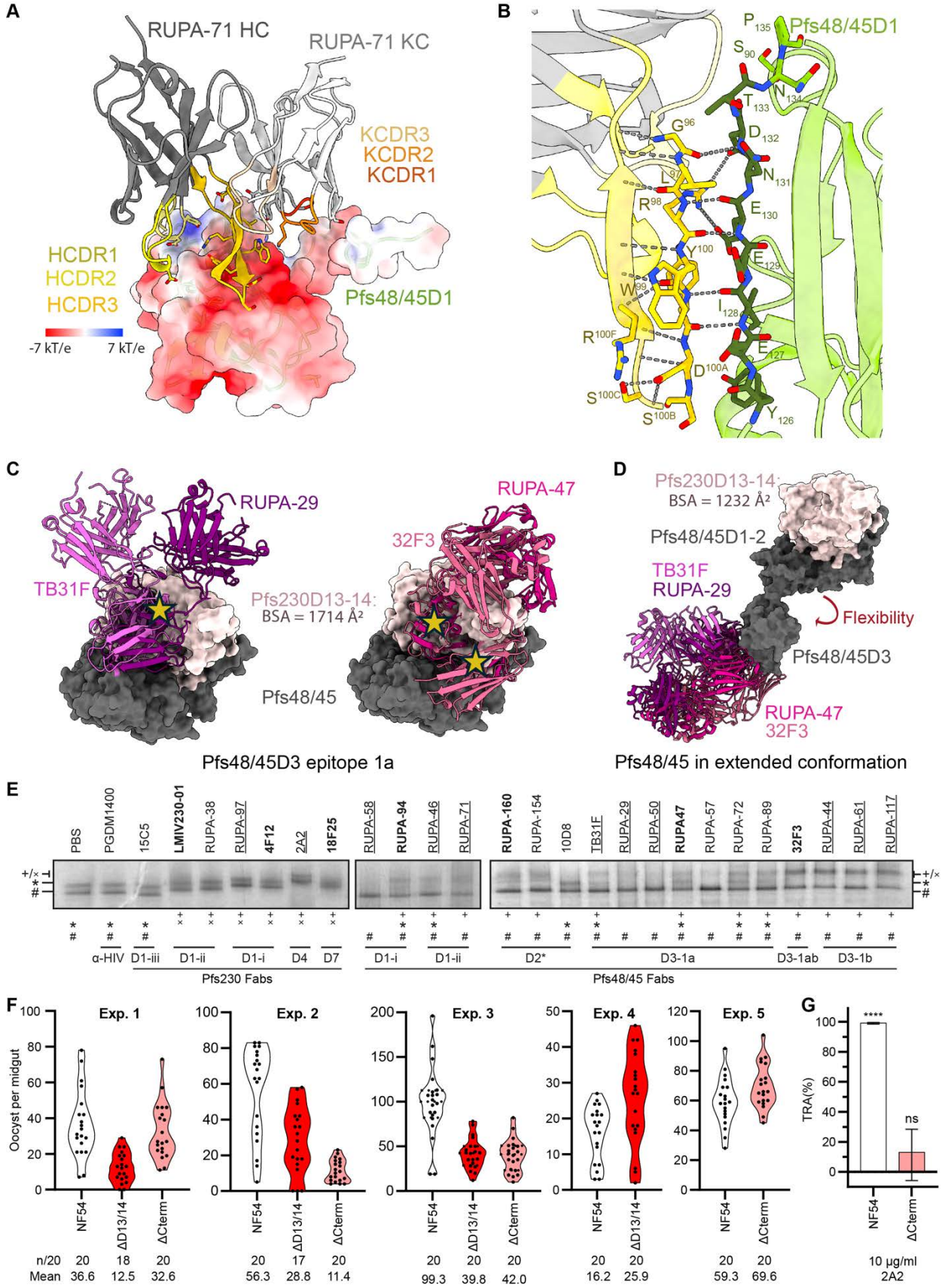
A
RUPA-71 HC
RUPA-71 KC
KCDR3
KCDR2
KCDR1
HCDR1
HCDR2
HCDR3
Pfs48/45D1
-7 kT/e
7 kT/e
B
Pfs48/45D1
C
RUPA-29
TB31F
Pfs230D13-14:
BSA = 1714 Å²
Pfs48/45
RUPA-47
32F3
Pfs48/45D3 epitope 1a
D
Pfs230D13-14:
BSA = 1232 Å²
Pfs48/45D1-2
TB31F
RUPA-29
Flexibility
Pfs48/45D3
RUPA-47
32F3
Pfs48/45 in extended conformation
E
PBS
PGDM1400
15C5
LMIV230-01
RUPA-38
RUPA-97
4F12
2A2
18F25
RUPA-58
RUPA-94
RUPA-46
RUPA-71
RUPA-160
RUPA-154
10D8
TB31F
RUPA-29
RUPA-50
RUPA47
RUPA-57
RUPA-72
RUPA-89
32F3
RUPA-44
RUPA-61
RUPA-117
α-HIV
D1-iii
D1-ii
D1-i
D4
D7
D1-i
D1-ii
D2*
D3-1a
D3-1ab
D3-1b
Pfs230 Fabs
Pfs48/45 Fabs
F
Exp. 1
Exp. 2
Exp. 3
Exp. 4
Exp. 5
Oocyst per midgut
NF54
ΔD13/14
ΔCterm
n/20 20 18 20
Mean 36.6 12.5 32.6
20 17 20
56.3 28.8 11.4
20 20 20
99.3 39.8 42.0
20 20
16.2 25.9
20 20
59.3 69.6
G
TRA(%)
****
ns
NF54
ΔCterm
10 µg/ml
2A2

651

652 **Figure 4: Molecular characterization of anti-Pfs48/45 epitopes in the Pfs230-bound state of Pfs48/45**. **(A)** Structure
653 of RUPA-71 bound to Pfs48/45D1 depicted as surface and coloured by electrostatic potential calculated by Adaptive
654 Poisson-Boltzmann Solver (APBS) and visualized in ChimeraX. **(B)** RUPA-71 HCDR3 (gold) bound to Pfs48/45D1
655 (yellow green) with key residues shown as sticks and hydrogen bonds or electrostatic interactions indicated by
656 dashed lines. **(C-D)** Model of Pfs48/45 (dark gray, depicted in surface) bound to Pfs230D13-14 (misty rose, depicted
657 in surface) in the disc-like (C) or extended (D) conformation bound to Pfs48/45D3-1a binders (TB31F (orchid, PDB ID:
658 6E63), RUPA-29 (dark magenta, PDB ID: 7UXL), RUPA-47 (violet red, PDB ID: 7UNB), and 32F3 (pale violet red, PDB
659 ID: 7ZWI)). Clashes are indicated with yellow stars. **(E)** Blue Native PAGE-based mobility shift assay of FLAG-tag
660 purified Pfs230:Pfs48/45 complex, incubated with a tenfold molar excess of individual anti-Pfs230 or anti-Pfs48/45
661 Fab fragments. The first lane shows the Pfs230:Pfs48/45 complex with the addition of a mock liquid (PBS) as a
662 reference, and PGDM1400, an anti-HIV envelope protein targeted Fab, was included as negative control. Fabs are
663 sorted by antigen, epitope, and potency (underlined: IC_{80} < 10 µg/ml; bold: IC_{80} = 10-100 µg/ml, others: IC_{80} > 100
664 µg/ml; See also **Table S1**). Note that due to the nature of Blue Native PAGE, the hydrodynamic radius and therefore
665 the angle of approach can heavily influence the extent of Fab-induced mobility retardation. The symbols #, *, ×, and
666 + denote Pfs230, Pfs230:Pfs48/45, Pfs230:Fab, and Pfs230:Pfs48/45:Fab, respectively. **(F)** Infection of *An. stephensi*
667 mosquitoes with wildtype NF54 (white), $Pfs230^{\Delta D13/14}$ (red), and $Pfs230^{\Delta Cterm}$ (pink) as measured in five independent
668 standard membrane feeding experiments with 20 mosquitoes per condition each. Dots represent the number of
669 oocysts per midgut of an individual mosquito. Note that data from experiment 4 are the same as the FCS controls in
670 Figure S8H experiment 2. N denotes the number of mosquitoes that carries at least 1 oocyst, mean is the mean
671 number of oocyst per midgut. **(G)** Transmission reducing activity of 10 µg/ml Pfs230D4-targeting mAb 2A2 for
672 mosquito infections with NF54 wildtype (white) and Pfs230ΔCterm (pink) gametocytes, in the presence of active
673 human complement. Mean with 95% confidence intervals are shown. Statistical analysis was done using a one-tailed
674 t-test to determine whether TRA was higher than 0%: ns = not significant, ****=p<0.0001. *See also Figure S8, Table*
675 *S1, and S3-S4.*
676

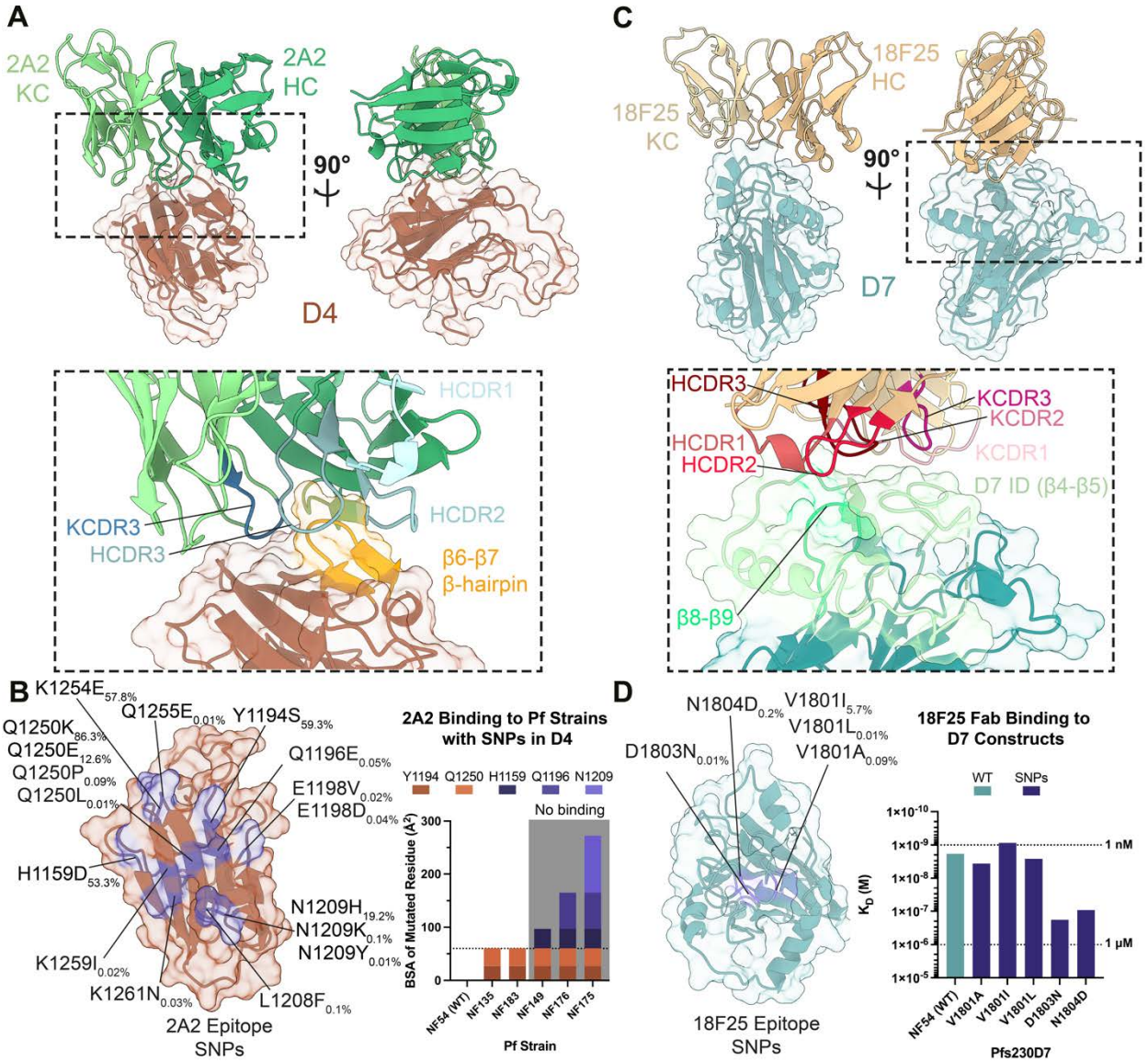

Figure 5: Structural delineation of potent Pfs230 epitopes outside of Pfs230D1. (A) The variable region of 2A2 (green) and Pfs230D4 (orange) are shown with key contacts (inset) made by the HCDR1, HCDR2, HCDR3, and KCDR3 (shades of blue) of mAb 2A2 with the β6-β7 perpendicular β-hairpin (yellow) of Pfs230D4 highlighted. **(B)** SNPs of Pfs230D4-2A2 epitope identified in the MalariaGEN Pf7 databse database (53) are indicated in purple and labeled. The frequency of the SNP is shown as a subscript. (right) Five strains of *P. falciparum* harbouring different combinations of five different SNPs (x-axis) with the BSA that that residue contributes to binding in the structural model (y-axis). Specific amino acid residue BSA contributions are indicated by shades of different colours. Residues found exclusively in *P. falciparum* strains that have perturbed ability to bind female gametes in surface immunofluorescence assays (asterisks) are coloured in shades of purple and appear above the dotted line. All other residues are coloured in shades of orange (**C)** The variable region of 18F25 (tan) and Pfs230D7 (cyan) are shown. 18F25 makes contacts with the Pfs230D7-ID (light green) and the β8-β9 loop (neon green) using all HCDRs (shades of red) and KCDRs (shades of pink) of 18F25 with Pfs230D7 (inset). **(D)** SNPs of Pfs230D7-18F25 epitope identified in the MalariaGEN Pf7 database (53) are indicated in purple and labeled. The frequency of the SNP is shown as a subscript. Summary of surface plasmon resonance experiments utilizing 18F25 Fab and Pfs230D7 variants (y-axis) (WT, teal; and SNP mutants, purple) and their determined affinity (y-axis). Dotted lines indicate K_D values of 1 nM and 1 μM. *See also Tables S3-4.*

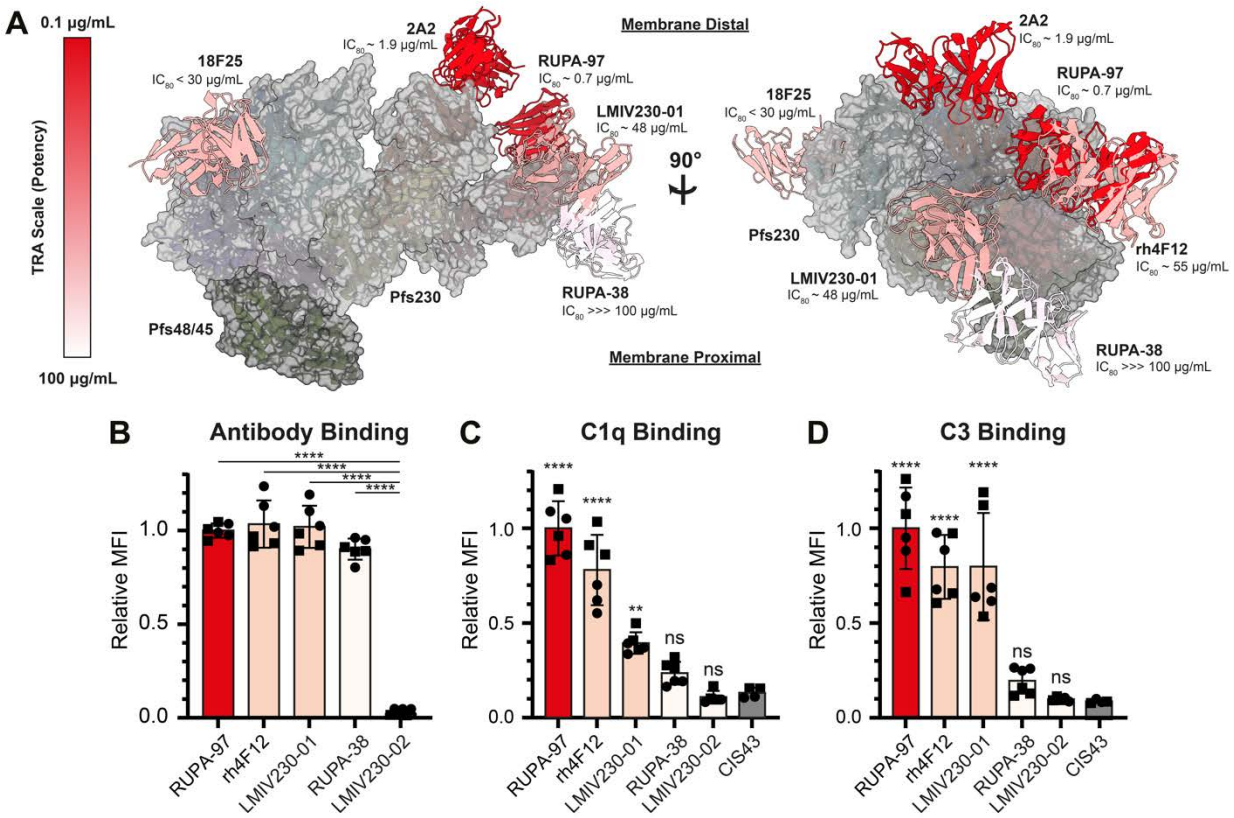

Figure 6: Molecular basis of Pfs230-directed mAb potency. (A) The binding sites of 18F25, LMIV230-01, 2A2, RUPA-97, RUPA-38, and rh4F12 shown in the context of Pfs230 (surface: gray, ribbons: domains coloured as done in Figure 1) and Pfs48/45 (surface: black, ribbons: domains coloured as done in Figure 1). The antibodies are coloured in accordance with their IC_{80} values or TRA via heat map with darker colours indicating higher TRA or potency (left scale). The membrane distal side corresponds to the top of the panel and the membrane proximal side at the bottom of the panel. **(B-D)** Anti-Pfs230D1 mAb binding (B), or antibody-mediated human C1q recruitment (C) and human C3 deposition (D) at 1 µg/ml on the surface of wildtype NF54 macrogametes as determined by flow cytometry. CIS43, an anti-PfCSP antibody, was included as a negative control for the C1q and C3 deposition assays. Mean fluorescence intensity (MFI) values were normalized against the mean of RUPA-97 replicates, to allow averaging across two independent experiments (depicted as different symbols) with two to three technical replicates each. Mean with standard deviations are shown. Statistical analysis was done using an ordinary one-way ANOVA with either a Tukey's multiple comparisons test with a single pooled variance comparing all groups to each other (panel B, only showing significant differences) or Dunnett's multiple comparisons test with a single pooled variance comparing all groups to CIS43 (C-D). ns = not significant; **=p<0.01, ****=p<0.0001. *See also Figure S9 and Table S1.*

710 # MAIN TABLES

711 **Table 1. CryoEM data collection and refinement statistics.**

	Pfs230D1-6:RUPA-97:LMIV230-01:2A2 (PDB: 9N5H, EMD-48921)	Pfs230D7-8:18F25 (PDB: 9N5O, EMD-48941)	Pfs230D9-14:Pfs48/45 (PDB: 9N5K, EMD-48924	Pfs230D13-14:Pfs48/45:RUPA-44:RUPA-71 (PDB: 9N5I, EMD-48922)
Data collection and processing				
Magnification	130,000	130,000	130,000	130,000
Voltage (kV)	300	300	300	300
Electron exposure (e–/Å^2)	50-53	50-53	50-53	50-53
Defocus range (µm)	0.4-3.5	0.1-3.0	0.4-3.5	0.4-3.5
Pixel size (Å)	0.93	1.03	0.93	0.93
Symmetry imposed	C_1	C_1	C_1	C_1
Initial particle images (no.)	1,167,622	237,721	1,942,561	1,942,561
Final particle images (no.)	70,113	165,992	138,915	146,814
Map resolution (Å) FSC threshold	3.6 0.143	3.8 0.143	4.7 0.143	3.4 0.143
Map resolution range (Å)	3.20-41.8	3.00-9.35	3.16-9.62	2.47-9.10
Refinement				
Initial model used (PDB code)	7USS, 7UVQ, 7JUM, 9N89	9N6U	7ZXF	7ZXF, 7UXL, 9N7K
Model resolution (Å) FSC threshold	 0.143	 0.143	 0.143	 0.143
Model resolution (Å)	3.7	3.9	5.1	3.4
Map sharpening *B* factor (Å^2)	-	-	-	-
Model composition Non-hydrogen atoms Protein residues Ligands	 19126 2430 0	 4313 546 0	 9496 1476 0	 9223 1156 2
B factors (Å^2) Protein Ligand	 108 -	 151 -	 556 -	 106 118
R.m.s. deviations Bond lengths (Å) Bond angles (°)	 0.002 0.58	 0.002 0.63	 0.002 0.53	 0.003 0.55
Validation MolProbity score Clashscore Poor rotamers (%)	 1.63 6.3 0.3	 1.67 5.2 0	 1.65 4.3 0.2	 2.03 10.3 1.3
Ramachandran plot Favored (%) Allowed (%) Disallowed (%)	 96.0 4.0 0	 94.2 5.8 0	 94.9 5.1 0	 94.0 6.0 0

712

713 # SUPPLEMENTARY FIGURES

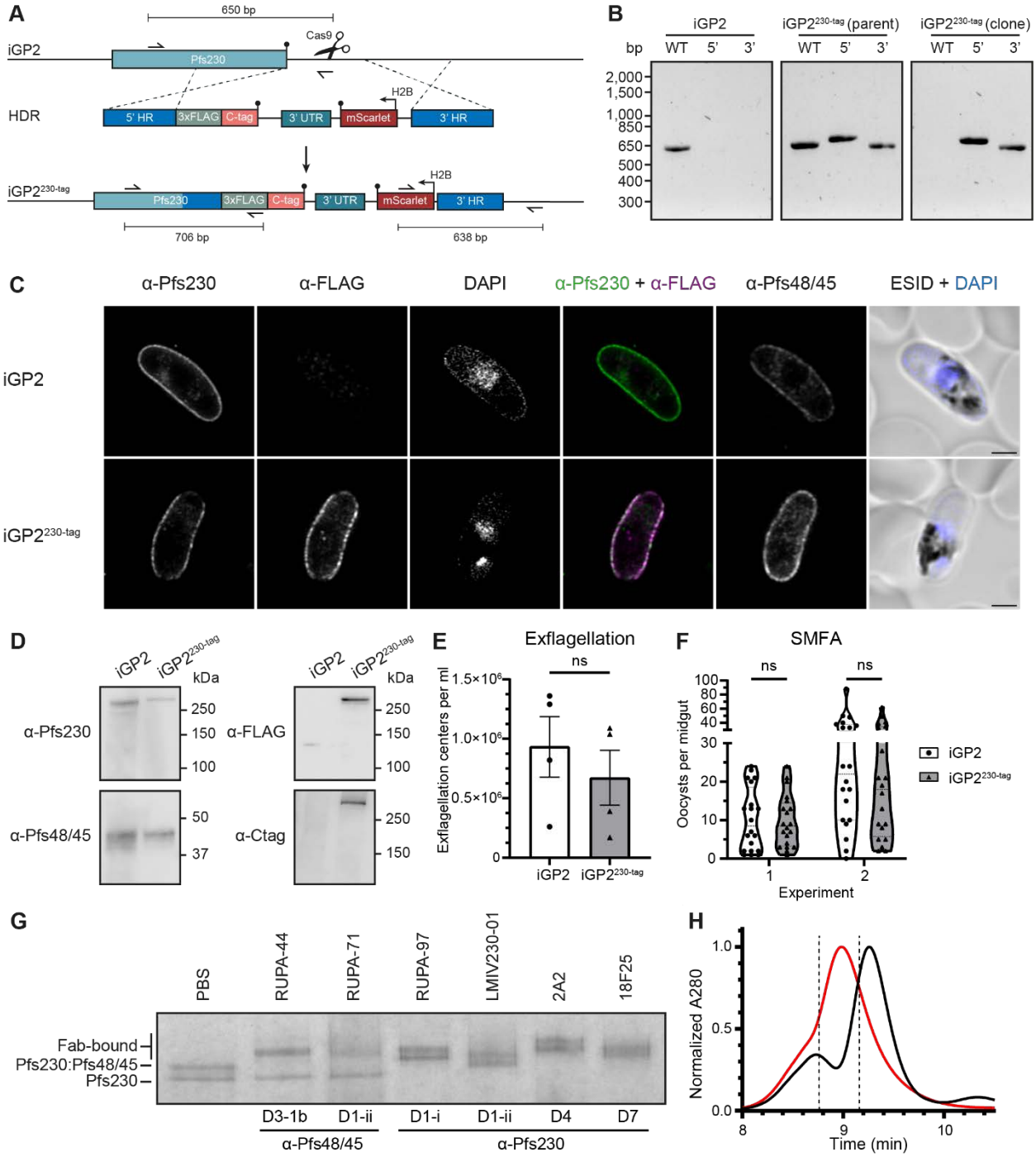

714
715
716 **Figure S1: The iGP2$^{230\text{-}tag}$ parasite line allows for purification of endogenous Pfs230:Pfs48/45 complex recognized**
717 **by transmission-blocking antibodies. (A)** Schematic overview of the genomic modification to obtain the iGP2$^{230\text{-}tag}$
718 parasite line. HDR = Homology Directed Repair, HR = homology region, 3xFLAG = triple FLAG tag, C-tag = EPEA* tag,
719 3'UTR = bidirectional 3'untranslated region of PBANKA_142660, H2B = promoter of Pf3D7_1105100. **(B)** Genomic
720 integration PCR to confirm 5' and 3' integration and the absence of wildtype parasites. Primers and expected PCR
721 product are indicated in (A). **(C)** Immunofluorescence microscopy images of paraformaldehyde/glutaraldehyde-fixed
722 and permeabilized iGP2 wildtype and iGP2$^{230\text{-}tag}$ stage V gametocytes. Parasites were stained for Pfs230 (green,

723 RUPA-55), FLAG-tag (magenta, M2), and Pfs48/45 (45.1), and DAPI (blue). Scalebar represents 5 µm. ESID =
724 Electronically Switchable Illumination and Detection brightfield image. **(D)** Western blot analysis of iGP2 and iGP2^{230-}
725 ^{tag} to confirm FLAG-tag and C-tag integration. **(E)** Exflagellation of stage V iGP2 (white) and iGP2$^{230-tag}$ (gray)
726 gametocytes. Bars represent mean ± standard deviation of number of exflagellation centers per ml from four
727 independent cultures (dots). No statistical significance was found using an unpaired t-test. **(F)** Transmission of iGP2
728 (white) and iGP2$^{230-tag}$ (gray) to mosquitoes in two independent standard membrane feeding experiments. Dots
729 represent the number of oocysts per midgut *Anopheles stephensi* mosquitoes (n=20 per experiment) in two
730 independent standard membrane feeding assays using iGP2 (white) and iGP2$^{230-tag}$ (gray) parasites. Statistical
731 analysis was done using a Mann-Whitney test with Holm-Šídák's multiple comparisons test (α = 0.05). ns = not
732 significant. **(G)** Coomassie blue stained Blue Native PAGE gel of purified Pfs230:Pfs48/45 (and free Pfs230) incubated
733 with molar excess of the following individual Fab fragments: RUPA-44, RUPA-71, RUP-97, LMIV230-01, 2A2, or 18F25.
734 Epitopes are defined in Figure 1A. **(H)** Normalized absorption at 280 nm during high-pressure liquid size-exclusion
735 chromatography of Pfs230:Pfs48/45 (black) or Pfs230-Pfs48/45:6Fab (red) complexes. Dotted lines indicate fractions
736 of eluted Pfs230:Pfs48/45:6Fab that were used for cryo-electron microscopy. *Related to Figure 1.*

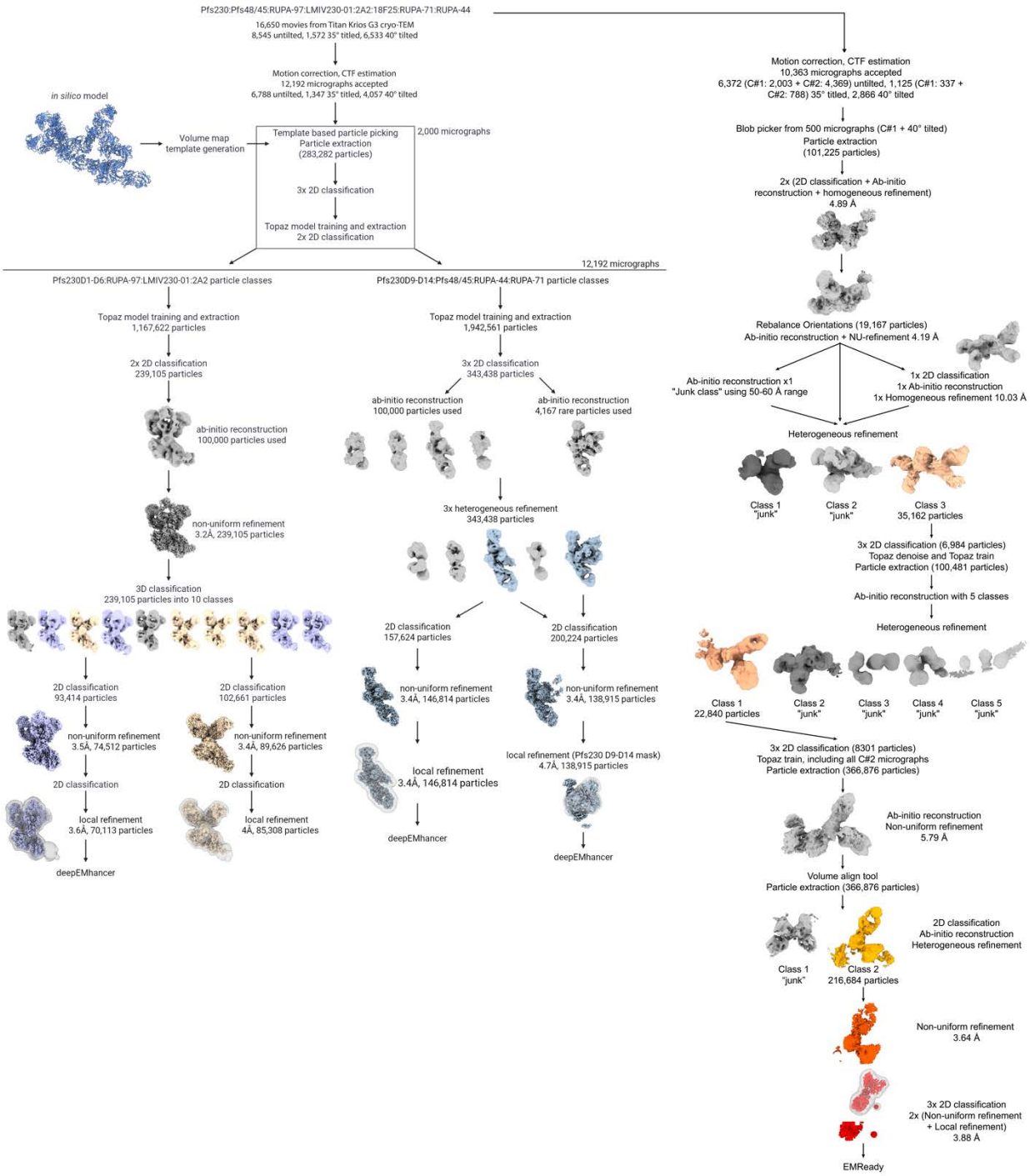

Figure S2: Cryo-EM processing workflow. Shown from left to right are the maps of Pfs230D1-6:LMIV230-01:RUPA-97:2A2, Pfs230D1-6:LMIV230-01:RUPA-97, Pfs230D13-14:Pfs48/45:RUPA-44:RUPA-71, the focused refinement for Pfs230D9-14:Pfs48/45, and the Pfs230D7-8:18F25 map. Abbreviations for the two data collection sessions are abbreviated in the Pfs230D7-8:18F25 workflow (C#1: collection C#2: collection 2). *Related to Figure 1.*

A

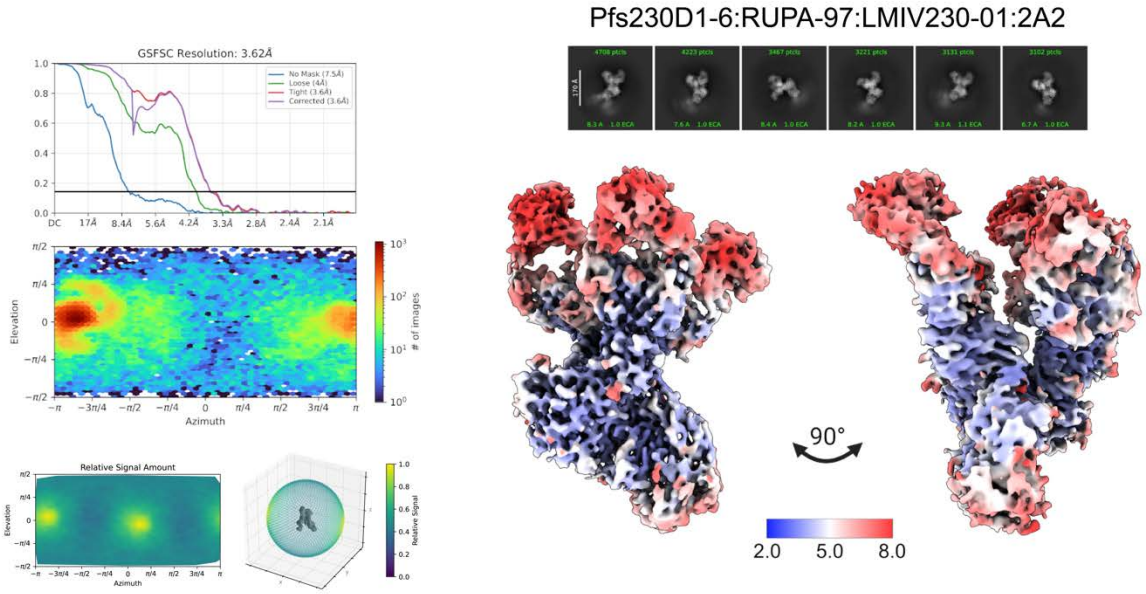
Pfs230D1-6:RUPA-97:LMIV230-01:2A2
GSFSC Resolution: 3.62Å
No Mask (7.5Å)
Loose (4Å)
Tight (3.6Å)
Corrected (3.6Å)
Elevation
Azimuth
# of images
Relative Signal Amount
Relative Signal
90°
2.0
5.0
8.0

B

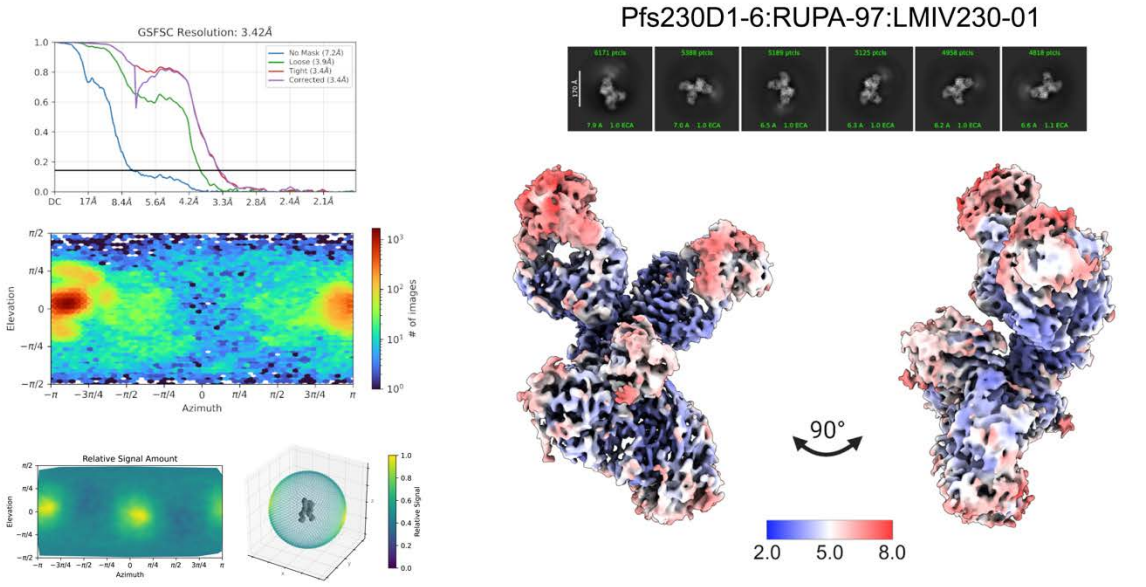
Pfs230D1-6:RUPA-97:LMIV230-01
GSFSC Resolution: 3.42Å
No Mask (7.2Å)
Loose (3.9Å)
Tight (3.4Å)
Corrected (3.4Å)
Elevation
Azimuth
# of images
Relative Signal Amount
Relative Signal
90°
2.0
5.0
8.0

744

C

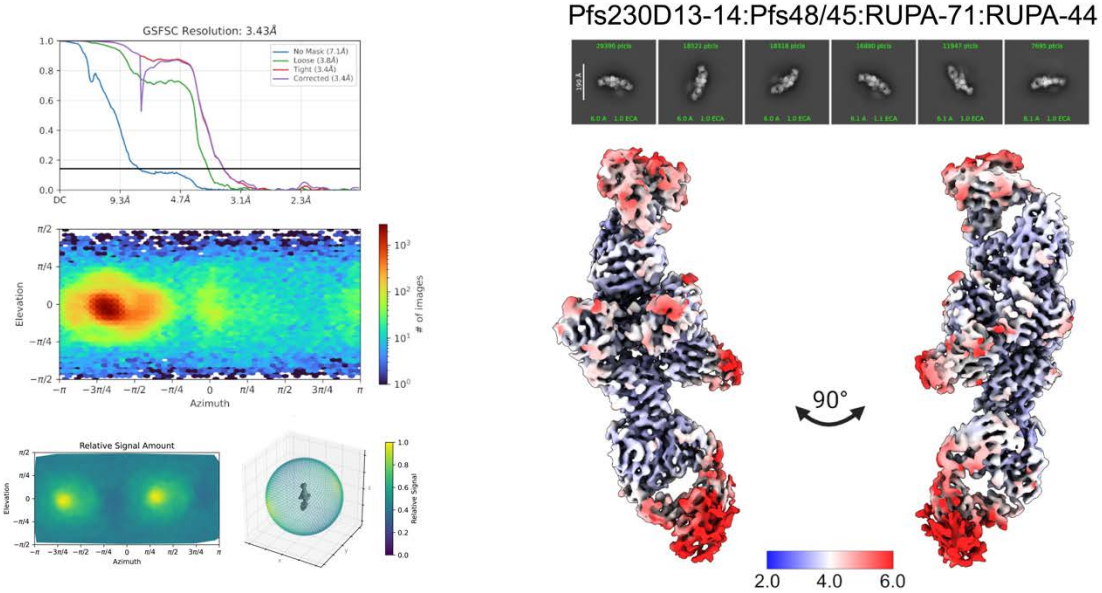
GSFSC Resolution: 3.43Å
No Mask (7.1Å)
Loose (3.8Å)
Tight (3.4Å)
Corrected (3.4Å)
DC
9.3Å
4.7Å
3.1Å
2.3Å
Elevation
Azimuth
# of images
Relative Signal Amount
Relative Signal
Pfs230D13-14:Pfs48/45:RUPA-71:RUPA-44
90°
2.0
4.0
6.0

D

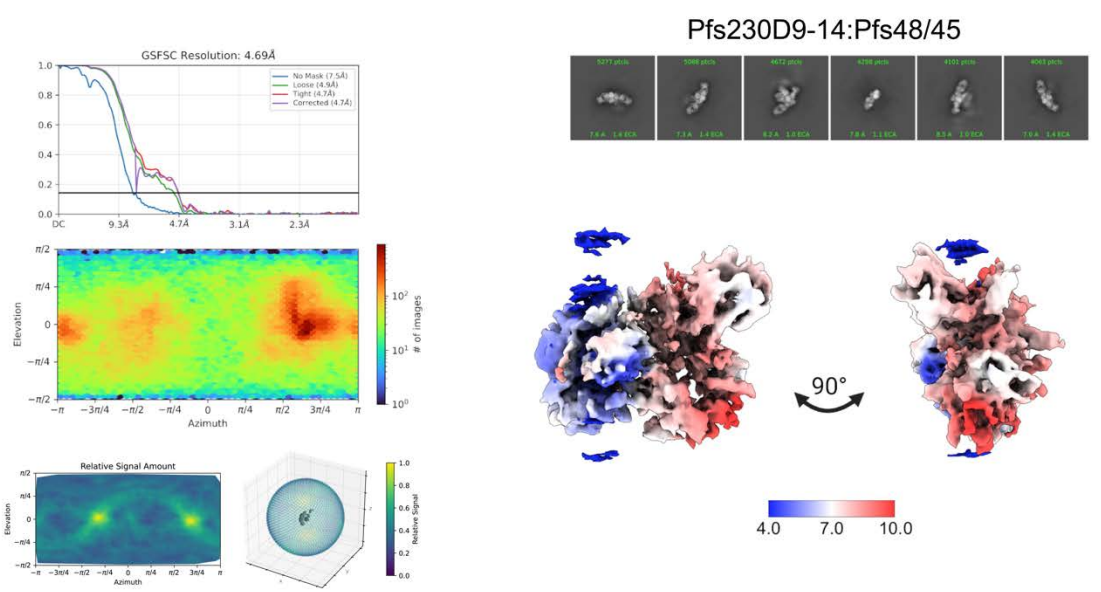
GSFSC Resolution: 4.69Å
No Mask (7.5Å)
Loose (4.9Å)
Tight (4.7Å)
Corrected (4.7Å)
DC
9.3Å
4.7Å
3.1Å
2.3Å
Elevation
Azimuth
# of images
Relative Signal Amount
Relative Signal
Pfs230D9-14:Pfs48/45
90°
4.0
7.0
10.0

745

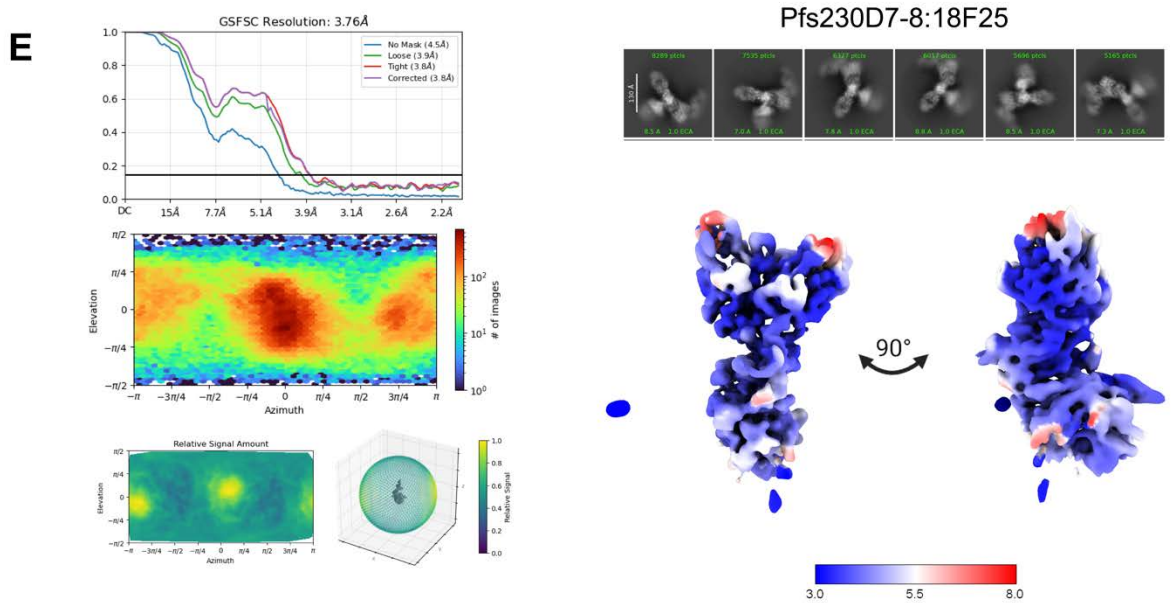

Figure S3: Cryo-EM map validation data. **(A-E)** The structures of (A) Pfs230D1-6:RUPA-97:LMIV230-01:2A2; (B) Pfs230D1-6:RUPA-97:LMIV230-01; (C) Pfs230D13-14:Pfs48/45:RUPA-44:RUPA-71; (D) focused refinement for Pfs230D9-14:Pfs48/45; and (E) Pfs230D7-8:18F25. The Fourier shell correlation curves following a gold-standard refinement with correction for the effects of masking for varying masks, the viewing direction particle distribution, and orientation diagnostic plots are shown (left panel). Additionally, representative 2D classes and cryo-EM maps coloured by local resolution are shown for each processed map (right panel). *Related to Figure 1.*

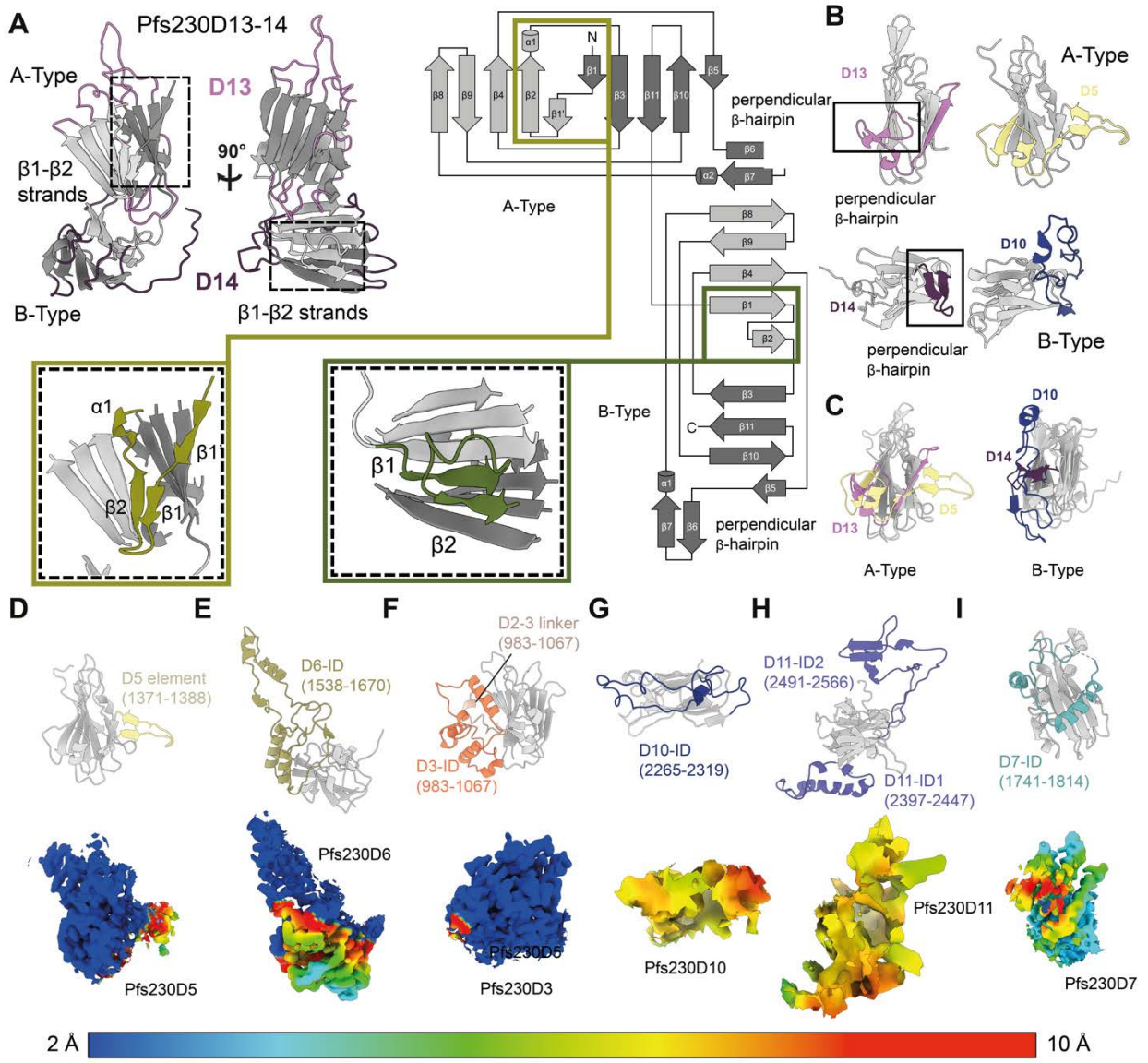

Figure S4: Structural features of Pfs230 6-Cys domains and Pfs230 domain clustering. (A) Pfs230D13-14 is shown as prototypical tandem A- and B-type 6-Cys domains of Pfs230. Loops of D13 and D14 are coloured according to the colouring scheme in Figure 1. The first β-sheet of the A-type and B-type domains is coloured distinctly (light gray) from the second β-sheet (gray). The distinguishing features of the A- and B-type domains (β1 to β2 strands) are indicated through the dashed box. Secondary structure topology of the two 6-Cys domains is shown with distinguishing features of A- (olive) and B-type (green) domains (β1 to β2 strands) indicated (inset) with a 3D representation of these differences shown. **(B-C)** Comparison of prototypical tandem 6-Cys domains (D13 and D14) to D5 and D10 respectively, (B) side by side and (C) overlaid, highlighting the structural differences of D5 and D10 at the perpendicular β-hairpin region. The regions that are structurally distinct are coloured according to the scheme in Figure 1. **(D-I)** Pfs230 domains that harbour IDs (Pfs230D3, D6, D7, D10, and D11) or structural elements contributing to ID clustering (Pfs230D3 and D5) are shown as ribbon representations with the cryoEM map corresponding to that portion of the model being shown underneath (shown at 5 Å radius around the models) and coloured according to local resolution (scale bar below). Non-canonical elements and IDs are coloured according to the colouring scheme specified in Figure 2. *Related to Figure 2.*

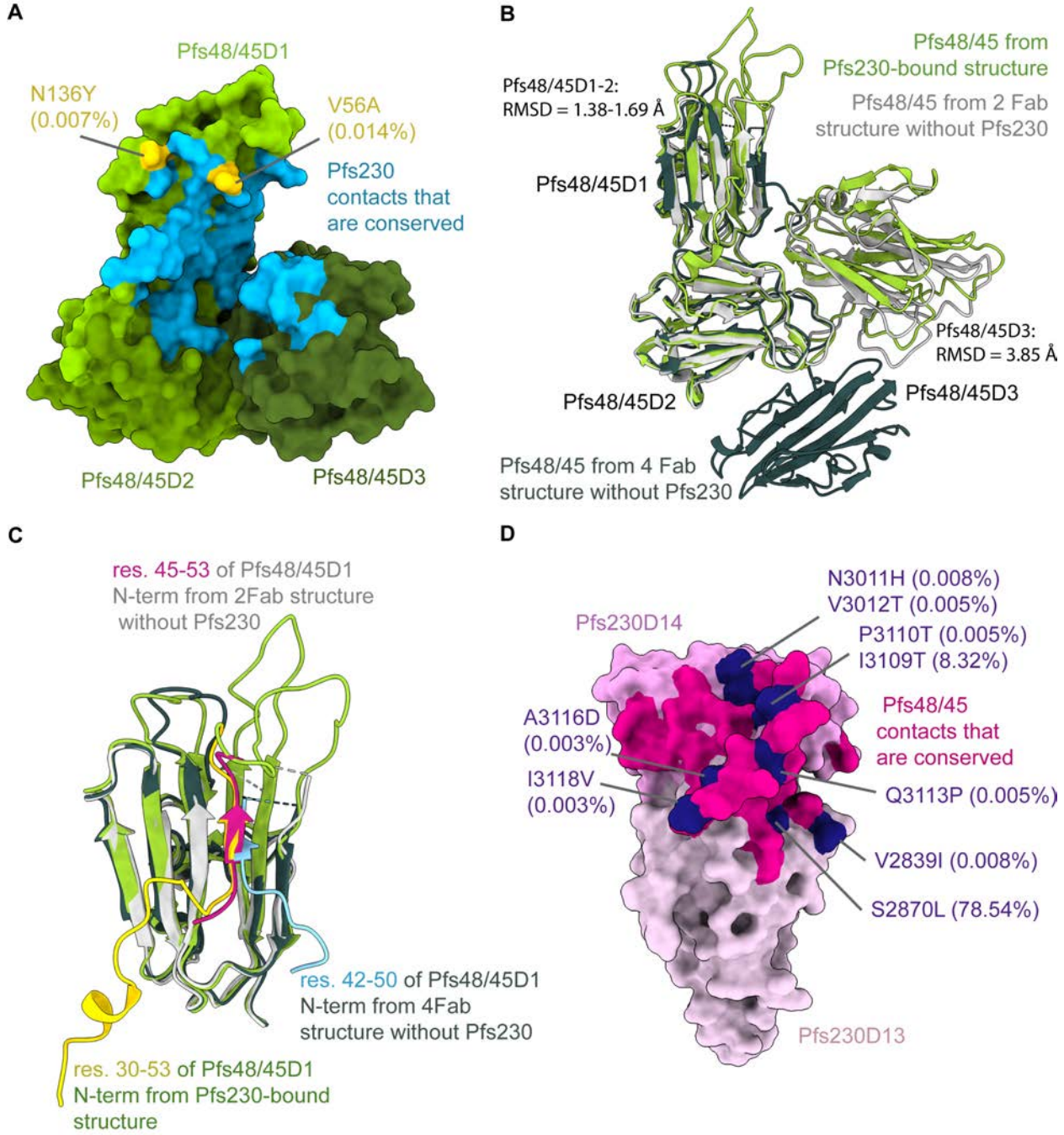

Figure S5: Comparison of Pfs48/45 conformation across determined structures and sequence conservation of Pfs230:Pfs48/45 binding site. (A) Structure of Pfs48/45 depicted as surface (yellow green, olive drab, and dark olive drab for Pfs48/45D1-3, respectively) with the Pfs230 binding site shown in sky blue and single nucleotide polymorphisms present within the epitope shown in gold. **(B)** Overlay of Pfs48/45 structures from Pfs48/45-Pfs230-6Fab complex (yellow green), Pfs48/45-4Fab complex (dark slate grey, PDB ID: 8U1P), and Pfs48/45-2 Fab complex (light grey, PDB ID: 7ZXF) aligned to Pfs48/45D1-2. **(C)** Overlay of N-terminal region of Pfs48/45-Pfs230-6Fab complex (green, yellow N-term), Pfs48/45-4Fab complex (dark slate grey, light blue N-term, PDB ID: 8U1P), and Pfs48/45-2 Fab complex (light grey, dark violet N-term, PDB ID: 7ZXF) aligned to Pfs48/45D1. **(D)** Pfs230D13 (thistle) and D14 (plum) shown as surface with the Pfs48/45 binding site in dark pink and SNPs in indigo. *Related to Figure 3.*

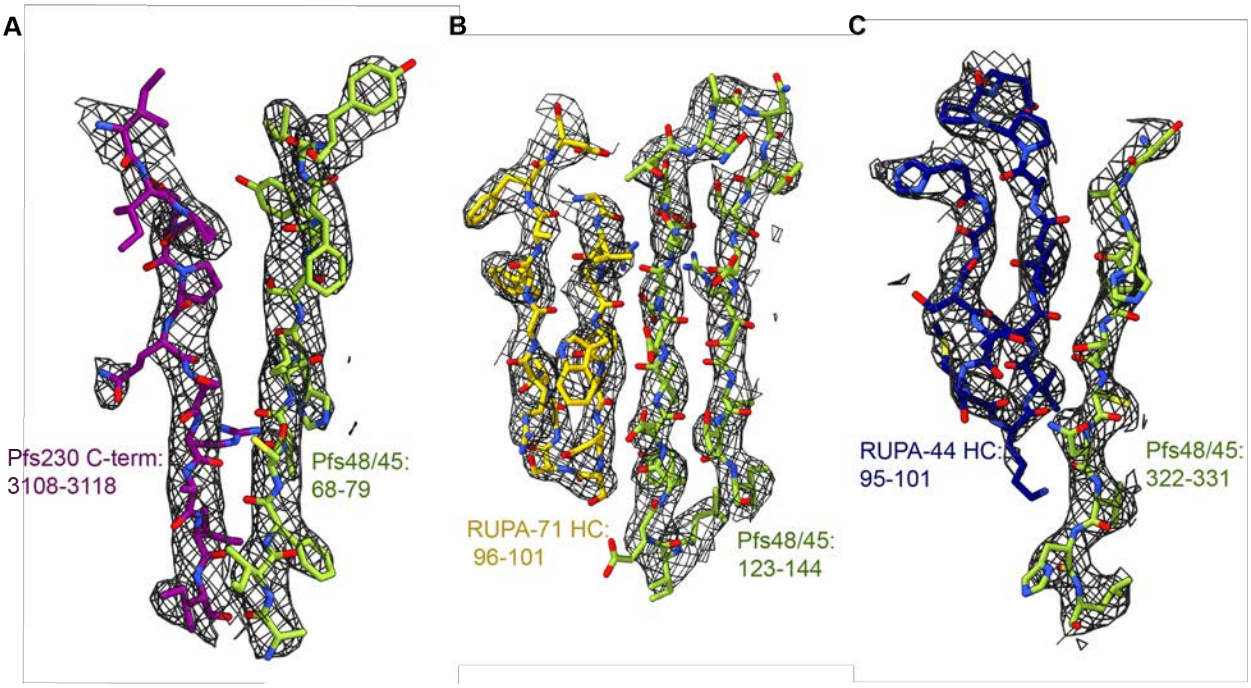

Figure S6: Cryo-EM map density around Pfs230:Pfs48/45:RUPA-71:RUPA-44 model. (A-D) Experimental map in grey mesh around key regions, including (A) the Pfs230 C-terminus and several of its Pfs48/45 contact residues, (B) residues at the Pfs48/45D1-RUPA-71 interface, and (C) residues at the Pfs48/45D3-RUPA-44 interface. Pfs48/45 (green), Pfs230D13-14 (purple), RUPA-71 (gold), and RUPA-44 (dark blue) are depicted as sticks. *Related to Figure 3-4.*

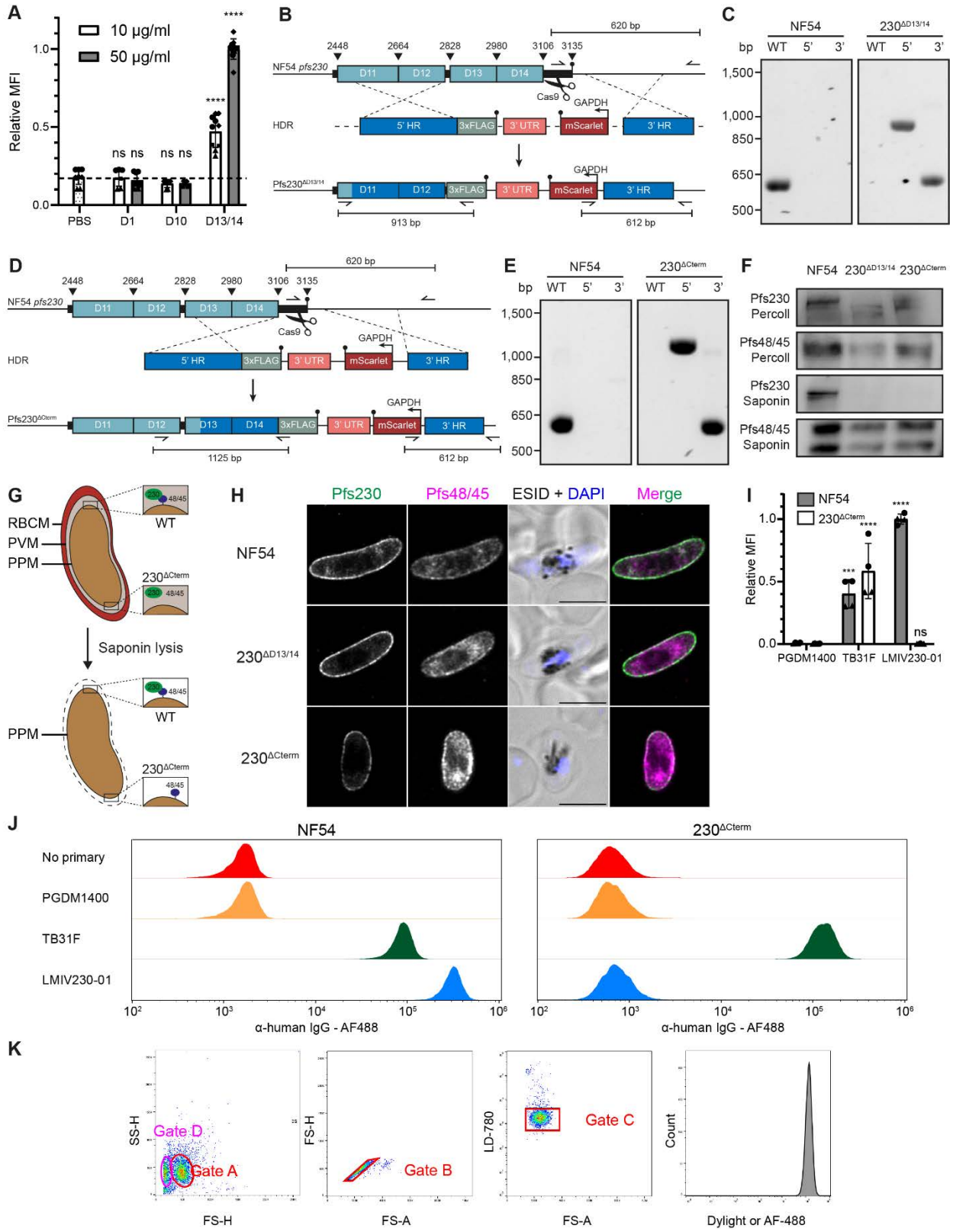

Figure S7: Pfs230:Pfs48/45 interactions are mediated by the C-terminal region Pfs230D13-14-Cterm *in vivo*. (A) Female gamete binding assay with recombinantly purified Pfs230D1, Pfs230D10 and Pfs230D13/14-Cterm at 10

794 µg/ml (white bar) or 50 µg/ml (gray bar). Bars show mean MFI (Mean Fluorescence Intensity) of two to four
795 independent experiments with two to three technical replicates each. Error bars show standard deviation. Individual
796 data points are shown, with different symbols for each independent experiment. Data was normalized against the
797 mean of the highest value (50 µg/ml D13-14) in each independent experiment to allow for comparison across
798 multiple experiments. Statistical analysis was done by comparing each group to the PBS control using an ordinary
799 one-way ANOVA with Dunnett's multiple comparisons test with a single pooled variance. **(B-E)** Schematic overview
800 of genomic integration of Pfs230$^{\Delta D13/14}$ (B) and Pfs230$^{\Delta Cterm}$ (D), and the corresponding diagnostic integration PCR (C,
801 E). HDR = Homology Directed Repair, HR = homology region, 3xFLAG = triple FLAG tag, 3'UTR = bidirectional
802 3'untranslated region of PBANKA_142660, GAPDH = promoter of Pf3D7_1462800. **(F)** Western blot analysis of
803 Pfs230 (18F25) and Pfs48/45 (32F3) expression in wildtype, Pfs230$^{\Delta D13/14}$ and Pfs230$^{\Delta Cterm}$ late-stage gametocytes,
804 isolated with Percoll (intact RBC and PVM membrane) or saponin (permeabilized RBC and PVM membrane). **(G)**
805 Schematic illustration of localization of the Pfs230:Pfs48/45 complex on the parasite plasma membrane (PPM), and
806 the effect of saponin on the red blood cell membrane (RBCM) and parasite vacuole membrane (PVM). **(H)**
807 Representative immunofluorescence microscopy images of paraformaldehyde/glutaraldehyde-fixed NF54 wildtype,
808 Pfs230$^{\Delta D13/14}$ and Pfs230$^{\Delta Cterm}$ stage V gametocytes. Parasites were stained for Pfs230 (green, RUPA-55), Pfs48/45
809 (magenta, 45.1), and DNA (DAPI, blue). Scale bar is 5 µm. ESID = Electronically Switchable Illumination and Detection
810 brightfield image. **(I)** Binding assay with wildtype (white bar) and Pfs230$^{\Delta Cterm}$ (gray bar) female gametes, testing the
811 binding of PDGM1400 (α-HIV-1 envelope glycoprotein), TB31F (α-Pfs48/45), and LMIV230-01 (α-Pfs230) antibodies
812 at 1 µg/ml. Bars show the mean relative MFI of two independent experiments with two technical replicates each
813 (±2000 live gametes per condition), error bars show standard deviation. MFI was normalized against the average of
814 LMIV230-01 in the independent experiments. MFI values were compared within each parasite line to the PGDM1400
815 control using an ordinary two-way ANOVA and Šídák's multiple comparison test with a single pooled variance. ns =
816 not significant; ***=p<0.001, ****=p<0.0001. **(J)** Representative histogram of female gamete binding assay as
817 shown in Figure S6I, comparing NF54 wildtype (top) and Pfs230$^{\Delta Cterm}$ (bottom) gametes. **(K)** Exemplary plots to
818 provide an overview for the gating strategy of macrogamete flow cytometry experiments. Live gametes (gate A)
819 were gated based on side-scatter (SS) and forward scatter (FS). Single cells (gate B) were selected based on FS area
820 (FS-A) versus height (FS-H), after which live cells (gate C) were selected based on absence of LD efluor780 staining.
821 The geometric mean fluorescence intensity of the Dylight/AlexaFluor-488 channel of the resulting population was
822 then used as the mean fluorescence intensity. Note that both gate A and D (containing dead gametes) were used in
823 the case of the complement deposition assays, when no live/dead stain was used. *Related to Figure 3.*
824

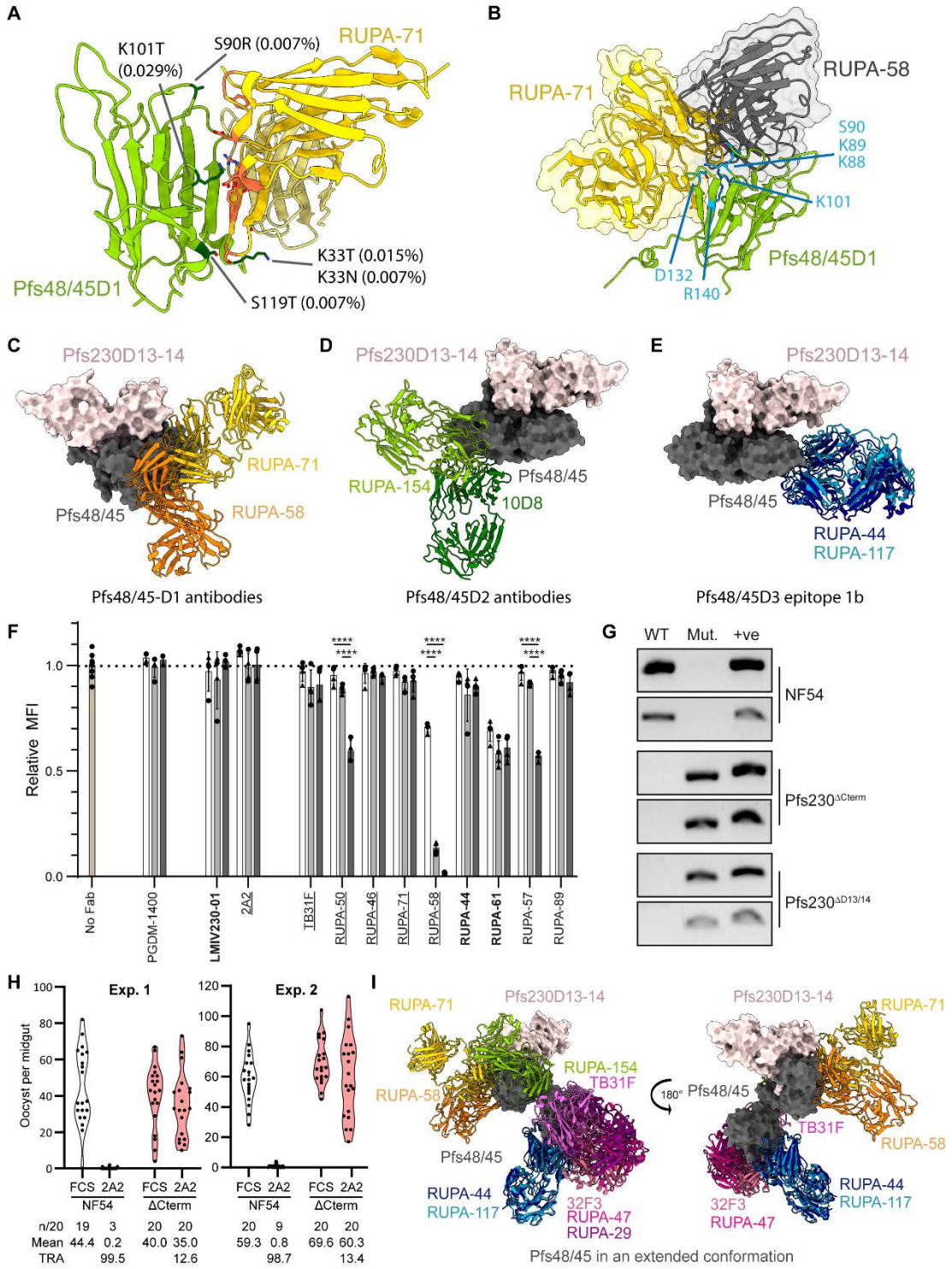

Figure S8: RUPA-71 epitope comparison and Pfs48/45-targeted Fab-induced dissociation of the Pfs230:Pfs48/45 complex *in vivo*. (A) RUPA-71 (yellow) bound to Pfs48/45 (yellow green) with Pfs48/45 residues with single nucleotide polymorphism in dark green and RUPA-71 residues that contact them in coral. **(B)** Overlay of Pfs48/45D1 (yellow green, cartoon) bound to antibodies RUPA-71 (gold) and RUPA-58 (dim gray; PDB ID: 8U1P). Pfs48/45 residues that contact both antibodies are indicated in blue. **(C-E)** Model of Pfs48/45 (dark gray, depicted in surface) bound to Pfs230D13-14 (misty rose, depicted in surface) in the disc-like conformation bound to (C) Pfs48/45D1 binders RUPA-71 (gold), RUPA-58 (orange, PDB ID: 8U1P)); (D) Pfs48/45D2 binders 10D8 (dark green, PDB ID: 7ZXF),

833 RUPA-154 (yellow green, PDB ID: 8U1P)); (E) Pfs48/45D3-1B binders (RUPA-44 (dark blue), RUPA-117 (sky blue, PDB
834 ID: 7UNB)). **(F)** Live female *P. falciparum* NF54 macrogametes were incubated with increasing concentrations of Fab
835 fragments (white bar: 1 µg/ml; light grey: 10 µg/ml; dark grey: 100 µg/ml), after which Pfs230 surface retention was
836 measured by determining the binding of 18F25-DyLight488 by flow cytometry. MFI was normalized against the no
837 Fab control to allow for averaging across experiments (two biological replicates with two technical replicates each).
838 Bars depict mean ± standard deviation, different symbols depict different biological replicates. Anti-Pfs48/45 Fabs
839 are sorted on potency as determined by the IC_{80} value (Underlined: IC_{80} < 10 µg/ml ; Bold: IC_{80} = 10-100 µg/ml,
840 Others: IC_{80} > 100 µg/ml, see **Table S**1). Statistical analysis to test for a dose-dependent reduction in 18F25-488
841 binding by comparing all concentrations per individual Fab using an ordinary two-way ANOVA with a Šídák's multiple
842 comparisons test with a single pooled variance as one family. Only significant comparisons are shown. **** =
843 p<0.0001. **(G)** PCR analysis of genomic DNA isolated from midgut oocysts from standard membrane feeding assay
844 experiments of Pfs230 wildtype and truncation parasite lines. Semi-nested PCRs were used to detect: WT = wildtype
845 Pfs230 genomic DNA; Mut = Pfs230 truncation genomic DNA; +ve = positive control for *P. falciparum* genomic DNA,
846 amplifying the Pfs25 gene (PF3D7_1031000). **(H)** Raw standard membrane feeding assay data of NF54 wildtype
847 (white) and $Pfs230^{\Delta Cterm}$ (pink) with and without the addition of 10 µg/ml 2A2 and active human complement. TRA
848 was calculated as percentage of reduction in mean oocyst per midgut compared to the FCS control. n/20 represents
849 the number of mosquitoes that had at least 1 oocyst, "mean" is the average number of oocyst per mosquito midgut.
850 **(I)** Model of Pfs48/45 (dark gray, depicted in surface) bound to Pfs230D13-14 (misty rose, depicted in surface) in the
851 extended conformation overlayed with RUPA-71 (gold), RUPA-58 (orange, PDB ID: 8U1P), , RUPA-154 (green, PDB
852 ID: 8U1P)), RUPA-44 (dark blue), RUPA-117 (sky blue, PDB ID: 7UNB), TB31F (orchid, PDB ID: 6E63), RUPA-29
853 (magenta, PDB ID: 7UXL), RUPA-47 (violet red, PDB ID: 7UNB), and 32F3 (pale violet red, PDB ID: 7ZWI)). *Related to*
854 *Figure 4.*
855

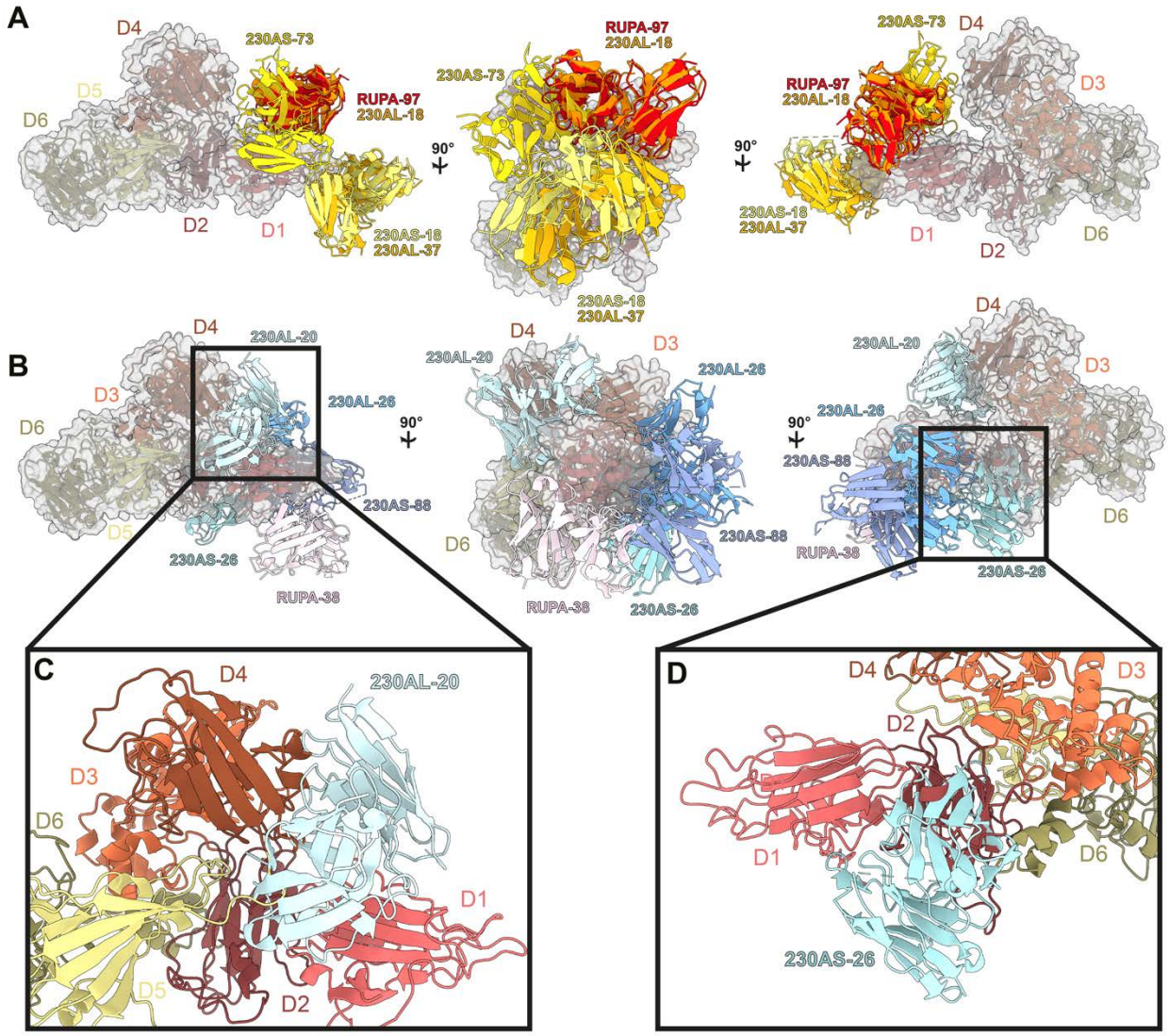

Figure S9. Overlay of Pfs230D1-EPA-elicted human mAbs (*17*). **(A)** Potent mAbs (TRA > 80% at 100 µg/mL in SMFA; shades of yellow and orange) are shown overlaid on Pfs230D1-6 (surface: gray, ribbons: coloured as done in Figure 1) compared to RUPA-97 (red). (**B-D**) Non-potent mAbs (TRA < 80% at 100 µg/mL in SMFA; shades of blue) are shown overlaid on Pfs230D1-6 compared to RUPA-38 (light pink) (B). Zoom in of (C) 230AL-20 and (D) 230AS-26 showcasing steric clashes that occur with Pfs230D4 and Pfs230D2, respectively – as examples of mAbs elicited via a single Pfs230 domain subunit vaccine exposing non-native epitopes that would be incompatible with full-length Pfs230 binding. *Related to Figure 6.*

865 # SUPPLEMENTARY TABLES

866 **Table S1. Overview of antibodies used or described in these studies.** Shown are the targeted epitopes, structures
867 in the RSCB/PDB database (structures in bold: this work), and estimates of the IC_{80} value (antibody concentration
868 required to achieve 80% TRA in Standard Membrane Feeding Assay). [a] Estimate value from limited number of
869 observations. [b] No blocking in High-Throughput membrane feeding assay at 100 µg/ml (32). *Related to Figures 1, 4,*
870 *and 6.*
871

Target	Antibody	Epitope	IC_{80} (µg/ml)	Reference	Structure
Pfs230	RUPA-97	D1 – i	0.7	Ivanochko[20]	7UVQ/**9N5H**
	4F12	D1 – i	55	MacDonald[34], Ivanochko[20]	6OHG
	LMIV230-01	D1 – ii	48	Coelho[19], Ivanochko[20]	7UFW/7JUM/**9N5H**
	RUPA-38	D1 – ii	>>100	Ivanochko[20]	7UVI
	LMIV230-02	D1 – iii	>>100	Coelho[19], Ivanochko[20]	7UVS
	15C5	D1 – iii	>>100	Lee[75], Ivanochko[20]	7UVQ
	2A2	D4	1.9	Roeffen[49] , De Jong[38]	**9N5H/9N89**
	18F25	D7	10 to 30 [a]	Roeffen[49], Inklaar[37]	**9N5O/9N6U**
Pfs48/45	RUPA-58	D1-i	7.5	Kucharska[15]	8U1P
	RUPA-94	D1-i	<100 [a]	Fabra-García[32]	-
	RUPA-46	D1-ii	2 to 10 [a]	Fabra-García[32]	-
	RUPA-71	D1-ii	2 to 10 [a]	Fabra-García[32]	**9N5I/9N7K**
	RUPA-154	D2	103.1	Kucharska[15]	8U1P
	RUPA-160	D2	± 10 [a]	Fabra-García[32]	-
	10D8	D2	>350 [a]	Ko[14]	7ZXF/7ZXG/7ZWM
	TB31F	D3 - 1a	0.86	Kundu[41], Kucharska[15], Ko[14]	6E63/7ZXF/6H5N
	RUPA-29	D3 - 1a	0.4 to 2 [a]	Fabra-García[32]	7UXL
	RUPA-50	D3 - 1a	0.4 to 2 [a]	Fabra-García[32]	-
	RUPA-47	D3 - 1a	10 to 100 [a]	Fabra-García[32]	7UNB
	RUPA-57	D3 - 1a	>100 [b]	Fabra-García[32]	-
	RUPA-72	D3 - 1a	>100 [b]	Fabra-García[32]	-
	RUPA-89	D3 - 1a	>100 [b]	Fabra-García[32]	-
	32F3	D3 - 1ab	<25 [a]	Vermeulen[25], Ko[14]	7ZWI/7ZWF/7ZWM
	RUPA-61	D3 - 1b	± 10 [a]	Fabra-García[32]	-
	RUPA-44	D3 - 1b	11	Fabra-García[32]; Kucharska[15]	7UXL/**9N5I**
	RUPA-117	D3 - 1b	± 10 [a]	Fabra-García[32]	7UNB
Negative controls	PGDM1400	HIV Env.	n/a	n/a	n/a
	CIS43	PfCSP	n/a	n/a	n/a

872

873 **Table S2: Pfs230:Pfs48/45 residue contact table.** *Related to Figure 3*

874

Pfs48/45 Domain	Pfs48/45 Residue	BSA (Å^2)	Pfs230 Residue contacts
Domain 1	N38	18	3108
	E40	25	3011, 3013
	I41	60	3011, 3112, 3013
	S42	88	2986, 2997, 2998, 3011,3012
	G43	34	2997
	F44	15	2997
	I45	86	2984, 3108-3110
	G46	16	3110
	Y47	65	3110-3114
	K48	49	2982, 2997, 3114
	N50	17	2993
	E54	48	2990, 2993, 3001
	G55	9	2993
	V56	90	2942, 2991, 2993, 2994
	H57	78	2942, 3116, 3118
	E65	34	2943, 3118
	R67	30	3118
	S68	20	3117-3118
	I69	25	3116-3118
	F70	56	3115-3117
	C71	25	3114-3116
	T72	50	3113-3115
	I73	16	3114
	H74	24	3115
	S75	8	3112
	D80	17	3110
	N136	39	3001
	Y137	18	2999
Domain 2	N247	13	3111
	K248	71	3109-3111
	I249	11	3108
	I250	17	3108
Domain 3	I348	28	2839
	I349	11	2839
	F354	48	2871, 2980
	Q355	25	2870
	I369	53	2868, 2870, 2977
	V370	9	2977
	Y371	11	2870, 2871, 2978-2980
	D373	47	2980, 3113
	N377	31	3115
	G379	25	3111, 3112
	D380	26	3111, 3112
	E385	12	3079

875

Table S3. Data collection and refinement statistics for the RUPA-71, 2A2, and 18F25 Fab crystal structures. *Related to Figures 4 and 5.*

	RUPA-71 Fab (PDB: 9N7K)	2A2 Fab (PDB: 9N89)	18F25 Fab (PDB: 9N6U)
Data collection			
Space group	P 2_1 2_1 2_1	P 2_1 2_1 2_1	P 2_1 2_1 2_1
Cell dimensions			
a, *b*, *c* (Å)	64.66, 74.55, 204.90	59.97, 76.68, 91.87	37.64, 81.80, 140.53
a, b, g (°)	90, 90, 90	90, 90, 90	90, 90, 90
Resolution (Å)[a]	48.85 - 2.28 (2.36 –2.28)	28.51 - 1.20 (1.21 -1.20)	34.19 - 1.60 (1.63 - 1.60)
R_{sym} or R_{merge}[b]	38.1 (214.6)	6.9 (58.3)	7.2 (62.2)
R_{pim}[c]	9.9 (56.2)	4.2 (35.6)	4.6 (40.2)
I / sI	7.5 (1.7)	8.9 (2.1)	9.8 (1.8)
Completeness (%)	100 (100)	99.5 (98.2)	99.4 (98.6)
Redundancy	15.4 (15.2)	3.5 (3.6)	3.3 (3.3)
Refinement			
Resolution (Å)	2.28	1.20	1.60
No. reflections	711,113 (67,539)	891,870 (29,484)	365,949 (17,109)
No. unique reflections	46,105 (4434)	254,175 (8,275)	109,994 (5,231)
R_{work}[d] / R_{free}[e]	19.1/ 24.1	18.6 / 19.4	18.8 / 21.3
No. atoms	7037	3708	4056
Protein	6776	3343	3432
Ligand/ion	52	0	20
Water	209	427	604
B-factors			
Protein	41	12	17
Ligand/ion	53[f]	0	36[g]
Water	39	20	26
R.m.s. deviations			
Bond lengths (Å)	0.009	0.004	0.006
Bond angles (°)	0.99	0.78	0.83

[a]Values in brackets refer to the highest resolution bin.

[b]$R_{merge} = \Sigma_{hkl} \Sigma_i \mid I_{hkl,\,i} - \langle I_{hkl} \rangle \mid / \Sigma_{hkl} \langle I_{hkl} \rangle$

[c]$R_{pim} = \Sigma_{hkl} [1/(N-1)]^{1/2} \Sigma i \mid I_{hkl,\,i} - \langle I_{hkl} \rangle \mid / \Sigma_{hkl} \langle I_{hkl} \rangle$

[d]$R_{work} = (\Sigma \mid \mid Fo \mid - \mid Fc \mid \mid) / (\Sigma \mid \mid F_o \mid)$ - for all data except R_{free} (see footnote e).

[e]5% of data were used for the R_{free} calculation.

[f]Four glycerol and seven 1,2-ethanediol molecules

[g]Four SO_4 ions

887 **Table S4: 2A2, 18F25, and RUPA-71 contact table in Kabat numbering.** *Related to Figures 4 and 5.*

Pfs230 Residue	Structural Element	BSA (Å²)	2A2 HC Residue	Structural Element	BSA (Å²)	2A2 KC Residue	Structural Element	BSA (Å²)
H1159	D4: β2-β3 loop	37	N33	HCDR1	16	S1	N-term / FR1-IMGT	27
E1160	D4: β3	14	N35	FR2-IMGT	2	I2	N-term / FR1-IMGT	8
Y1194	D4: β5	27	W47	FR2-IMGT	22	Q27	KCDR1	73
Q1196	D4: β5	68	N50	FR2-IMGT	19	S28	KCDR1	8
E1198	D4: β5-β6 loop	20	D52	HCDR2	21	N30	KCDR1	6
Y1205	D4: β6	34	H55	HCDR2	58	D91	KCDR3	8
K1206	D4: β6-β7 loop	51	G57	HCDR2	23	Y92	KCDR3	80
G1207	D4: β6-β7 loop	21	T58	HCDR2	11	S93	KCDR3	42
L1208	D4: β6-β7 loop	170	T59	FR3-IMGT	60	S94	KCDR3	74
N1209	D4: β6-β7 loop	107	Y60	FR3-IMGT	8	P95	KCDR3	12
S1210	D4: β7	54	N61	FR3-IMGT	1	L96	KCDR3	26
V1211	D4: β7	44	Q62	FR3-IMGT	51			
T1215	D4: α1	31	K65	FR3-IMGT	14			
Q1250	D4: β10	33	T100	HCDR3	1			
T1252	D4: β10	9	L101	HCDR3	20			
Q1255	D4: β10-β11 loop	4	Y102	HCDR3	70			
V1256	D4: β11	8	G103	HCDR3	17			
V1257	D4: β11	70	S105	HCDR3	32			
K1259	D4: β11	41						
K1261	D4: β11	15						
Pfs230 Residue	**Structural Element**	**BSA (Å²)**	**18F25 HC Residue**	**Structural Element**	**BSA (Å²)**	**18F25 KC Residue**	**Structural Element**	**BSA (Å²)**
K1751	D7: β4-β5 loop (D7-ID)	36	Y32	HCDR1	33	T30	KCDR1	16
V1752	D7: β4-β5 loop (D7-ID)	47	W33	HCDR1	10	N31	KCDR1	10
I1754	D7: β4-β5 loop (D7-ID)	27	Y52	HCDR2	23	D32	KCDR1	32
E1756	D7: β4-β5 loop (D7-ID)	35	D54	HCDR2	9	Y49	FR2-IMGT	24
V1801	D7: β4-β5 loop (D7-ID)	20	D56	HCDR2	12	S50	KCDR2	4
L1802	D7: β4-β5 loop (D7-ID)	79	R58	HCDR2	11	Y53	KCDR2	32
D1803	D7: β4-β5 loop (D7-ID)	52	R94	HCDR3	2	Y55	FR3-IMGT	7
N1804	D7: β4-β5 loop (D7-ID)	7	L96	HCDR3	27	H91	KCDR3	28
T1806	D7: β4-β5 loop (D7-ID)	32	Y97	HCDR3	42	Y92	KCDR3	85
F1807	D7: β4-β5 loop (D7-ID)	115	L98	HCDR3	70	S93	KCDR3	1
E1808	D7: β4-β5 loop (D7-ID)	40						
K1809	D7: β4-β5 loop (D7-ID)	2						
K1856	D7: β8-β9 loop	25						
D1857	D7: β8-β9 loop	1						
Pfs48/45 Residue	**Structural Element**	**BSA (Å²)**	**RUPA-71 HC Res.**	**Structural Element**	**BSA (Å²)**	**RUPA-71 KC Res.**	**Structural Element**	**BSA (Å²)**
K33	D1: N-term	28	E2	N-term / FR1-IMGT	47	K32	KCDR1	40
S35	D1: N-term	14	G26	HCDR1	19	L46	FR2-IMGT	20
S36	D1: N-term	11	F27	HCDR1	14	Y49	FR2-IMGT	57
K88	D1: β3-β4 loop	35	T28	HCDR1	26	T56	FR3-IMGT	79

K89	D1: β3-β4 loop	40	D31	HCDR1	24	S67	FR3-IMGT	39
S90	D1: β3-β4 loop	45	Y32	HCDR1	25			
K101	D1: β4-β5 loop	81	D52C	HCDR2	48			
Q104	D1: β4-β5 loop	61	E53	HCDR2	18			
S119	D1: α1	21	R94	HCDR3	14			
Y126	D1: α1-β7 loop	47	G96	HCDR3	24			
E127	D1: β7	42	L97	HCDR3	60			
I128	D1: β7	42	R98	HCDR3	86			
E129	D1: β7	61	W99	HCDR3	59			
E130	D1: β7	76	Y100	HCDR3	96			
N131	D1: β7	51	D100A	HCDR3	35			
D132	D1: β7-β8 loop	71	S100B	HCDR3	69			
T133	D1: β7-β8 loop	113	D101	HCDR3	30			
N134	D1: β7-β8 loop	24						
P135	D1: β7-β8 loop	26						
R140	D1: β8	6						

888

889 **Table S5: Oligonucleotides used in this study.** Red or green nucleotides depict restriction sites used for cloning.
890 Underlined nucleotides were used for overlap-PCR. Blue nucleotides highlight the CRISPR/Cas9 guide RNA sequence.
891 Orange nucleotides are three sequential guanosine nucleotides used for template switching, as described in (*85*).
892 *Related to Methods.*

	Function	Sequence
		HDR template - primers
p1	5'HR(-A) Pfs230-tag FW	cagttCGTCTCtggagCCACCATATGTACATAAAGATATACATTTCTCATTAG
p2	5'HR-A Pfs230-tag RV	aGCcCTactcTGAGGTTCTGGGATTATATAATTAGGATCAAATGTG
p3	5'HR Pfs230-tag RV	gtcaaCGTCTCataccAAGCTTTCTCAAGTATTTTG
p4	3'HR Pfs230-tag FW	cagttCGTCTCtgcacTCGTAAATAATTAATCAAACATATATATAATCAAAAGG
p5	3'HR Pfs230-tag RV	cagttCGTCTCtatggGGACTCTAAGATATTTCTTTCGCTAATCC
p6	H2B_mSc_biUTR-A FW	cagttGGTCTCTggagCGTCTCttaagCTAAATGGATGATTCCCCTCTTTGCAATATG
p7	H2B_mSc_biUTR-A RV	CAGTTggtctctTGACatttcatatttgcatgtgcatattaaaagtatcg
p8	H2B_mSc_biUTR-B FW	cagttggtctctGTCAgtctctgcataattttcgctatttaaatatat
p9	H2B_mSc_biUTR-B RV	cagttGGTCTCTatggCGTCTCtGTGCgTTCGAATCAACTCCGTTCAGTTAAAAATATTAC
p10	5'HR Pfs230ΔD13-14 FW	CAGTcgtctcTagagGGGATGATGTACATTTATTTTATCCTCCTC
p11	5'HR Pfs230ΔD13-14 RV	CAGTcgtctcTatccaccTGTTTTTTTTTCATCTATTTTTATTTTATCCATTGTAC
p12	5'HR Pfs230ΔCterm FW	CAGTcgtctcTagagCAATTGGTAAAGATATATGTAAATATGATGTTACTAC
p13	5'HR Pfs230ΔCterm RV	CAGTcgtctcTatccaccATTAGGATCAAATGTGATTCGTATAGTATAATTTG
p4	3'HR Pfs230Δ FW	See p4
p14	3'HR Pfs230Δ RV	cagtCGTCTCtcggtGGACTCTAAGATATTTCTTTCGCTAATCC
p15	GAPDH_swap FW	cagtGCTAGCGAAAAGAATTAAAAAGCCGAAGAAAAAATATATG
p16	GAPDH_swap RV	cagtGAGCTCGAGCTATGAAAAACATGGGTGTG
p17	C-terminal 3xFLAG FW	cagtGAATTcgtctcTggatCTGGTGATTACAAAGATCATGATGG
p18	C-terminal 3xFLAG RV	cagtAAGCTTcgtctcTcttaGTCATGATCCTTGTAATCTATATCGTG
		HDR template - oligonucleotides
p19	5'HR-B anneal Pfs230 FW	CTAATTATATAATCCCAGAACCTCAgagtAGgGCtATCATTAAATATGTAGATCTGCA AGATAAAAATTTTGCAAAATACTTGAGAAAGCTTggtaTGAGACGttgac
p20	5'HR-B anneal Pfs230 RV	gtcaaCGTCTCataccAAGCTTTCTCAAGTATTTTGCAAAATTTTTATCTTGCAGATCTA CATATTTAATGATaGCcCTactcTGAGGTTCTGGGATTATATAATTAG
p21	FLAG-C-tag FW	gatccgtctctGGTACATCTGGTGATTACAAAGATCATGATGGAGATTATAAAGATCAC GATATAGATTACAAGGATCATGACGGTTCAGGTGAACCAGAAGCATAAgtGAGACG
p22	FLAG-C-tag RV	aattCGTCTCacTTATGCTTCTGGTTCACCTGAACCGTCATGATCCTTGTAATCTATA TCGTGATCTTTATAATCTCCATCATGATCTTTGTAATCACCAGATGTACCagagacg
		CRISPR/Cas9 guide plasmid oligonucleotides
p23	Guide Pfs230 Cterm FW	tattgTTAATGATGGCTCTTGATTG
p24	Guide Pfs230 Cterm RV	aaacCAATCAAGAGCCATCATTAAc
p25	Guide Pfs230 D13 FW	tattgATTCTATTACATTATCAAGA
p26	Guide Pfs230 D13 RV	aaacTCTTGATAATGTAATAGAATc
		Template-switch oligonucleotide for hybridoma sequencing
p27	RT-PCR template switch FW	*AAGCAGTGGTATCAACGCAGAGTACATrGrGrG*
p28	RT-PCR for mIgK RV	TTGTCGTTCACTGCCATCAATC
p29	RT-PCR for mIgH RV	AGCTGGGAAGGTGTGCACAC
p30	Universal ISPCR primer FW	AAGCAGTGGTATCAACGCAGAG
p31	mIgK RV	ACATTGATGTCTTTGGGGTAGAAG
p32	mIgH RV	GGGATCCAGAGTTCCAGGTC

893

Integration PCR to check genomic integration		
p33	iGP2$^{230\text{-tag}}$ - WT FW	CTAATTATATAATCCCAGAACCTCAATCAAGAGCC
p34	iGP2$^{230\text{-tag}}$ - WT RV	GCAAAAATGAACAAACATCACACGAAGATGTG
p35	iGP2$^{230\text{-tag}}$ - 5'HR FW	GAACATATCTTACCAGGAGCCATTACAACAG
p36	iGP2$^{230\text{-tag}}$ - 5'HR RV	CTCCATCATGATCTTTGTAATCACCAGATG
p37	iGP2$^{230\text{-tag}}$ - 3'HR FW	GATGAACGATTTCTTAATATTGATAAGTATCATGTG
p34	iGP2$^{230\text{-tag}}$ - 3'HR RV	see p34
p38	230^{trunc} - WT FW	GAGCCATCATTAAATATGTAGATCTGCAAG
p34	230^{trunc} - WT RV	see p34
p39	230$^{\Delta\text{Cterm}}$ - 5'HR FW	CAGCTGATAAATATAATACATTTAGTAAAGAC
p40	230$^{\Delta\text{D13/14}}$ - 5'HR FW	CAAAGTTTTTATGGTGTTTCTCTTGATCATC
p41	230^{trunc} - 5'HR RV	CGTGATCTTTATAATCTCCATCATGATC
p42	230^{trunc} - 3'HR FW	CACACGATTTTAATTATCACACCCATG
p34	230^{trunc} - 3'HR RV	see p34
Integration PCR midgut oocyst		
p38	WT - reaction A - FW	see p38
p43	WT - reaction A - RV	CTTACGTATTCTCATTCTCATTGTGGAC
p38	WT - reaction B - FW	see p38
p34	WT - reaction B - RV	see p34
p42	Mut - reaction A - FW	see p42
p43	Mut - reaction A - RV	see p43
p42	Mut - reaction B - FW	see p42
p34	Mut - reaction B - RV	see p34
p44	Pfs25 - reaction A - FW	ATTTACATTATAAAAAAGCATACTGA
p45	Pfs25 - reaction A - RV	TTATTCTTTTAAAAATGAATAAACTTTAC
p46	Pfs25 - reaction B - FW	TGAAAATAGTATAAACATAATGCTTAG
p47	Pfs25 - reaction B - RV	ATGAATAAACTTTACAGTTTGTTTCT

894

895 **Table S6: Amino acid sequence of variable chains of mAbs 18F25 and 2A2.** *Related to Methods.*
896

mAb	Region	Amino acid sequence
18F25	Heavy chain (VDJ)	QVQLQQSGAELARPGASVKLSCKASGYTFTNYWMQWVKQRPGQGLEWFGAIYPGDGDTRYT QKFKGKATLTADKSSSTAYMQLSSLASEDSAVYYCARSLYLGAMDYWGQGTSVTVSS
	Light chain (VJ)	DIVMTQSHKFMSTSVGDRVSITCKASQDVTNDVAWYQQKPGQSPKLLIYSASYRYTGVPDRFTG SGSGTDFIFTISSVQAEDLAVYYCQQHYSAPPTFGGGTKLEIK
2A2	Heavy chain (VDJ)	EVQLQQSGPELEKPGASVKISCKASGYSITDYNMNWVKLSNGKSLEWIGNIDPSHGGTTYNQKF KGKATLTVDKSSSTAYMQLKSLTSEDSAVYHCARSTLYGNSAMDCWGQGTSVTVSS
	Light chain (VJ)	SIVMTQTPKFLLVPAGDRVTITCKASQSVNNDVTWYQQKPGQSPKLLIYYASNRYTGVPDRFTGS GYGTDFTFTISTVQAEDLAVYFCQQDYSSPLTFGAGTKLEL

897

REFERENCES

1. World malaria report 2024: addressing inequity in the global malaria response. Geneva: World Health Organization; 2024. Contract No.: CC BY-NC-SA 3.0 IGO.
2. Smith DL, McKenzie FE, Snow RW, Hay SI. Revisiting the basic reproductive number for malaria and its implications for malaria control. PLoS Biol. 2007;5(3):e42.
3. Cowman AF, Healer J, Marapana D, Marsh K. Malaria: Biology and Disease. Cell. 2016;167(3):610-24.
4. Aly AS, Vaughan AM, Kappe SH. Malaria parasite development in the mosquito and infection of the mammalian host. Annu Rev Microbiol. 2009;63:195-221.
5. Duffy PE. The Virtues and Vices of Pfs230: From Vaccine Concept to Vaccine Candidate. Am J Trop Med Hyg. 2022;107:17-21.
6. Sauerwein RW, Plieskatt J, Theisen M. 40 Years of Pfs48/45 Research as a Transmission-Blocking Vaccine Target of Plasmodium falciparum Malaria. Am J Trop Med Hyg. 2022;107:22-6.
7. Eksi S, Czesny B, van Gemert GJ, Sauerwein RW, Eling W, Williamson KC. Malaria transmission-blocking antigen, Pfs230, mediates human red blood cell binding to exflagellating male parasites and oocyst production. Mol Microbiol. 2006;61(4):991-8.
8. van Dijk MR, Janse CJ, Thompson J, Waters AP, Braks JA, Dodemont HJ, et al. A central role for P48/45 in malaria parasite male gamete fertility. Cell. 2001;104(1):153-64.
9. Rener J, Graves PM, Carter R, Williams JL, Burkot TR. Target antigens of transmission-blocking immunity on gametes of plasmodium falciparum. J Exp Med. 1983;158(3):976-81.
10. Kumar N. Target antigens of malaria transmission blocking immunity exist as a stable membrane bound complex. Parasite Immunol. 1987;9(3):321-35.
11. Quakyi IA, Carter R, Rener J, Kumar N, Good MF, Miller LH. The 230-kDa gamete surface protein of Plasmodium falciparum is also a target for transmission-blocking antibodies. J Immunol. 1987;139(12):4213-7.
12. Templeton TJ, Kaslow DC. Identification of additional members define a Plasmodium falciparum gene superfamily which includes Pfs48/45 and Pfs230. Mol Biochem Parasitol. 1999;101(1-2):223-7.
13. Gerloff DL, Creasey A, Maslau S, Carter R. Structural models for the protein family characterized by gamete surface protein Pfs230 of Plasmodium falciparum. Proc Natl Acad Sci U S A. 2005;102(38):13598-603.
14. Ko KT, Lennartz F, Mekhaiel D, Guloglu B, Marini A, Deuker DJ, et al. Structure of the malaria vaccine candidate Pfs48/45 and its recognition by transmission blocking antibodies. Nat Commun. 2022;13(1):5603.
15. Kucharska I, Ivanochko D, Hailemariam S, Inklaar MR, Kim HR, Teelen K, et al. Structural elucidation of full-length Pfs48/45 in complex with potent monoclonal antibodies isolated from a naturally exposed individual. Nat Struct Mol Biol. 2025.
16. Dietrich MH, Gabriela M, Reaksudsan K, Dixon MWA, Chan LJ, Adair A, et al. Nanobodies against Pfs230 block Plasmodium falciparum transmission. Biochem J. 2022;479(24):2529-46.
17. Tang WK, Coelho CH, Miura K, Nguemwo Tentokam BC, Salinas ND, Narum DL, et al. A human antibody epitope map of Pfs230D1 derived from analysis of individuals vaccinated with a malaria transmission-blocking vaccine. Immunity. 2023;56(2):433-43.e5.
18. Singh K, Burkhardt M, Nakuchima S, Herrera R, Muratova O, Gittis AG, et al. Structure and function of a malaria transmission blocking vaccine targeting Pfs230 and Pfs230-Pfs48/45 proteins. Commun Biol. 2020;3(1):395.
19. Coelho CH, Tang WK, Burkhardt M, Galson JD, Muratova O, Salinas ND, et al. A human monoclonal antibody blocks malaria transmission and defines a highly conserved neutralizing epitope on gametes. Nat Commun. 2021;12(1):1750.
20. Ivanochko D, Fabra-García A, Teelen K, van de Vegte-Bolmer M, van Gemert GJ, Newton J, et al. Potent transmission-blocking monoclonal antibodies from naturally exposed individuals target a conserved epitope on Plasmodium falciparum Pfs230. Immunity. 2023;56(2):420-32.e7.
21. Duffy PE. Transmission-Blocking Vaccines: Harnessing Herd Immunity for Malaria Elimination. Expert Rev Vaccines. 2021;20(2):185-98.
22. Tediosi F, Maire N, Penny M, Studer A, Smith TA. Simulation of the cost-effectiveness of malaria vaccines. Malar J. 2009;8:127.
23. Sherrard-Smith E, Sala KA, Betancourt M, Upton LM, Angrisano F, Morin MJ, et al. Synergy in anti-malarial pre-erythrocytic and transmission-blocking antibodies is achieved by reducing parasite density. Elife. 2018;7.

24. Challenger JD, Olivera Mesa D, Da DF, Yerbanga RS, Lefèvre T, Cohuet A, Churcher TS. Predicting the public health impact of a malaria transmission-blocking vaccine. Nat Commun. 2021;12(1):1494.
25. Vermeulen AN, Roeffen WF, Henderik JB, Ponnudurai T, Beckers PJ, Meuwissen JH. Plasmodium falciparum transmission blocking monoclonal antibodies recognize monovalently expressed epitopes. Dev Biol Stand. 1985;62:91-7.
26. Stone WJR, Campo JJ, Ouédraogo AL, Meerstein-Kessel L, Morlais I, Da D, et al. Unravelling the immune signature of Plasmodium falciparum transmission-reducing immunity. Nat Commun. 2018;9(1):558.
27. van der Kolk M, de Vlas SJ, Sauerwein RW. Reduction and enhancement of Plasmodium falciparum transmission by endemic human sera. Int J Parasitol. 2006;36(10-11):1091-5.
28. Bousema T, Roeffen W, Meijerink H, Mwerinde H, Mwakalinga S, van Gemert GJ, et al. The dynamics of naturally acquired immune responses to Plasmodium falciparum sexual stage antigens Pfs230 & Pfs48/45 in a low endemic area in Tanzania. PLoS One. 2010;5(11):e14114.
29. Graves PM, Carter R, Burkot TR, Quakyi IA, Kumar N. Antibodies to Plasmodium falciparum gamete surface antigens in Papua New Guinea sera. Parasite Immunol. 1988;10(2):209-18.
30. Mulder B, Lensen T, Tchuinkam T, Roeffen W, Verhave JP, Boudin C, Sauerwein R. Plasmodium falciparum: membrane feeding assays and competition ELISAs for the measurement of transmission reduction in sera from Cameroon. Exp Parasitol. 1999;92(1):81-6.
31. Roeffen W, Mulder B, Teelen K, Bolmer M, Eling W, Targett GA, et al. Association between anti-Pfs48/45 reactivity and P. falciparum transmission-blocking activity in sera from Cameroon. Parasite Immunol. 1996;18(2):103-9.
32. Fabra-García A, Hailemariam S, de Jong RM, Janssen K, Teelen K, van de Vegte-Bolmer M, et al. Highly potent, naturally acquired human monoclonal antibodies against Pfs48/45 block Plasmodium falciparum transmission to mosquitoes. Immunity. 2023;56(2):406-19.e7.
33. Lennartz F, Brod F, Dabbs R, Miura K, Mekhaiel D, Marini A, et al. Structural basis for recognition of the malaria vaccine candidate Pfs48/45 by a transmission blocking antibody. Nat Commun. 2018;9(1):3822.
34. MacDonald NJ, Nguyen V, Shimp R, Reiter K, Herrera R, Burkhardt M, et al. Structural and Immunological Characterization of Recombinant 6-Cysteine Domains of the Plasmodium falciparum Sexual Stage Protein Pfs230. J Biol Chem. 2016;291(38):19913-22.
35. Tachibana M, Miura K, Takashima E, Morita M, Nagaoka H, Zhou L, et al. Identification of domains within Pfs230 that elicit transmission blocking antibody responses. Vaccine. 2019;37(13):1799-806.
36. Inklaar MR, de Jong RM, Da DF, Hubregtse LL, Meijer M, Teelen K, et al. Pfs230 Domain 12 is a potent malaria transmission-blocking vaccine candidate. bioRxiv. 2024 (preprint):2024.11.09.622785.
37. Inklaar MR, de Jong RM, Bekkering ET, Nagaoka H, Fennemann FL, Teelen K, et al. Pfs230 Domain 7 is targeted by a potent malaria transmission-blocking monoclonal antibody. NPJ Vaccines. 2023;8(1):186.
38. de Jong RM, Meerstein-Kessel L, Da DF, Nsango S, Challenger JD, van de Vegte-Bolmer M, et al. Monoclonal antibodies block transmission of genetically diverse Plasmodium falciparum strains to mosquitoes. NPJ Vaccines. 2021;6(1):101.
39. Simons LM, Ferrer P, Gombakomba N, Underwood K, Herrera R, Narum DL, et al. Extending the range of Plasmodium falciparum transmission blocking antibodies. Vaccine. 2023;41(21):3367-79.
40. Roeffen W, Geeraedts F, Eling W, Beckers P, Wizel B, Kumar N, et al. Transmission blockade of Plasmodium falciparum malaria by anti-Pfs230-specific antibodies is isotype dependent. Infect Immun. 1995;63(2):467-71.
41. Kundu P, Semesi A, Jore MM, Morin MJ, Price VL, Liang A, et al. Structural delineation of potent transmission-blocking epitope I on malaria antigen Pfs48/45. Nat Commun. 2018;9(1):4458.
42. Miura K, Flores-Garcia Y, Long CA, Zavala F. Vaccines and monoclonal antibodies: new tools for malaria control. Clin Microbiol Rev. 2024;37(2):e0007123.
43. Yoo R, Jore MM, Julien JP. Targeting Bottlenecks in Malaria Transmission: Antibody-Epitope Descriptions Guide the Design of Next-Generation Biomedical Interventions. Immunol Rev. 2025;330(1):e70001.
44. Plieskatt J, Ofori EA, Naghizadeh M, Miura K, Flores-Garcia Y, Borbye-Lorenzen N, et al. ProC6C, a novel multi-stage malaria vaccine, elicits functional antibodies against the minor and central repeats of the Circumsporozoite Protein in human adults. Front Immunol. 2024;15:1481829.
45. Tiono AB, Plieskatt JL, Ouedraogo A, Soulama BI, Miura K, Bougouma EC, et al. A randomized first-in-human phase I trial of differentially adjuvanted Pfs48/45 malaria vaccines in Burkinabé adults. J Clin Invest. 2024;134(7):e175707.

1002 46. Healy SA, Anderson C, Swihart BJ, Mwakingwe A, Gabriel EE, Decederfelt H, et al. Pfs230 yields higher
1003 malaria transmission-blocking vaccine activity than Pfs25 in humans but not mice. J Clin Invest. 2021;131(7):e146221.
1004 47. Sagara I, Healy SA, Assadou MH, Kone M, Swihart BJ, Kwan JL, et al. Malaria transmission-blocking vaccines
1005 Pfs230D1-EPA and Pfs25-EPA in Alhydrogel in healthy Malian adults; a phase 1, randomised, controlled trial. Lancet
1006 Infect Dis. 2023;23(11):1266-79.
1007 48. Boltryk SD, Passecker A, Alder A, Carrington E, van de Vegte-Bolmer M, van Gemert GJ, et al. CRISPR/Cas9-
1008 engineered inducible gametocyte producer lines as a valuable tool for Plasmodium falciparum malaria transmission
1009 research. Nat Commun. 2021;12(1):4806.
1010 49. Roeffen W, Beckers PJ, Teelen K, Lensen T, Sauerwein RW, Meuwissen JH, Eling W. Plasmodium falciparum:
1011 a comparison of the activity of Pfs230-specific antibodies in an assay of transmission-blocking immunity and specific
1012 competition ELISAs. Exp Parasitol. 1995;80(1):15-26.
1013 50. Dietrich MH, Chan LJ, Adair A, Boulet C, O'Neill MT, Tan LL, et al. Structure of the Pf12 and Pf41 heterodimeric
1014 complex of Plasmodium falciparum 6-cysteine proteins. FEMS Microbes. 2022;3:xtac005.
1015 51. Parker ML, Peng F, Boulanger MJ. The Structure of Plasmodium falciparum Blood-Stage 6-Cys Protein Pf41
1016 Reveals an Unexpected Intra-Domain Insertion Required for Pf12 Coordination. PLoS One. 2015;10(9):e0139407.
1017 52. Churcher TS, Blagborough AM, Delves M, Ramakrishnan C, Kapulu MC, Williams AR, et al. Measuring the
1018 blockade of malaria transmission--an analysis of the Standard Membrane Feeding Assay. Int J Parasitol.
1019 2012;42(11):1037-44.
1020 53. Abdel Hamid MM, Abdelraheem MH, Acheampong DO, Ahouidi A, Ali M, Almagro-Garcia J, et al. Pf7: an
1021 open dataset of Plasmodium falciparum genome variation in 20,000 worldwide samples. Wellcome Open Res.
1022 2023;8:22.
1023 54. Kanoi BN, Nagaoka H, Morita M, Tsuboi T, Takashima E. Leveraging the wheat germ cell-free protein synthesis
1024 system to accelerate malaria vaccine development. Parasitol Int. 2021;80:102224.
1025 55. Diebolder CA, Beurskens FJ, de Jong RN, Koning RI, Strumane K, Lindorfer MA, et al. Complement is activated
1026 by IgG hexamers assembled at the cell surface. Science. 2014;343(6176):1260-3.
1027 56. Strasser J, de Jong RN, Beurskens FJ, Wang G, Heck AJR, Schuurman J, et al. Unraveling the Macromolecular
1028 Pathways of IgG Oligomerization and Complement Activation on Antigenic Surfaces. Nano Lett. 2019;19(7):4787-96.
1029 57. Ho CM, Beck JR, Lai M, Cui Y, Goldberg DE, Egea PF, Zhou ZH. Malaria parasite translocon structure and
1030 mechanism of effector export. Nature. 2018;561(7721):70-5.
1031 58. Ho CM, Jih J, Lai M, Li X, Goldberg DE, Beck JR, Zhou ZH. Native structure of the RhopH complex, a key
1032 determinant of malaria parasite nutrient acquisition. Proc Natl Acad Sci U S A. 2021;118(35):e2100514118.
1033 59. Schureck MA, Darling JE, Merk A, Shao J, Daggupati G, Srinivasan P, et al. Malaria parasites use a soluble
1034 RhopH complex for erythrocyte invasion and an integral form for nutrient uptake. Elife. 2021;10.
1035 60. Zhao J, Makhija S, Zhou C, Zhang H, Wang Y, Muralidharan M, et al. Structural insights into the human PA28-
1036 20S proteasome enabled by efficient tagging and purification of endogenous proteins. Proc Natl Acad Sci U S A.
1037 2022;119(33):e2207200119.
1038 61. Di Trani JM, Gheorghita AA, Turner M, Brzezinski P, Ädelroth P, Vahidi S, et al. Structure of the bc(1)-cbb(3)
1039 respiratory supercomplex from Pseudomonas aeruginosa. Proc Natl Acad Sci U S A. 2023;120(40):e2307093120.
1040 62. Liang Y, Plourde A, Bueler SA, Liu J, Brzezinski P, Vahidi S, Rubinstein JL. Structure of mycobacterial respiratory
1041 complex I. Proc Natl Acad Sci U S A. 2023;120(13):e2214949120.
1042 63. Ho CM, Li X, Lai M, Terwilliger TC, Beck JR, Wohlschlegel J, et al. Bottom-up structural proteomics: cryoEM
1043 of protein complexes enriched from the cellular milieu. Nat Methods. 2020;17(1):79-85.
1044 64. Abramson J, Adler J, Dunger J, Evans R, Green T, Pritzel A, et al. Accurate structure prediction of biomolecular
1045 interactions with AlphaFold 3. Nature. 2024;630(8016):493-500.
1046 65. van Dijk MR, van Schaijk BC, Khan SM, van Dooren MW, Ramesar J, Kaczanowski S, et al. Three members of
1047 the 6-cys protein family of Plasmodium play a role in gamete fertility. PLoS Pathog. 2010;6(4):e1000853.
1048 66. Sanders RW, Moore JP. Virus vaccines: proteins prefer prolines. Cell Host Microbe. 2021;29(3):327-33.
1049 67. Crank MC, Ruckwardt TJ, Chen M, Morabito KM, Phung E, Costner PJ, et al. A proof of concept for structure-
1050 based vaccine design targeting RSV in humans. Science. 2019;365(6452):505-9.
1051 68. McLeod B, Mabrouk MT, Miura K, Ravichandran R, Kephart S, Hailemariam S, et al. Vaccination with a
1052 structure-based stabilized version of malarial antigen Pfs48/45 elicits ultra-potent transmission-blocking antibody
1053 responses. Immunity. 2022;55(9):1680-92.e8.

69. Dickey TH, Gupta R, McAleese H, Ouahes T, Orr-Gonzalez S, Ma R, et al. Design of a stabilized non-glycosylated Pfs48/45 antigen enables a potent malaria transmission-blocking nanoparticle vaccine. NPJ Vaccines. 2023;8(1):20.
70. Correia BE, Bates JT, Loomis RJ, Baneyx G, Carrico C, Jardine JG, et al. Proof of principle for epitope-focused vaccine design. Nature. 2014;507(7491):201-6.
71. Bale JB, Gonen S, Liu Y, Sheffler W, Ellis D, Thomas C, et al. Accurate design of megadalton-scale two-component icosahedral protein complexes. Science. 2016;353(6297):389-94.
72. Dietrich MH, Chmielewski J, Chan L-J, Tan LL, Adair A, Lyons FMT, et al. Cryo-EM structure of endogenous *Plasmodium falciparum* Pfs230 and Pfs48/45 fertilization complex. bioRxiv. 2025:2025.02.13.638205.
73. Brooks SR, Williamson KC. Proteolysis of Plasmodium falciparum surface antigen, Pfs230, during gametogenesis. Mol Biochem Parasitol. 2000;106(1):77-82.
74. Deutsch EW, Bandeira N, Perez-Riverol Y, Sharma V, Carver JJ, Mendoza L, et al. The ProteomeXchange consortium at 10 years: 2023 update. Nucleic Acids Res. 2023;51(D1):D1539-d48.
75. Lee SM, Plieskatt J, Krishnan S, Raina M, Harishchandra R, King CR. Expression and purification optimization of an N-terminal Pfs230 transmission-blocking vaccine candidate. Protein Expr Purif. 2019;160:56-65.
76. Lim MY, LaMonte G, Lee MCS, Reimer C, Tan BH, Corey V, et al. UDP-galactose and acetyl-CoA transporters as Plasmodium multidrug resistance genes. Nat Microbiol. 2016;1:16166.
77. Verhoef JMJ, Bekkering ET, Boshoven C, Hannon M, Proellochs NI, Spruijt CG, Kooij TWA. The role of stomatin-like protein (STOML) in Plasmodium falciparum. bioRxiv. 2024:2024.07.18.604071.
78. Trager W, Jensen JB. Human malaria parasites in continuous culture. Science. 1976;193(4254):673-5.
79. Lambros C, Vanderberg JP. Synchronization of Plasmodium falciparum erythrocytic stages in culture. J Parasitol. 1979;65(3):418-20.
80. Wu Y, Sifri CD, Lei HH, Su XZ, Wellems TE. Transfection of Plasmodium falciparum within human red blood cells. Proc Natl Acad Sci U S A. 1995;92(4):973-7.
81. Crabb BS, Cowman AF. Characterization of promoters and stable transfection by homologous and nonhomologous recombination in Plasmodium falciparum. Proc Natl Acad Sci U S A. 1996;93(14):7289-94.
82. Graumans W, van der Starre A, Stoter R, van Gemert GJ, Andolina C, Ramjith J, et al. AlbuMAX supplemented media induces the formation of transmission-competent P. falciparum gametocytes. Mol Biochem Parasitol. 2024;259:111634.
83. van de Vegte-Bolmer M, Graumans W, Stoter R, van Gemert GJ, Sauerwein R, Collins KA, Bousema T. A portfolio of geographically distinct laboratory-adapted Plasmodium falciparum clones with consistent infection rates in Anopheles mosquitoes. Malar J. 2021;20(1):381.
84. Schindelin J, Arganda-Carreras I, Frise E, Kaynig V, Longair M, Pietzsch T, et al. Fiji: an open-source platform for biological-image analysis. Nat Methods. 2012;9(7):676-82.
85. Stone WJ, Eldering M, van Gemert GJ, Lanke KH, Grignard L, van de Vegte-Bolmer MG, et al. The relevance and applicability of oocyst prevalence as a read-out for mosquito feeding assays. Sci Rep. 2013;3:3418.
86. Ramjith J, Alkema M, Bradley J, Dicko A, Drakeley C, Stone W, Bousema T. Quantifying Reductions in Plasmodium falciparum Infectivity to Mosquitos: A Sample Size Calculator to Inform Clinical Trials on Transmission-Reducing Interventions. Front Immunol. 2022;13:899615.
87. Meyer L, López T, Espinosa R, Arias CF, Vollmers C, DuBois RM. A simplified workflow for monoclonal antibody sequencing. PLoS One. 2019;14(6):e0218717.
88. Rappsilber J, Ishihama Y, Mann M. Stop and go extraction tips for matrix-assisted laser desorption/ionization, nanoelectrospray, and LC/MS sample pretreatment in proteomics. Anal Chem. 2003;75(3):663-70.
89. Marr CR, Benlekbir S, Rubinstein JL. Fabrication of carbon films with ∼ 500nm holes for cryo-EM with a direct detector device. J Struct Biol. 2014;185(1):42-7.
90. Guo H, Franken E, Deng Y, Benlekbir S, Singla Lezcano G, Janssen B, et al. Electron-event representation data enable efficient cryoEM file storage with full preservation of spatial and temporal resolution. IUCrJ. 2020;7(Pt 5):860-9.
91. Punjani A, Rubinstein JL, Fleet DJ, Brubaker MA. cryoSPARC: algorithms for rapid unsupervised cryo-EM structure determination. Nat Methods. 2017;14(3):290-6.
92. Bepler T, Morin A, Rapp M, Brasch J, Shapiro L, Noble AJ, Berger B. Positive-unlabeled convolutional neural networks for particle picking in cryo-electron micrographs. Nat Methods. 2019;16(11):1153-60.

93. Punjani A, Zhang H, Fleet DJ. Non-uniform refinement: adaptive regularization improves single-particle cryo-EM reconstruction. Nat Methods. 2020;17(12):1214-21.
94. Sanchez-Garcia R, Gomez-Blanco J, Cuervo A, Carazo JM, Sorzano COS, Vargas J. DeepEMhancer: a deep learning solution for cryo-EM volume post-processing. Commun Biol. 2021;4(1):874.
95. Vonrhein C, Flensburg C, Keller P, Sharff A, Smart O, Paciorek W, et al. Data processing and analysis with the autoPROC toolbox. Acta Crystallogr D Biol Crystallogr. 2011;67(Pt 4):293-302.
96. Kabsch W. XDS. Acta Crystallogr D Biol Crystallogr. 2010;66(Pt 2):125-32.
97. McCoy AJ, Grosse-Kunstleve RW, Adams PD, Winn MD, Storoni LC, Read RJ. Phaser crystallographic software. J Appl Crystallogr. 2007;40(Pt 4):658-74.
98. Emsley P, Lohkamp B, Scott WG, Cowtan K. Features and development of Coot. Acta Crystallogr D Biol Crystallogr. 2010;66(Pt 4):486-501.
99. Liebschner D, Afonine PV, Baker ML, Bunkóczi G, Chen VB, Croll TI, et al. Macromolecular structure determination using X-rays, neutrons and electrons: recent developments in Phenix. Acta Crystallogr D Struct Biol. 2019;75(Pt 10):861-77.
100. Krissinel E, Henrick K. Inference of macromolecular assemblies from crystalline state. J Mol Biol. 2007;372(3):774-97.
101. Pettersen EF, Goddard TD, Huang CC, Meng EC, Couch GS, Croll TI, et al. UCSF ChimeraX: Structure visualization for researchers, educators, and developers. Protein Sci. 2021;30(1):70-82.
102. Jumper J, Evans R, Pritzel A, Green T, Figurnov M, Ronneberger O, et al. Highly accurate protein structure prediction with AlphaFold. Nature. 2021;596(7873):583-9.
103. Croll TI. ISOLDE: a physically realistic environment for model building into low-resolution electron-density maps. Acta Crystallogr D Struct Biol. 2018;74(Pt 6):519-30.
104. Chaudhury S, Lyskov S, Gray JJ. PyRosetta: a script-based interface for implementing molecular modeling algorithms using Rosetta. Bioinformatics. 2010;26(5):689-91.
105. Adams PD, Afonine PV, Bunkóczi G, Chen VB, Davis IW, Echols N, et al. PHENIX: a comprehensive Python-based system for macromolecular structure solution. Acta Crystallogr D Biol Crystallogr. 2010;66(Pt 2):213-21.
106. Morin A, Eisenbraun B, Key J, Sanschagrin PC, Timony MA, Ottaviano M, Sliz P. Collaboration gets the most out of software. Elife. 2013;2:e01456.
107. Li H. A statistical framework for SNP calling, mutation discovery, association mapping and population genetical parameter estimation from sequencing data. Bioinformatics. 2011;27(21):2987-93.
108. Ranford-Cartwright LC, Balfe P, Carter R, Walliker D. Genetic hybrids of Plasmodium falciparum identified by amplification of genomic DNA from single oocysts. Mol Biochem Parasitol. 1991;49(2):239-43.

1139 # METHODS
1140
1141 *Plasmodium falciparum* genome modification plasmids
1142
1143 To create the Cas9 guide plasmids, a pair of complementary guide-encoding oligonucleotides 5'-
1144 TTAATGATGGCTCTTGATTG-3' (targeting Pfs230 C-terminus to create iGP2$^{230\text{-tag}}$ / 230$^{\Delta D13/D14}$ / 230$^{\Delta Cterm}$)
1145 and 5'-ATTCTATTACATTATCAAGA-3' (targeting Pfs230D13 to create 230$^{\Delta D13/14}$) were treated with T4
1146 polynucleotide kinase, annealed, and ligated into BbsI-digested pMLB626 (a kind gift from Marcus Lee)
1147 (76).
1148
1149 To generate the iGP2$^{230\text{-tag}}$ homology-directed repair (HDR) template, partial 5' and full 3' homology
1150 regions (HR) were PCR amplified from NF54 genomic DNA (**Table S5**). Synonymous mutations to shield
1151 the Cas9 guide region in the full 5'HR were inserted by overlap PCR using the partial 5'HR and two
1152 annealed custom-made oligonucleotides (Sigma-Aldrich, **Table S5**). A selection cassette containing the i)
1153 PfH2B promoter, ii) the *mScarlet* gene, and iii) a bidirectional 3'UTR (PBANKA_142660) was PCR amplified
1154 from an in-house plasmid (77) as two separate amplicons to remove internal restriction sites. These two
1155 amplicons were cloned into pGGASelect using a BsaI-HFv2 Golden Gate reaction, and further sub-cloned
1156 using AatII and BamHI-HF into a pUC19-based plasmid that had all internal type IIS restriction enzymes
1157 removed via site-directed mutagenesis, yielding pRF0508. The final HDR template was created using the
1158 NEBridge Golden Gate Assembly Kit (BsmBI-v2), combining i) pGGAselect, ii) the 5' HR amplicon, iii) two
1159 annealed oligonucleotides coding for a tandem affinity purification tag (GTSG-(3xFLAG)-GSG-EPEA-stop)
1160 (**Table S5**), iv) pRF0508, and v) the 3' HR amplicon.
1161
1162 To generate HDR templates to make Pfs230$^{\Delta D13/14}$ and Pfs230$^{\Delta Cterm}$, the respective 5'HRs (Pfs230$^{\Delta D13/D14}$
1163 spanning Pfs230D11-12, Pfs230$^{\Delta Cterm}$ spanning Pfs230D13-14) and 3'HR were PCR amplified from NF54
1164 genomic DNA (**Table S5**). The selection cassette was modified by swapping the PfH2B promoter in
1165 pRF0508 for the PfGAPDH promoter (Pf3D7_1462800). The HDR templates were created in a golden gate
1166 reaction combining i) pGGAselect, ii) respective 5'HR amplicon, iii) PCR amplicon coding for (GGSG-
1167 3xFLAG-stop), iv) GAPDH selection marker, and v) the 3' HR amplicon.
1168
1169 All PCR reactions were performed using Primestar® GXL DNA polymerase (Takara Bio), all other cloning
1170 enzymes were obtained via New England Biolabs. Sequences were confirmed by Sanger Sequencing
1171 (Baseclear).
1172
1173 *Plasmodium falciparum* culturing, transfections, and gametocyte production
1174
1175 *P. falciparum* cultures were maintained at 37 °C with 3% O_2 and 4% CO_2, in complete medium (RPMI1640
1176 medium with 25 mM HEPES, 25 mM $NaHCO_3$, 10% human type A serum) with 5% O^+ human red blood
1177 cells (Sanquin, The Netherlands) (78). Asexual NF54/iGP2 and NF54/iGP2$^{230\text{-tag}}$ parasites were cultured in
1178 the presence of 2.5 mM D-(+)-glucosamine hydrochloride (Sigma #1514). Parasites were synchronized
1179 using sorbitol treatment before transfection or gametocyte induction (79).
1180
1181 For transfection, 80 µg of HDR plasmid was linearized overnight, ethanol precipitated and co-transfected
1182 with 80 µg of Cas9 guide plasmid by ring-stage transfection as described previously (80, 81). Briefly,
1183 plasmids were resuspended in cytomix (10 mM K_2HPO_4/KH_2PO_4 pH 7.6, 120 mM KCl, 0.15 mM $CaCl_2$, 5 mM
1184 $MgCl_2$, 25 mM HEPES, 2 mM EDTA) and added to a 3% ring-stage NF54/iGP2 (to generate iGP2$^{230\text{-tag}}$) or
1185 NF54 (to generate 230$^{\Delta D13/D14}$ / 230$^{\Delta Cterm}$) culture. Parasites were electroporated (310 V, 950 µF), allowed

1186 to recover for 4 h, after which transfected parasites were selected using 2.5 nM WR99210 (Jacobus
1187 Pharmaceuticals) for five days. To obtain single-cell clones for iGP2$^{230\text{-tag}}$, late-stage parasites were stained
1188 using 1 µg/ml Rhodamine123 solution, and single-cell sorted using a FACSAria III Cell Sorter (BD
1189 Biosciences) in a round-bottom 96 well plate containing 100 µl complete medium with 3% haematocrit.
1190 To obtain an isogenic population for 230$^{\Delta D13/D14}$ and 230$^{\Delta Cterm}$, parasites were sorted based on mScarlet
1191 expression using a Cytoflex SRT Benctop Cell Sorter (Beckman Coulter). Successful integration was
1192 confirmed by diagnostic PCR (**Table S5**).
1193
1194 To induce gametocytogenesis, a 1% early trophozoite culture (±24 hours post invasion) was induced with
1195 AlbuMAX medium (RPMI1640 supplemented with 25 mM HEPES, 25 mM $NaHCO_3$, and 0.5% AlbuMAX-II
1196 (Gibco, #11021-045)), in a previously described automatic shaker setup with media changes every 12 h
1197 (82, 83). Additionally, glucosamine was removed from iGP2-based cultures to further increase gametocyte
1198 induction. 36 h post induction until completion, cultures were maintained in complete medium. From day
1199 4 – 8 post induction, gametocytes were cultured in the presence of 20 units/ml heparin (Sigma, #H3393)
1200 to eliminate asexual parasite growth. To obtain late-stage gametocyte saponin pellets, gametocytes were
1201 harvested on day 13 post induction by incubating the cells for 10 min in a 10x pellet volume ice-cold 0.06%
1202 (w/v) saponin in PBS supplemented with 1x Complete™ Protease Inhibitor (PI) Cocktail (Roche), and
1203 subsequent centrifugation at 3,000xg for 5 min at 4 °C. Pellets were washed three times in ice-cold PBS
1204 with 1x PI, flash frozen and stored at -70 °C.
1205
1206 Western blot
1207
1208 Saponin pellets from late-stage gametocyte cultures were resuspended in lysis buffer (10 mM Tris-HCl (pH
1209 8.0), 150 mM NaCl, 1% (w/v) sodium deoxycholate, and 1x PI) for 15 min at RT. Lysate was cleared by
1210 centrifugation, and supernatant was supplemented with 1x NuPAGE LDS buffer, and heated to 56 °C for
1211 15 min. Samples were loaded on 4-12% Bis-Tris SDS-PAGE gels (SurePAGE), using Precision Plus Dual Color
1212 (BioRad) as a reference. After electrophoresis, proteins were transferred to 0.45 µm Immun-Blot PVDF
1213 membrane (Bio-Rad) using the Trans-Blot Turbo transfer system (Bio-Rad). Membranes were blocked in
1214 PBS with 3% BSA, before incubation with primary antibody diluted in PBS-T with 1% BSA. The following
1215 primary antibodies were used: 18F25 (mouse anti-Pfs230 (*36*), 5 µg/ml), 32F3 (mouse anti-Pfs48/45 (*25*),
1216 5 µg/ml), M2 (mouse anti-FLAG, F1804 Sigma, 1:2000), CaptureSelect™ (biotinylated single domain
1217 antibody fragment anti-C-tag, Thermofisher, 1:1000). After washing, blots were incubated with one of the
1218 following secondary antibodies: HRP-conjugated rabbit anti-mouse (P0260, Dako, 1:2000), HRP-
1219 conjugated streptavidin (890803, R&D Systems, 1:500). Blots were developed with Clarity Western ECL
1220 substrate (BioRad) and imaged on an ImageQuant™ LAS 4000 (GE Healthcare).
1221
1222 Immuno-fluorescence microscopy
1223
1224 Heparin-treated stage V gametocytes (day 13) were fixed (4% EM-grade paraformaldehyde, 0.0075%
1225 glutaraldehyde in PBS) for 20 min on pre-warmed poly-L-lysine coated coverslips at 37 °C. Cells were
1226 permeabilized with 0.1% Triton X-100, washed in PBS and blocked using 3% BSA in PBS for 1 h. Primary
1227 and secondary antibodies were incubated for 1 h at RT, with PBS washes in between. Primary antibodies
1228 were diluted in 1% BSA in PBS, and included M2 (mouse anti-FLAG, F1804 (Sigma), 1:500), RUPA-55 mAb
1229 (human anti-Pfs230 (*20*), 5 µg/ml), and 45.1 mAb (rat anti-Pfs48/45 (*25*), 5 µg/ml). Secondary antibodies
1230 (goat anti-mouse 594 (A11031), goat anti-human 488 (A11013), and chicken anti-rat 674 (A21472)
1231 (ThermoFisher)) were all diluted 1:500 in PBS with 1 µM DAPI. Coverslips were mounted using
1232 Vectashield® Antifade Mounting Medium (Vector Laboratories). Images were taken on a Zeiss LSM900
1233 Airyscan confocal microscope using a 63x oil objective with 405, 488, 561, and 633 nm laser excitation

1234 and an Electronically Switchable Illumination and Detection Model (ESID) for transmitted light. Images
1235 were processed for airyscan, using the Zeiss Zen Blue software and analysed using FIJI software (84).
1236
1237 Suspension Immunofluorescence Microscopy (SIFA)
1238
1239 For gamete SIFAs, heparin-treated stage V gametocytes (day 13 post-induction) were collected, spun
1240 down to remove the culture medium, and resuspended in half the culture volume of FCS. After incubation
1241 with gentle agitation at RT for 1 h, parasites were spun down and washed in ice-cold PBS. For saponin-
1242 treated gametocytes, heparin-treated stage V gametocytes (day 13 post-induction) were collected, spun
1243 down, and resuspended in half the volume of ice-cold PBS supplemented with 0.06% Saponin and 1x
1244 protease inhibitor. After 10 min incubation on ice, saponin-treated gametocytes were harvested by
1245 centrifugation and washed three times in ice-cold SIFA buffer (PBS supplemented with 0.5% FCS). All
1246 subsequent steps were performed at 4 °C.
1247
1248 Both gametes and gametocytes were incubated for 1 h in SIFA buffer with 15 µg/ml mAb 18F25 or 45.1,
1249 labeled with LYNX Rapid Plus DyLight488 Antibody Conjugation Kit (Bio-Rad). After washing in ice-cold
1250 SIFA buffer, parasites were resuspended in ice-cold PBS and deposited in pre-cooled poly-L-lysin-coated
1251 µ-slide 8 well Ibidi chambers. Parasites were allowed to settle at 4 °C, after which the Ibidi chamber was
1252 transferred to a room-temperature Axio Observer 7 Inverted LED microscope equipped with a Colibri 7
1253 LED source and Axiocam 705 mono (Zeiss). Images were taken with a 63x oil objective using the 475 nm
1254 LED module and a Differential Interference Contrast enhanced brightfield channel. Images for different
1255 parasite lines were taken on the same day with the same microscope settings, and were analyzed with
1256 the same settings in FIJI software (84).
1257
1258 Exflagellation assay and standard membrane feeding assay
1259
1260 Day 15 cultures of non-heparin treated gametocytes were used to test exflagellation. Cultures were mixed
1261 1:1 with 50 µM xanthurenic acid in complete media, and incubated at room temperature in a dark, humid
1262 chamber for 15 min. The number of exflagellation centres per ml was determined by bright-field
1263 microscopy using a Neubauer chamber. To assess mosquito infectivity, day 15 non-heparin treated
1264 gametocytes were added to the bloodmeal of *Anopheles stephensi* mosquitoes (colony maintained at
1265 Radboudumc (Nijmegen, The Netherlands)), as described previously (85). In the SMFA experiments with
1266 2A2, purified 2A2.2a IgG was diluted in FBS to a final concentration within the total bloodmeal of 10 µg/ml,
1267 and mixed with mature *P. falciparum* gametocytes and human serum that contains active complement.
1268 Mosquito midguts from 20 mosquitoes were dissected 6-8 days after the blood meal, stained with
1269 mercurochrome, and oocysts were counted by microscopy. Transmission reducing activity was calculated
1270 as described previously (86).
1271
1272 Affinity purification of Pfs230:Pfs48/45 complex from stage V gametocytes
1273
1274 Frozen stage V gametocyte pellets were resuspended in solubilization buffer (25 mM HEPES pH 7.4, 150
1275 mM KCl, 10% glycerol, 1x PI, and 0.25% (v/v) DDM), and rotated at 4 °C for 1 h. The cell suspension was
1276 centrifuged at 18,000xg at 4 °C for 30 min, after which the pellet was solubilized a second time following
1277 the previous steps. The combined supernatants were applied to anti-FLAG® M2 affinity resin (Merck), and
1278 incubated overnight at 4 °C. The resin was extensively washed in Wash buffer (25 mM HEPES pH 7.4, 150
1279 mM KCl, 10% glycerol, 1x PI, and 0.02% DDM), after which proteins were eluted using 5x resin volume of
1280 elution buffer (25 mM HEPES pH 7.4, 150 mM KCl) supplemented with 0.02% DDM, and 150 µg/ml 3xFLAG
1281 peptide (Merck)). For cryo-EM studies, the eluted proteins were mixed with a fivefold molar excess of

1282 RUPA-97, LMIV230-01, 2A2, 18F25, RUPA-71, and RUPA-44 Fabs and incubated on ice for 30 min. After
1283 concentrating the protein fraction, the Fab-bound complex was separated from unbound Fabs by high-
1284 pressure size exclusion chromatography using a Bio SEC-3 300 Å column (Agilent, 5190-5213), pre-
1285 equilibrated with elution buffer.
1286
1287 Expression and purification of Fabs, mAbs, and recombinant proteins
1288
1289 Expression and purification of individual Fabs was performed as described previously (20, 32). Variable
1290 light and heavy chains were gene synthesized (GeneArt), and cloned into a custom pcDNA3.4 expression
1291 vector directly upstream of the constant chains. The variable chain sequences for 32F3, TB31F, LMIV-230s,
1292 and all RUPA mAbs were described previously (20, 32, 41). Variable sequences for 18F25 (**Table S6**) were
1293 determined by a previously published workflow for hybridoma sequencing (87). In short, RNA was
1294 obtained from 18F25.1 hybridoma cells by Trizol purification, which was used as template for RT-PCR with
1295 heavy/kappa constant chain specific reverse primer and a universal template-switching oligonucleotide
1296 (**Table S5**). The obtained cDNA was used for a PCR, and obtained PCR products were inserted into a TOPO
1297 vector, and sequenced by Sanger Sequencing (Baseclear, The Netherlands). Variable sequences for 2A2
1298 were sequenced by Genmab (**Table S6**). For the IgGs produced for complement-fixation assays, sequences
1299 of the variable chain of α-Pfs230D1 IgGs were described previously (20), and ordered as synthetic products
1300 subcloned into custom-made pcDNA3.4 vectors directly upstream of Igγ1-CH1-CH3 or Igκ-CL1.
1301
1302 Fab and IgG purification were done in a similar manner. Plasmids coding for Fab/IgG heavy chain and light
1303 chain were co-transfected at a 1:1 molar ratio using PEI MAX® transfection reagent (PolySciences) into
1304 Freestyle 293-F or 293-S cells (ThermoFisher). Cells were cultured in FreeStyle 293 Expression medium
1305 (Gibco) at 37 °C and 8% CO_2 while shaking for seven days, after which the supernatant containing secreted
1306 recombinant protein was collected. After filtering, the supernatant was used for affinity purification using
1307 a HiTrap Kappaselect column (Cytiva) for recombinant Fab, or the HiTrap Protein G HP column (Cytiva) for
1308 recombinant IgG, pre-equilibrated in 1x PBS. In both cases, recombinant protein was eluted in 100 mM
1309 glycine (pH 2.2). Fabs were further purified by cation-exchange chromatography using a MonoS column
1310 (Cytiva) with a buffer of 20 mM sodium acetate (pH 5.6) across a 0-1.0 M potassium chloride gradient.
1311
1312 Single Pfs230 domains Pfs230D1 and Pfs230D10 were expressed and purified as described previously (36).
1313 Coding sequences for the double Pfs230 domain D13-14-Cterm (residue 2831-3105) were ordered and
1314 synthesized as *Drosophila melanogaster* codon-optimized sequences (Baseclear). The synthetic gene was
1315 subcloned into pExpreS2.2 plasmid (ExpreS2ion Biotechnologies), in frame with an N-terminal BiP signal
1316 peptide – His_6 tag. The expression plasmid was used to transfect *D. melanogaster* S2 cells (ExpreS2ion
1317 Biotechnologies) to generate stable cell lines as described previously (36). Pfs230D13-14-Cterm-
1318 containing supernatant was loaded directly on a 1 ml cOmplete™ His-Tag Purification Column (Roche).
1319 The column was washed with PBS, and Pfs230D13-14-Cterm was eluted using PBS with 250 mM imidazole.
1320 After overnight dialysis against PBS, the sample was concentrated and further purified by size-exclusion
1321 chromatography using a Superdex200 Increase column (Cytiva), using PBS as running buffer.
1322
1323 Blue Native Polyacrylamide Gel Electrophoresis
1324
1325 For BN-PAGE, the elution fraction from FLAG-based affinity purification, containing purified
1326 Pfs230:Pfs48/45 protein complex, was used. To test Fab binding to the complex, a tenfold molar excess
1327 of Fab fragment was added to the purified Pfs230:Pfs48/45 complex, and incubated on ice for 30 min.
1328 Protein samples were supplemented with a home-made 1x loading solution (final concentration 10%
1329 glycerol, 0.025% Coomassie Blue G-250), and loaded on a NativePAGE™ 3-12% Bis-Tris protein gels

1330 (ThermoFisher) following manufacturer's protocols. NativeMark™ Unstained Protein Standard was used
1331 as marker. After electrophoresis, gels were either stained with Coomassie InstantBlue® protein stain
1332 (Abcam) or incubated in 0.1% SDS for western blotting. For western blotting, proteins were transferred to
1333 0.45 µm Immun-Blot PVDF membrane (BioRad) using the Trans-Blot Turbo Transfer system (BioRad). After
1334 transfer, proteins were fixed to the membrane using 8% acetic acid. Membranes were air-dried, washed
1335 in pure methanol and re-hydrated using MQ. Blocking, antibody incubation and detection were performed
1336 as described above.
1337
1338 Mass spectrometry
1339
1340 Three batches of 40 ml heparin-treated, late-stage gametocyte cultures (iGP2$^{230\text{-tag}}$ and iGP2 WT) of
1341 comparable gametocytaemia were harvested and lysed in parallel, as described as above for purification
1342 of the endogenous Pfs230:Pfs48/45 complex. Protein concentration in parasite lysate was determined
1343 using the PierceTM BCA Protein Assay kit. 120 µg of protein extract in 300 µl solubilization buffer (25 mM
1344 HEPES pH 7.4, 150 mM KCl, 10% glycerol, 1x PI, and 0.25% (v/v) DDM) was applied on 10 µl anti-FLAG®
1345 M2 affinity resin, and incubated overnight. The resin was washed in ice-cold wash buffer (25 mM HEPES
1346 pH 7.4, 150 mM KCl, 10% glycerol, 1x PI, and 0.02% DDM) three times, and consequently washed three
1347 times in ice-cold PBS (Gibco). After harvesting, beads were resuspended in 50 µl elution buffer (100 mM
1348 Tris-HCl pH 8.0, 2 M Urea, 10 mM DTT), and incubated for 20 min at 25 °C with shaking. 50 mM
1349 iodoacetamide was added to alkylate cysteines, after which samples were kept in the dark for 10 min at
1350 25 °C. After adding 0.25 µg sequencing grade trypsin (Promega), samples were incubated at 25 °C for 2 h
1351 with gentle shaking. Samples were spun down, supernatants were collected, and the beads were
1352 resuspended in 50 µl fresh elution buffer. After 5 min incubation on a shaker, the samples were spun
1353 down again and the supernatant combined with the previous elution fraction. Another 0.1 µg of fresh
1354 trypsin was added to the combined supernatants, which was left to digest overnight at 25 °C. The following
1355 day, samples were concentrated and purified on C18 StageTips (88). Samples were analyzed on a Obitrap
1356 Exploris 480 mass spectrometer (ThermoScientific) ran in Top20 mode (with dynamic exclusion enabled
1357 for 45 s), operated with an online Easy-nLC 1000. A gradient of buffer B (80% acetonitrile, 0.1% formic
1358 acid) was applied for 60 min. Raw data was analyzed using Maxquant software (version 2.1.4.0), and
1359 analyzed against a *Plasmodium* database (PlasmoDB, downloaded 21-10-2022). LFQ, iBAQ and match
1360 between runs were enabled, and deamidation (NQ) was added as additional variable modification. The
1361 resulting output was filtered using Perseus (version 1.0.15), removing potential contaminants, reverse
1362 hits, and proteins with less than two unique peptides or with less than three valid values in at least one
1363 group. Missing values were imputed using default settings, and a t-test was performed to identify outliers.
1364 Data was visualized using GraphPad Prism.
1365
1366 Cryo-EM data collection and image processing
1367 The Pfs230:Pfs48/45:RUPA-97:LMIV230-01:2A2:18F25:RUPA-71:RUPA-44 Fab complex was concentrated
1368 to 0.8 mg/ml, and 1.8 µl sample was deposited on homemade holey gold grids (89) that were glow-
1369 discharged in air for 15 s. Excess sample was blotted away for 1.7 s using a Leica EM GP2 Automatic Plunge
1370 freezer at 4 °C and 90% humidity, and plunge-frozen in liquid ethane. Data was collected on a Thermo
1371 Fisher Scientific Titan Krios G3 equipped with a Selectris X energy filter (slit width: 10 eV) and Falcon 4i
1372 camera, operated at 300 kV and automated with the EPU software. Data was collected at a magnification
1373 of 130,000× with a calibrated pixel size of 0.93 Å. Exposures were collected for 6.5 s as movies with a
1374 camera exposure rate of ~7.11 or ~7.15 e^- per pixel per s, and total exposure of ~50 or ~53.7 electrons/Å^2
1375 and recorded in Electron Event Representation mode (90). Before processing, movies were fractionated
1376 into 30 frames. A total of 8,545, 1,572, and 6,533 raw movies were obtained at 0°, 35°, and 40° tilt,
1377 respectively.

The collected cryo-EM data was processed using CryoSPARC v4.6.0 (91). The movies from the 35° tilted, 40° tilted, and untilted data collections were corrected for motion in patches, and contrast transfer function (CTF) parameters were estimated in patches. Resulting micrographs were curated using thresholds for average defocus values (4,000-35,000 Å), CTF fit resolution (2.0-5.0 Å), and relative ice thickness (0.95-1.10). An *in silico* model of the Pfs230:Pfs48/45:RUPA-97:LMIV230-01:2A2:18F25:RUPA-71:RUPA-44 complex was built from AF models and arranged based on views seen from 2D classes. The resulting model was used to generate particle templates corresponding to 40 evenly distributed projections which were low-pass filtered to 20 Å to avoid model bias. Initially, particle images were selected from a subset of 2,000 curated micrographs, which were then extracted in 450x450 pixel boxes and subjected to 2D classification. Classes where the average showed clear views of the complex were used to train a Topaz particle selection model (92), with subsequent 2D classification steps used to clean the dataset of selected particle images. To focus on the various subsections of the full complex, 2D class average images showing the appropriate domains were used as templates to select more particles from the full dataset of 12,192 curated micrographs. Further Topaz models were trained on specific regions (Pfs230D1-6:RUPA-97:LMIV230-01:2A2, Pfs230D9-14:Pfs48/45:RUPA-71:RUPA-44) of the full complex, after which particles images were selected and extracted with the trained models. Initial junk particle image removal was performed with multiple rounds of 2D classification, followed by *ab initio* 3D reconstruction. Non-particle images and poorly behaved particle images were removed with a combination of heterogeneous refinement, 3D classification, and 2D classification. Selected particle images were used to generate 3D maps with reconstructions in non-uniform refinement (93) jobs without enforced symmetry (C1). The resulting maps were further improved by local refinement and post-processing with DeepEMhancer (94). Heterogeneity for 2A2 Fab binding could be distinctly observed, such that two maps of Pfs230D1-6:LMIV230-01:RUPA-97 were obtained: with and without 2A2 Fab. A detailed processing flow path and experimental map details are available in the supplementary document (**Figure S2, 3A-3D**).

For the Pfs230D7-8:18F25 map, particle images from a subset of 500 micrographs were used from one set of collections of the untilted (2,003), 35° tilted (337), and 40° tilted (2,866) micrographs for blob picking after motion correction, CTF estimation, and curation of the micrographs (average defocus = 1000-30,000 Å; CTF fit resolution < 5 Å; relative ice thickness = 0.954-1.1; astigmatism < 4000 Å). The 101,225 particle stack was cleaned using multiple rounds of 2D classification, ab initio reconstruction, and homogeneous refinement (4.89 Å). The rebalance orientations job was used, followed by ab initio reconstruction and non-uniform refinement (4.19 Å). A map containing the interface between Pfs230 and 18F25 Fab was determined by cleaning the particle stack with 2D classification, followed by ab initio reconstruction and homogeneous refinement (10.03 Å). This map, along with the 4.19 Å map and a junk class generated with ab initio reconstruction were used as input for heterogeneous refinement, resulting in a class containing 18F25 with 35,162 particles. The resulting particle stack was cleaned with multiple rounds of 2D classification, with the final particle stack used for Topaz training on denoised micrographs. Ab initio reconstruction with five classes was run using the resulting 100,481 particle stack, followed by heterogeneous refinement. The particle stack from the class containing 18F25 was cleaned using 2D classification, then used again for Topaz training on all micrographs (6,372 untilted, 1,125 35° tilted, 2,866 40° tilted). To ensure the particles were centered on 18F25, ab initio reconstruction, followed by non-uniform refinement was run with the resulting 366,876 particle stack at a box size of 600 pix and Fourier crop of 300 pix (5.79 Å), followed by centering of the particles using volume alignment tools and re-extraction of the particles to 300 pix boxes. 2D classification without re-centering, 2 class ab initio reconstruction, and heterogeneous refinement were used to obtain a clean 216,684 particle stack. A further three rounds of 2D classification and two rounds of non-uniform refinement and local refinement

resulted in a 3.88 Å map using 106,349 particles. Post-processing was performed in EMReady to prepare the map for model building. A detailed processing workflow and experimental map details are available in the supplementary document (**Figure S2, 3E**).

X-Ray Crystallography

Fractions containing purified 2A2, 18F25, and RUPA-71 Fab following cationic exchange chromatography were pooled and concentrated at 16.8 mg/mL, 27.3 mg/mL, and 10 mg/ml, respectively in preparation for crystallization trials. RUPA-71 Fab was mixed in a 1:1 ratio with reservoir conditions from a JCSG Top96 screen (0.2 µL + 0.2 µL) using the sitting drop vapor diffusion method. RUPA-71 crystals then formed in a drop containing 0.2 M $(NH4)_2SO_4$, 0.1 M MES 6.5 pH, and 30 %w/v PEG MME 5K. For the 2A2 and 18F25 Fab crystallization trials, reservoir conditions from a JCSG Top96 screen and Fab were mixed at a 1:1 volumetric ratio (0.3 µL + 0.3 µL) resulting in 0.6 µL drops. Approximately 48 h after setting drops at room temperature, 2A2 crystals were obtained from a drop containing reservoir solution: 30% (w/v) PEG 4K. 18F25 crystals were obtained from a drop containing reservoir solution: 0.2 M Na_2SO_4 and 20% (w/v) PEG 3350. The 2A2 and 18F25 crystals were cryo-protected with 25% glycerol (v/v) and 15% polyethylene glycol 200 (PEG200), respectively. Crystals of all three samples were flash-frozen in liquid nitrogen. Data collection on 2A2 and 18F25 was performed at the 17-ID-1 beamline at the Brookhaven National Laboratory Synchrotron Light Source (Beam wavelength = 0.920194 Å). RUPA-71 data collection occurred at the CMCF-ID beamline at the Canadian Light Source (Beam wavelength = 0.95357 Å).

X-Ray Crystallography model building and refinement

Datasets were processed using autoproc (95) and xds (96). A molecular replacement solution was obtained using PhaserMR (97) using an *in silico*-derived model of the Fab domains predicted via ABodyBuilder2. Model building and refinement was performed using Coot (98) and phenix.refine (99). For the RUPA-71 Fab crystal structure, 98.0% of the dihedral angles are in "favoured regions" of the Ramachandran plot; 2.0% are in the "allowed regions;" and 0% are "outliers." For the 2A2 Fab crystal structure, 98.3% of the dihedral angles are in "favoured regions" of the Ramachandran plot; 1.7% are in the "allowed regions;" and 0% are "outliers." For the 18F25 Fab crystal structure, 97.4% of the dihedral angles are in "favoured regions" of the Ramachandran plot; 2.6% are in the "allowed regions;" and 0% are "outliers." **(Table S3).** Inter- and intra-molecular contacts were determined using PISA (100) and manual inspection. Structural figures were generated using UCSF ChimeraX (101).

Cryo-EM model building

Starting structural models were obtained by manually fitting previously determined structural models (PDB: 8U1P, Pfs48/45-D1D2; 7UXL, Pfs48/45-D3:RUPA-44; 7UVQ, Pfs230-D1:RUPA-97; and 7UFW, Pfs230-D1D2:LMIV230-01), novel crystal structures (Fabs of 18F25, RUPA-71, and 2A2), and models generated by AlphaFold2 (102)and AlphaFold3 (64) into the experimentally determined maps. Structural refinements were performed using Isolde (103), PyRosetta (104), and PHENIX (105); models were manually checked and improved with Coot (98). Images were generated using ChimeraX (101). Access to all software was supported through SBGrid (106).

Single nucleotide polymorphism detection

Single nucleotide polymorphisms were obtained from the MalariaGEN Catalogue of Genetic Variation in Pf version 7 (53). Genotype calls for chromosomes 2 and 13 (Pf3D7_02_v3 and Pf3D7_13_v3, respectively)

1474 were downloaded (https://ngs.sanger.ac.uk/production/malaria/Resource/34/Pf7_vcf/). Bcftools
1475 (107)was used to subset calls and calculate the allele frequencies between nucleotide positions 369,351
1476 and 380,156(+) on chromosome 2 that coincide with Pfs230 and between nucleotide positions 1,875,452
1477 and 1,878,087(-) on chromosome 13 that coincide with Pfs48/45. SNPs calls below MalariaGEN's quality
1478 filter (Low_VQSLOD) were removed before identification of missense variants.
1479
1480 Gamete binding assay with flow cytometry
1481
1482 Heparin treated stage V gametocytes (day 13 – 16 post induction) were collected and resuspended in FCS
1483 with half the volume of the original culture volume. Gamete maturation was induced for 30 min at room
1484 temperature while shaking, after which samples were centrifuged at 2,000xg at 4 °C. The pellet was
1485 resuspended in PBS and placed on a layer of 12.4% Nycodenz (Serumwerk Bernburg) and centrifuged for
1486 30 min at 3,500xg without break at 4°C. The top layer containing female gametes was harvested and
1487 washed in PBS before continuing.
1488 50,000 female gametes per well were deposited in a V-bottom non-treated 96-well plate (Costar). All
1489 gamete incubations were carried out at RT in PBS supplemented with 2% Fetal Calf Serum (FCS, Gibco)
1490 and 0.02% sodium azide, and washed in ice-cold PBS. All secondary antibody incubations included
1491 eBioscience™ Fixable Viability Dye eFluor™ 780 (Invitrogen, 1:1000). For the Pfs230 domain binding
1492 experiment (**Figure S6A**), gametes were incubated for 1 h with recombinant proteins and washed in PBS.
1493 Afterwards, gametes were incubated with mouse anti-his tag antibody (Sigma-Aldrich, A7058, 1:200) for
1494 1 h, washed, and stained with chicken-anti-mouse 488 secondary antibodies (Invitrogen, A21200, 1:200)
1495 for 30 min. For the antibody gamete binding experiment (**Figure S6H, Figure 5G**), gametes were incubated
1496 with 1 µg/ml antibody for 1 h, washed, and stained with goat-anti-human 488 secondary antibody
1497 (Invitrogen, A11013, 1:200). For the Fab competition experiment (**Figure S7C**), gametes were incubated
1498 for 1 h with Fabs. After washing in PBS, gametes were stained with 18F25 antibody labeled with LYNX
1499 Rapid Plus DyLight488 Antibody Conjugation Kit (Bio-Rad, 5 µg/ml). Finally, for complement deposition
1500 assay, gametes were incubated with 1 µg/ml antibody for 1 h and washed. Gametes were then incubated
1501 with 10% Normal Human Serum (Sanquin, The Netherlands) and incubated for 45 min at RT. After
1502 washing, parasites were first stained with polyclonal goat anti-human C1q (CompTech, 1:5,000) or anti-
1503 human C3 (CompTech, 1:10,000), washed, and finally stained with donkey-anti-goat 488 secondary
1504 antibody (Invitrogen, A11055, 1:200). After staining, gametes were resuspended in PBS and fluorescence
1505 was measured for approximately 2,000 gametes with the Gallios™ 10-color system (Beckman Coulter),
1506 and analyzed with FlowJo (BD, version v10.10.0). For all gamete binding experiments only live gametes
1507 were analyzed, except for the complement deposition assays for which both live and dead gametes were
1508 included in the analysis (gating strategy in **Figure S7K**). Statistical analyses were performed using
1509 GraphPad Prism (version 10.4.1), and are described in the figure legends.
1510
1511 DNA extraction and PCR analysis of midgut oocysts
1512
1513 Mosquito midguts were dissected into individual tubes seven days after the infectious blood meal, and
1514 DNA was extracted using a protocol modified from Ranford-Cartwrigth *et al.* (108). In short, the midgut
1515 was incubated at 56 °C overnight in oocyst lysis buffer (10 mM Tris-HCl pH 8.8, 100 mM NaCl, 25 mM
1516 EDTA, 0.5% N-lauroyl sarcosine, 1 mg/ml Proteinase K). DNA was extracted from the lysate using
1517 phenol/chloroform/isoamyl alcohol (25:24:1), followed by isopropanol precipitation. The DNA pellet was
1518 washed with 70% EtOH, dried and redissolved in 20 µl ultra-pure water. The presence of wildtype or
1519 truncated *pfs230* gene was confirmed with a semi-nested PCR protocol (**Table S5**) as described previously
1520 (38).
1521

1522 Pfs230D7-18F25 SPR binding analysis
1523
1524 The gene sequences coding for Pfs230D7, including the SNP mutant sequences, were optimized for wheat
1525 codon usage, purchased from GenScript, and cloned into a pEU-E01 expression vector (CellFree Science,
1526 Matsuyama, Japan) (37). The recombinant Pfs230D7 proteins were expressed as C-terminally His-tagged
1527 proteins in wheat germ cell-free extract WEPRO7240H (CellFree Science), supplemented with Disulfide
1528 Bond Enhancer Enzyme Set (CellFree Science). Proteins were purified by single-step His-tag purification
1529 using a Ni Sepharose 6 Fast Flow column (Cytiva), following the manufacturer's instructions.
1530
1531 The binding kinetics between recombinant Pfs230D7 proteins and 18F25 were measured using a Biacore
1532 X100 instrument (Cytiva). The antibody 18F25 was immobilized on the sensor chip using
1533 the Mouse Antibody Capture Kit (Cytiva) according to the manufacturer's instructions. Recombinant
1534 Pfs230D7 proteins were injected in HBS-EP+ running buffer (Cytiva) using a single-cycle kinetic format.
1535 Data were analyzed with Biacore X100 Evaluation Software, and kinetic parameters were calculated using
1536 a 1:1 binding model.